博士論文

Pressurization process of shallow magma reservoir of Stromboli volcano (Italy) as inferred from analyses of ground deformation associated with different-type eruptions

（地盤変動解析により推定されるストロンボリ火山の異なる様式の噴火に伴う浅部マグマだまりの増圧過程）

石川　歩

令和４年

Doctoral Thesis

Pressurization process of shallow magma reservoir of Stromboli volcano (Italy) as inferred from analyses of ground deformation associated with different-type eruptions

[地盤変動解析により推定される
ストロンボリ火山の異なる様式の噴火に伴う
浅部マグマだまりの増圧過程]

Ayumu Ishikawa
（石川　歩）

Department of Geophysics
Graduate School of Science
Tohoku University

Thesis Committee Members

Professor Takeshi Nishimura (Chair, Supervisor)
Professor Maurizio Ripepe (University of Florence, Co-supervisor)
Professor Satoshi Miura
Associate Professor Tomofumi Kozono
(National Research Institute for Earth Science and Disaster Resilience)
Associate Professor Yo Fukushima
(International Research Institute of Disaster Science)
Assistant Professor Giorgio Lacanna (University of Florence)
Doctor Dario Delle Donne (National Institute of Geophysics and Volcanology)

2022

Acknowledgement

First and foremost, I am deeply grateful to my supervisours Prof. Takeshi Nishimura and Prof. Maurizio Ripepe for their continuous assistance and patience during my PhD thesis project. Their immense knowledge, plentiful experience and powerful motivation encouraged me in every stage of the academic research and my daily life.

I am very thankful to Prof. Satoshi Miura and Associate Prof. Yo Fukushima, for their invaluable comments on this study. I would like to express my sincere gratitude to my colleagues in the Solid Earth Physics Laboratory, Associate Prof. Hisashi Nakahara, Associate Prof. Tomofumi Kozono, Associate Prof. Sayaka Saito, Assistant Prof. Masayuki Kano, Assistant Prof. Kimiko Taguchi, former Assistant Prof. Kentaro Emoto, former Assistant Prof. Yasuhito Jibiki for their support for maintaining computational environment, solving technical problem and valuable advices on my research. I would like to express my sincere thanks to my colleagues in the Labortorio di Geofisica Sperimentale - Associate Prof. Emanuele Marchetti, Assistant Prof. Giorgio Lacanna, Dr. Dario Delle Donne, Dr. Giacomo Ulivieli, Dr. Massimo Della Schiacva, Dr. Lorenzo Innocenti, Dr. Maria Cristina Silengo, Dr. Gilda Risica, Dr. Letizia Orti and Dr. Riccardo Genco for their fruitful discussion on my work and and assistance for my daily life in Italy. I would like to extend my gratitude to my research collaboraters - Prof. Hiroshi Aoyama, Dr. Ryohei Kawaguchi, Dr. Eisuke Fujita, Assistant Prof. Taishi Yamada and Dr. Takairo Miwa for their cooperation and advices on my work. I sincerely thank students of my laboratories in Japan and Italy for active discussion on scientific topic and friendship.

I also express my gratitude to all the professors and students of Research Center for Prediction of Earthquakes and Volcanic Eruptions, the members of reseach collaborators in Italy - Universuty of Pisa, University of Palermo and University of Torino, and the academic board of the 35th cycle of the PhD course on Earth Sciences for their comments and discussions in seminars, congress presentations and field works. I would like to offer

my special thanks to Ms. Chika Kamada, Ms. Naoko Mizuta, Ms. Yumiko Takahashi, Ms. Shinobu Okuyama and Ms. Serena Cartei for all their administrative support.

This work was supported by the Bilateral Joint Research Projects/Seminars of Japan Society for the Promotion of Science, the Italian Civil Protection in the framework of the DEVNET project and the International Joint Graduate Program in Earth and Environmental Science (GP-EES) in Tohoku University. I am also grateful to the Integrated Program fro Next Generation Volcano Research and Human Resource Development.

Finally, I would like to express my deep and sincere gratitude to my family and friends for their continuous supports and encouragements.

Abstract

The mechanism of volcanic eruptions has been studied by multidisciplinary approaches to interpreting complex and various physical processes of volcanic phenomena such as effusive eruptions and explosive ones as well as small to large magnitude. However, the mechanisms of magma ascent before volcanic eruptions have not been well understood due to the occasionality of eruptions and the difficulty of near-vent observation. It is thus necessary to investigate volcanoes that show repetitive eruptive activity and have an ideal environment for field measurement. In this study, we focus on Stromboli volcano (Italy), whose eruptive activity is characterized by various-type eruptions with different explosivity and intensity, generally classified into three types: ordinary explosion, so-called Strombolian eruption, lava effusion and more violent explosion, so-called paroxysm. This study aims to clarify similarities and differences among the eruptions in the aspect of ground deformation. We systematically analyze ground tilt signals recorded by near-vent measurement network to capture tiny deformation associated with volcanic eruptions and to estimate parameters of underground pressure sources in order to understand the dynamics of magma ascent.

In Chapter 1, we first review the ground deformation studies of volcanoes, from the basic framework to the recent development of field measurement techniques and theoretical models. We further present the eruptive activity and volcanological framework of Stromboli volcano (Italy), summarizing previous studies mainly on the geophysical approaches. We present the motivation and objectives of the thesis at the end.

In Chapter 2, we show the observation network and data on tilt measurement at Stromboli volcano used for the analyses. Borehole tiltmeters of the permanent multiparametric network operated by the University of Florence are used for all eruption types. For the analysis of ordinary explosions and the 7 August 2014 lava effusion, we further use three temporary platform tiltmeters installed by Japan-Italy collaboration research

conducted in 2014–2015. For the analysis of the 3 July 2019 paroxysm, we use tilt signals retrieved from five broadband seismometers of the permanent network. These tilt and seismic stations are deployed at close distances (<1.2 km from the eruptive craters) and thus record high-quality ground deformation signals.

In Chapter 3, we analyze tilt signals associated with three different types of eruptions (ordinary explosion, lava effusion and paroxysm) at Stromboli volcano to examine their characteristics of the observed tilt vectors that are used for the pressure source estimation in Chapter 4. We classify the ground tilt associated with ordinary explosion into four stages: (A) gradual inflation starting ∼200 s before each explosion, (B) rapid inflation ∼15 s before, (C) rapid deflation after the onset of explosion and (D) recovery process. We focus on (A) gradual inflation that is not contaminated with the Very-Long-Period (VLP) seismic signal to infer a volcanic pressure source which reflects magma dynamics before the ordinary explosion. The observed tilt vector is calculated by stacking 868 events that occurred from 1 to 14 July 2014. Our tilt network in 2014 also recorded local ground inflation caused by dyke intrusion ∼15 h before the 7 August 2014 lava effusion and ground deflation with >2 days at all the stations. Amplitude of tilt signal between -15 h and +48 h is used as representative tilt vector for pressure source estimation. Data analysis using tilt signal retrieved from seismogram identifies unique and robust ground deformation starting ∼3.5 hours before a paroxysm occurring on 3 July 2019. The initial part (-600 s to -200 s) of the final inflation is used for pressure source estimation. Tilt vectors derived from the analyses of the three types of eruptions generally direct to the summit crater area and share a similar deformation field.

In Chapter 4, we invert the observed tilt vectors to determine the location and the shape of the pressure source. We calculate the ground deformation caused by an ellipsoidal pressure source using a finite element method (FEM) to include the effect of the volcano topography. The pressure source is modelled as an ellipsoidal cavity whose X-axis is aligned to E50°N. Firstly, we estimated the best-fit location of a spherical source and its pressure change for each eruption type independently, assuming a sphere radius of 100 m. The best-fit location for the ordinary explosion is estimated beneath the summit crater area at 500 m a.s.l. (depth of ∼280 m), which is only one grid lower (-50 m) than that for paroxysm (550 m). For lava effusion, the best-fit model is located horizontally ∼150 m apart from the central crater. Although these independent inversions do not show exactly the same location, which suggests that the pressure source of these eruptions is commonly

located at a range of shallow (<∼400 m depth, >400 m a.s.l.) portion of magma plumbing system beneath the summit crater area (<∼200 m from the central crater). Secondly, we conduct joint inversion of ordinary explosion and paroxysm. The best-fit sphere model is estimated at the same location as that of the ordinary explosion case. Ellipsoidal models are further calculated to evaluate if they can improve the fitness of tilt vectors. This results in $100 \times 150 \times 100$ m ellipsoid, which however indicates a trade-off between the source volume and the pressure change. We also show that this ellipsoidal source can also well reproduce the deflation during lava effusion.

In Chapter 5, we first demonstrate the reliability of our results of the pressure source estimation, that is, geometry and the amount of depressurization induced by lava drainage from the conduit, referring to caldera-forming effusive eruption. From comparison with an analogue experiment of caldera collapse and an dynamic model of a gravity-driven lava effusion, we interpret our estimated source as a shallow magma reservoir to which the uppermost eruptive conduits (radius of ∼2.5 m) are connected or the upper part of the feeding conduit (∼100 m) filled with gas-poor and crystal-rich magma (Highly Porphyritic, HP magma). We further model the pressurization processes of the shallow magma reservoir and conduit that include magma-static pressurization and flow-driven pressurization, which relates the estimated pressure changes to the physical parameters of magma discharge (i.e. volume discharge and exit velocity). We demonstrate that pressurization before an ordinary explosion (2.6 kPa) can be explained as the magma-static pressure change due to magma surface uplift driven by a magma ascent constantly supplied from a deeper portion. On the other hand, pressurization before paroxysm (3.9 MPa) reflects the flow-driven pressure change that is generated by a rapid upward migration of magma into conduits. We also propose a real-time calculation method for tilt signals from seismometers, which may be a possible option for ground deformation monitoring and hazard migration system. We then outline several future perspectives.

In this thesis, we have examined ground deformation associated with different-type eruptions at Stromboli volcano based on data analyses and modelling using near-vent tilt sensors. Our main finding is that, in spite of different magma properties and eruptive intensity, ground deformations induced by different-type eruptions (ordinary explosion, paroxysm and lava effusion) are caused by a common pressure source at a shallow depth beneath the vent. This mechanical similarity may be a factor controlling the scale-invariance of pre-explosive inflations of ordinary and paroxysmal explosions. Moreover,

we show the difference between ordinary and paroxysmal explosions, that is, the pressurization mechanisms (magma-static or flow-driven pressurization) of the source. Our result can be helpful in revealing the eruption dynamics of Stromboli volcano, and it will lead to a fundamental understanding of the magma ascent dynamics of volcanic eruptions.

Contents

Chapter 1

Introduction

1.1 Review of the ground deformation studies on volcanoes

The transport of volcanic fluids such as magma and hydrothermal fluids associated with volcanic eruptions causes pressure changes in volcanic chambers (reservoirs), conduits and dykes. This underground pressure change is exerted on the surrounding host rock, which generates elastic deformation of the ground. The ground deformation can be measured by geodetic observation techniques, for example, Global Navigation Satellite System (GNSS), Synthetic Aperture Rader (SAR), leveling, tilt and strain. In order to mechanically understand such geodetic observations and interpret underground volcanic phenomena as an inverse problem, research on the mathematical model of the volcanic pressure source and its application to observational ground deformation data have been conducted.

1.1.1 Classic ground deformation models and case studies

A spherical pressure source model in a semi-infinite elastic isotropic homogeneous medium is the simplest pressure source model, called the Mogi model (Mogi, 1958[132]), and has been widely used for the analysis of volcano deformation. Mogi (1958)[132] applied the analytical solution of ground displacement derived by Yamakawa (1955)[209] to the subsidence before and after the 1914 Sakurajima Taisho eruption and the 1924 Hawaii Kilauea eruption. The model describes the ground deformation due to a small spherical pressure source inside an elastic homogeneous half-space medium. This pressure source model represents the pressurization or depressurization of a buried magma chamber under the ground. As for the application to Sakurajima, Mogi (1958)[132] demonstrated that leveling result around Kagoshima bay is well reproduced by a source at a depth of 10 km.

Although the model contains several simplifications and assumptions, it has been successfully applied to many cases of volcano deformation so far. McTigue (1987)[126] derived higher-order terms for ground surface displacement due to spherical pressure sources by imposing stress boundary conditions at the surface of the spherical shell and the ground surface. This model releases a limitation of the Mogi model that assumes the radius of source is smaller than the depth of the source. Host rock surrounding a magma chamber is considered to behave as viscoelastic material because of the heat transfer from high-temperature ($\sim 1000\mathrm{C}^{\circ}$) magma (Dragoni and Magnanensi, 1989[62]; Segall, 2016[178]). Dragoni and Magnanensi (1989)[62] investigated the effect of the viscoelasticity of rocks around a magma chamber on crustal deformation by measuring the pressure change when a spherical pressure source in an elastic body is surrounded by a Maxwell viscoelastic shell. They showed that the pressure increase of the pressure source does not appear in the deformation of the ground surface due to the effect of viscoelastic relaxation.

In the case of a spherical pressure source, the volcanic deformation field appears as a point-symmetric field with respect to the pressure source. However, in practice, anisotropic volcanic deformation is also observed. For those cases, spheroidal or ellipsoidal pressure sources can be used as a pressure source. Davis (1986)[58] derived an approximate solution for ground displacement when an ellipsoidal pressure source can be assumed to be a point source, based on Eshelby's (1957)[65] elastic field due to ellipsoidal pressurization in a semi-infinite elastic medium. Yang et al. (1988)[210] obtained an analytical solution for the pressure variation of a finite-sized spheroidal pressure source. Amoruso and Crecentini (2013)[7] obtained an analytical solution for surface displacement caused by an ellipsoidal pressure source of arbitrary shape and finite size. Bonaccorso et al. (2005)[36] applied the ellipsoidal pressure source of Davis (1986) and the spheroidal pressure source of Yang et al. (1988)[210] to ground deformation data measured by using EDM (Electro-optical Distance Measurement) and GPS during the expansion period of Etna from 1993 to 1998.

Once pressurization within a magma chamber due to magma supply and accumulation reaches a critical value to break the wall rock, fractures are generated, and magma propagates within the rock as dykes (vertical cracks) or sills (horizontal cracks). This volcanic phenomenon can be represented as an opening or closing of faults (cracks). The surface displacement, strain and tilt due to the opening of rectangular faults were summarized by Okada (1985)[141]. Okada (1985)[141] formulated analytical solutions for surface displacements, strains, and tilts associated with discrepancies and openings of point sources

with arbitrary strike and dip angles in the body and rectangular faults of finite length. Okada and Yamamoto (1991)[143] applied this model to the crustal deformation associated with the Ito-oki submarine eruption in 1989. They showed that it was explained by the combination of an aperture fault and a strike-slip fault. The displacement field of the opening crack is relatively small along the strike direction but large in the normal direction to the fault. Subsidence occurs above the fault, and it reaches the largest at a certain distance from the fault. Okada (1992)[142] extended Okada (1985)[142] to formulate displacement, strain, and tilt at the ground surface and arbitrary depths. Fialko et al. (2001)[67] obtained a semi-analytical solution for surface displacement caused by a disk-shaped pressure source such as a sill. They showed that vertical displacement is similar to a spherical source, but the horizontal displacement was relatively small. This implies that vertical and horizontal displacement data are necessary to distinguish between spherical and sill-like sources.

Volcanic eruptions of volcanoes that are dormant for a long time are generally initiated as a dyke reaches the surface (volcanic vent). When the magma flows within the conduit for a long time or eruptive activity is stabilized (e.g. intermittent sequence of repetitive eruptions), the conduit geometry transforms from dyke-like shape to a cylindrical shape. Ground deformation models that consider a cylindrical pressure source representing such volcanic conduit have also been developed and applied to inflation and deflation before and after volcanic eruptions. Walsh and Decker (1971)[205] obtained the ground displacement due to a pipe-shaped pressure source by integrating the effect of a spherical pressure source aligned in the depth direction in a semi-infinite elastic body. Bonaccorso and Davis (1999)[37] derived the surface displacement due to a cylindrical pressure source for the case of Poisson's ratio $\nu = 0.25$ for both open and closed types. A general expression, including cases other than $\nu = 0.25$, was given by Segall (2010)[176]. Bonaccorso (2006)[33] used an open-type model to analyze tilt changes associated with lava fountain eruptions that occurred on Mt. Etna from 1998 to 2000. They estimated the conduit length of 1.5–1.9 km and the radius of 5–8 m. Nishimura (2009)[137] derived the ground surface deformation due to the normal stress and shear stress exerted on the conduit wall by the magma rising in the conduit, and investigated the temporal change of the volcano deformation due to gas bubble growth in magma.

1.1.2 Recent development of volcano deformation measurement

Observations of volcanic eruptions have been conducted since the beginning of the 20th century using techniques such as leveling, EDM, strain gauges, and tiltmeters (Dzurisin, 2007[64]). With the development of satellite geodetic technology using GNSS and interferometric synthetic aperture radar (InSAR), it has become possible to observe surface displacements with few milimeters over timescales ranging from days to decades (e.g. Pinel et al., 2014[152]) Recently, these two space-geodetic techniques have been the mainstream of volcano deformation measurement (Freymueller et al., 2015[71]; Ferenandez et al., 2017[66]). This development has enabled us to detect ground deformation associated with large-scale eruptions and volcanic unrest in a wide range of spatial and temporal scales, even at "hidden" active volcanoes in a remote area, which results in drastic increase in the number of volcanoes at which deformation has been detected (e.g. Hooper et al., 2012[90]; Biggs et al., 2014[28]; Biggs and Pritchard, 2017[29]).

However, small repetitive eruptions such as Strombolian and Vulcanian eruptions, non-explosive eruptions that form lava domes or flows, and phreatic eruptions generate relatively small amplitude of volcanic deformation in a short time scale. Therefore, measurement techniques with high sensitivity and high time resolution, for example, strainmeters and tiltmeters, are suitable for observing these small-scale eruptions. Observations using tiltmeters and strainmeters enable us to detect tiny signals (micro or nano, 10^{-6}–10^{-9} strain or radian) even in the short-term range of a few seconds to tens of minutes. Recently, power saving and miniaturization of tilt and strain instruments, and the development of retrieval methods of tilt components from broadband seismometers (e.g., Wielandt and Forbiger, 1999[206]; Aoyama and Oshima, 2008[16]) have allowed capturing the volcano deformation associated with small-scale eruptions near the eruptive vents. This has made it possible to discuss the behaviour of subsurface volcanic fluids immediately before and after an eruption.

Ground deformations associated with effusive (lava dome-building and lava flow) eruptions have been observed in silicic and basaltic volcanoes. As a case study of lava dome-building eruptions, we introduce the eruption of Soufriere Hills volcano, Montserrat, beginning to erupt in 1995. This event was characterized by a series of lava dome formations and subsequent dome collapse and pyroclastic flows (Sparks and Young, 2000[181]; Wadge et al., 2014[204]). In 2003, strainmeters (Sacks-Everson dilatometers) have captured the pressurization of a magma source at $\sim$5 km depth over a duration of a few hundred sec-

onds after the collapse of a lava dome (Voight et al., 2006[203]; Linde et al., 2010[112]). The collapse of the lava dome caused rapid depressurisation, which is inferred to have led to rapid bubbling in a magma chamber at the depth. Another example is Mount St Helens, which exhibited a series of non-explosive eruptions producing a lava dome between 2004 and 2008 (Iverson et al., 2006[96]; Sherrod et al., 2008[179]). Anderson et al. (2010)[9] used borehole tiltmeters deployed in the vicinity of the lava domes and found a cycle of rapid uplift toward the vent followed by gradual subsidence in correlation with volcano-tectonic earthquakes. This tilt variation is considered to be caused by the stick-slip behaviour of the magma column rising in the shallow part of the conduit. In the case of lava flow eruption, tiltmeters located near the Halemaumau crater and in the East Rift Zone of Kilauea volcano have observed intermittent uplift-subsidence in tilt linked to the height of the lava lake (Cervelli and Miklius, 2003[131]; Anderson et al., 2015[14]; Patrick et al., 2016[149]). Tiltmeters located in the East Rift Zone showed delays of a few minutes to a few hours, which may indicate the subsurface horizontal magma transport from the summit crater area to the lava effusive vent.

Ground deformations associated with explosive eruptions have also been observed in volcanoes characterized by repetitive or small eruptions (i.e. Vulcanian and Strombolian eruptions). The physical processes of Vulcanian eruptions are better understood through tilt and strain observations in the vicinity of the crater at volcanoes, for example, Sakurajima (Iguchi et al., 2008[93]; 2013[92]), Suwanose-jima (Nishimura et al., 2013[140]), Semeru (Nishimura et al., 2012[139]), Santiaguito (Johnson et al., 2009[100]). Kamo and Ishihara (1989)[101] and Ishihara (1990)[95] conducted observations using strain gauges and water-tube tiltmeters at the Mt Haruta shaft of Sakurajima volcano, and reported that the expansion of the volcano edifice precedes a Vulcanian eruption by tens of minutes to hours, and the contraction after the eruption. Ishihara (1990)[95] analysed the pressure source of the mountain expansion preceding the eruption using the Mogi model and showed that the expansion occurred at a depth of 2–6 km. Tateo and Iguchi (2009)[192] studied the tilt and strain of Strombolian and Vulcanian eruptions with BL-type earthquakes and repeated ash ejections at Sakurajima. They found that, although the amount of ground deformation is the same for Vulcanian and Strombolian eruptions, the Vulcanian eruption is accompanied by rapid ground deformation immediately before the eruption, while the Strombolian eruption is accompanied by rapid ground deformation. This difference may reflect the fact that the uppermost part of the crater is closed in the case of Vulcanian

eruptions, whereas it is open in the case of Strombolian eruptions. For the Strombolian eruptions, Genco and Ripepe (2010)[76] reported the inflation-deflation cycle of ground tilt beginning a few hundred seconds before the eruption. Tiltmeters and seismometers have also contributed to capturing small deformations associated with geyser eruptions (Nishimura et al., 2006[138]; Vandemeulebrouck et al., 2014[199]) and phreatic eruptions (Aoyama and Oshima, 2008[16]; 2015[17]; Maeda et al., 2017[115]; Honda et al., 2018[89]; Terada et al., 2021[193]; Takahashi et al., 2022[189]). Maeda et al. (2017)[115] analyzed tilt signals immediately ($\sim$ 450 s) before the eruption onset of Mt. Ontake in 2014. They estimated the pressure source as a vertical tensile crack at a depth of 1100 m and showed the transition of ground inflation from linear to exponential. This initial linear phase is explained as the boiling of underground water controlled by constant heating, while the exponential phase is induced by decompression boiling of water. In this way, the development of observation technology has made it possible to capture volcanic deformation that reflects pressure changes in the shallow part of the volcanic edifice before and after an eruption. Particularly, high-precision measurements using tilt and strain instruments have improved our understanding of the dynamics of magma or fluid transport before explosive eruptions.

1.1.3 Recent development of volcano deformation modelling

As described above, theoretical models of elastic deformation on the surface have been applied to field measurement data. Although these analytical formula successfully reproduce the ground deformation field in many cases and do not require high calculation costs, sometimes it is necessary to consider the influence of the mountain topography because the analytical solutions are derived under the assumption of a semi-infinite plane surface. The simplest way to correct the topographic effect is to set the elevation of the free surface at a certain reference elevation (reference elevation model, Cayol and Cornet, 1998[48]; Williams and Wadge, 2000[208]). Another way is the varying-depth model (Williams and Wadge, 1998[207]). In this model, the ground surface is set for each observation point by taking the apparent depth of the pressure source as the difference from the altitude of the observation point. Williams and Wadge (1998)[207] compared these correction methods for the analytical model with a finite element model, and showed that vertical displacement and tilt are well reproduced by the varying-depth model, while horizontal displacement is well reproduced by the reference elevation model. Also, analytical models

assume homogeneous media, although Earth's underground structure is heterogeneous.

To fully take the complex effects of surface topography and subsurface structure into account, numerical methods such as the finite element method (FEM) and the boundary element method (BEM) have been applied thanks to the development of computational techniques and resources. Cayol and Cornet (1997)[47] developed a 3-D mixed boundary element method (MBEM). This model has been applied to modeling of Merapi volcano (Beauducel and Cornet, 1999[25]) and Piton de la Fournaise volcano (e.g. Fukushima et al., 2005[72]; 2010[73]; Dumont et al., 2022[63]). Fukushima et al. (2005)[72] used the MBEM for analysis of SAR observation data during the 2000 eruption of the Piton de la Fournaise volcano(Reunion island) and they showed the pressure source could be modelled as complex dykes. Bonaccorso et al. (2005)[36] compared several analytical models with the 3-D finite element model of Mt. Etna to the inflation episode in 1993-1997 to include the topography and the seismic velocity structure obtained by seismic tomography. Some studies using a finite element model (e.g. Ronchin et al., 2015[172]; Marsden et al., 2019[119]; Anderson et al., 2020[8]) demonstrated that derivatives of surface displacement (i.e. tilt and strain) were more affected by the local gradient of surface topography such as caldera rims. Finite element method is also useful to solve the ground deformation of heterogeneous medium (Hickey and Gottsmann, 2015[87]; Gottsmann et al., 2020[80]; Hickey et al., 2022[88]), complex geometry of pressure source (Hautmann et al., 2009[86]), and estimation of the stress field (Albino et al., 2018[4]; 2019[5]). Recently, these numerical models have been applied for coupled problems of ground deformation with gravity fields (Currenti et al., 2007[55]; 2008[56]), hydrothermal processes (Stissi et al., 2021[183]; Arens et al., 2022[18]), and conduit flow (Albino et al., 2011[6]; Kawaguchi and Nishimura, 2015[102]; Marsden et al., 2019[120]).

1.1.4 Integration with non-geodetic measurements and physics-based model of volcanic eruption

Volcano deformation studies essentially solve an inverse problem to estimate mechanical information of volcanic eruptions as a pressure source. However, ground deformation is proportional to the moment of the source, that is, the product of the pressure change and the source volume. This thus means that these two parameters are not able to be separated. In this case, to constrain them independently, it is important to use ground deformation with independent non-geodetic observation (e.g. magma discharge during a

volcanic eruption: flux, volume, velocity) and mathematical models of magma dynamics within the chamber, conduit and dyke. Moreover, The combined usage of a mathematical model including the physical process of magma dynamics made it possible to estimate geochemical parameters in the model.

In recent years, with the availability of real-time measurements of volcanic plume height and effusive lava dome or flow volume using satellite-based and meteorological radar, some studies have compared estimates of geodetic volume changes associated with eruptions with measurements of eruptive volumes (Mastin, 2008[122]; Kozono et al., 2013[104]; 2014[105]; Hreinsdóttir et al., 2014[91]; Bato et al., 2019[23]). Kozono et al. (2013[104], 2014[105]) estimated eruption rate during the 2011 eruption of Kirishima Shinmoe-dake volcano using geodetic magma chamber volume and lava volume measured by SAR satellite imaging, and also combined with meteorological radar observations. Hreinsdóttir et al. (2014)[91] conducted simultaneous satellite-based measurements of plume height with exponential-decaying ground deflation during the 2011 eruption of Grimsvotn volcano, Iceland. They showed that the magma chamber at 1.7 km below the surface depressurised in correlation with the eruption rate decaying exponentially. Recently, quantitative integration with simultaneous non-geodetic observations through physics-based modelling provided a probabilistic estimation of model parameters like chamber volume and magma properties (density, viscosity and vesicularity) (Anderson and Segall, 2011[10], 2013[11]; Segall, 2013[177]; Anderson and Poland, 2016[13]; Anderson et al., 2019[12]). Anderson and Segall (2011[10], 2013[11]) applied the Markov chain Monte Carlo (MCMC) method to GPS data of the 2004 lava dome eruption of Mount St Helens to estimate the geometry of magma chamber and magma properties by combining a physics-based conduit flow model of effusive silicic eruption.

1.1.5 Summary

Ground deformation associated with volcanic eruptions can be used to estimate information on volcanic pressure sources, which is a key to infer the dynamics of subsurface magma movement. Measurement techniques of ground deformation and theoretical models that predict surface deformation caused by pressurization or depressurization of an underground geodetic source have been developed and applied to volcanic eruptions worldwide. Recently, the number of geodetic data has been increasing due to the development of multiparametric measurement techniques with a focus on space-based techniques (GNSS

and SAR). On the other hand, high-precision measurements using strainmeters, tiltmeters (and seismometers) have captured short-term (seconds to hours) ground deformation associated with small-scale eruptions, which contributes to understanding the dynamic process of volcanic eruptions. Numerical modelling of ground deformation with FEM or BEM enables us to take topographic effects into account. Besides, simultaneous measurement of ground deformation and non-geodetic parameters such as magma discharge such as volume (/flux) allows us to independently constrain the pressure change of the geodetic pressure source, which can not be estimated by a geodetic inversion itself in general.

1.2 Review of the typical eruptive activity of Stromboli volcano, Italy

Stromboli volcano is a basaltic stratovolcano in the Aeolian archipelago, Tyrrhenian Sea, Italy, and one of the world's most active and monitored volcanoes. Stromboli volcano exhibits a variety of volcanic eruption types with different intensities and explosivities (Figure 1.1).

Ordinary eruptive activity of Stromboli is intermittent mild explosions well-known as "Strombolian" eruptions worldwide (Barberi et al., 1993[20], Figure 1.1b), which explosively emit volcanic jets of gas and incandescent magma fragments within a few seconds (<5 s) at a rate of ∼13 events per hour (Ripepe et al., 2008[162]). This eruption style is typical for basaltic to basaltic andesite volcanoes over the world, such as Stromboli (Italy), Etna (Italy), Yasur (Vanuatu), Erebus (Antarctica), Batu Tara (Indonesia), Fuego (Guatemala), Villarrica (Chile), Shishaldin (Alaska), Aso (Japan). At Stromboli, this recent activity is persistent and has been inferred to have continued for at least 1,300–1,700 years (Rosi et al., 2000[173]; Rosi et al., 2013[174]), only occasionally being interrupted by effusive eruptions (Barberi et al., 1993[20], Figure 1.1c), and by larger-scale and more violent explosions, called major and paroxysmal explosions (paroxysm, Figure 1.1d). Eruptive activity of Stromboli is thus generally categorized into four types: "ordinary explosion", "major explosion", "paroxysm" and "lava effusion" (e.g. Rittmann, 1931[168]; Barberi, 1993[20]; Harris and Ripepe, 2007[83]). Different scales of explosive activity also involve different magma and thus the origin of this variety of activity is still debated.

The magma plumbing system of Stromboli is divided into shallow and deep magma storage zones from petrological analyses. The shallow storage is located at <3 km b.s.l.

and is filled with high porphyritic (HP), volatile-poor (<0.5 wt%), crystal-rich (50 vol%), high-density (2700 kg/m^3) magma. This HP magma is ejected as scoria during ordinary Strombolian eruptions or is effused as a lava flow (Métrich et al., 2001[128]; Francalanci et al., 2004[70]; Landi et al., 2006[108]; Burton et al., 2007[40]). Seismic studies imaged this structure as a NE-SW aligned dyke-conduit system extending to ∼1 km b.s.l. (Chouet et al., 2003[51]; 2008[50]; Marchetti et al., 2009[117]). The deep storage is located at a depth of ∼7–10 km b.s.l. and is composed of low porphyritic (LP), volatile-rich (3–4 wt%), crystal-poor (<10 vol%), low-density (2500 kg/m^3) magma that generates short-lived major and paroxysmal explosions (Métrich et al., 2010[127]; Aiuppa et al., 2010[2]; Métrich et al., 2021[129]). These shallow and deep magma storages are inferred to be connected with each other by a near-vertically elongated pressure source at 2.6 km that is suggested to have generated ground deflation during the 2007 effusive eruption (Bonaccorso et al., 2008[39]).

The ordinary explosion is characterized by a small volume of ejected materials (1–30 m^3: Ripepe et al., 1993[167]; Patrick et al., 2007[148]; Gaudin et al., 2014[75]; Bombrun et al., 2015[31]) and a plume height of less than about 150 m (e.g. Ripepe et al., 2008[162]; Tadeucci et al., 2013[188]; Gaudin et al., 2017[74]). The ordinary explosions are often explained by the gas slug model (e.g. Jaupart and Vergniolle, 1988[98]), where tiny gas bubbles accumulate at the roof of a magma reservoir (Jaupart and Vergniolle, 1988[98]; 1989[99]; Ripepe et al., 2001[158]) or progressively coalesce during ascent from a deeper part (Parfitt and Wilson, 1995[145]; Parfit, 2004[146]). Then the accumulated gas ascends as a slug through a conduit filled with low-viscous magma, and the gas slug bursts at the free surface of magma, generating acoustic and seismic emissions (Chouet et al., 1974[52]; Blackburn et al., 1976[30]; Ripepe, 1996[166]; Vergniolle and Brandies, 1996[200]; Vergniolle et al., 1996[201]). Broad-band seismic observations have captured the very-long-period (VLP) signals associated with each explosion (e.g. Neuberg et al., 1994[136]; Chouet et al., 2003[51]; 2008[50]; Auger et al., 2006[19]; Giudicepietro et al., 2009[78]; Sugimura et al., 2021[185]; Legrand and Perton, 2022[111]). The source locations of the VLP signals were suggested to represent the location of a rising gas slug at a depth of ∼300 m from the vent at ∼200 m west of the NE crater by applying a seismic waveform inversion (Chouet et al., 2003[51]). Recently, Sugimura et al. (2021)[185] analyzed a very-near-field seismic data using the moment tensor inversion and semblance analysis to locate the VLP source at a depth of ∼ 180 m and 150–200 m west/southwest of the

crater. They also found a preceding phase in the VLP signal 10–20 s before the explosion onset at the vent and its lateral migration of about 50 m, which is suggested to reflect a bending of the shallow feeding system towards the northeast. Thanks to these studies of seismo-acoustic and visual observations, shallow ($<\sim$ 200 m depth) conduit dynamics $<\sim$20 s before the ordinary explosions have been quantitatively investigated (Harris and Ripepe, 2007[83]; Gurioli et al., 2014[82]).

At Stromboli, ground tilt appears as inflation-deflation cycles associated with ordinary explosions (Genco and Ripepe, 2010[76]; Ripepe et al., 2021b[160]). Each explosion is preceded by gradual exponential inflation ($\sim$200 s) which is followed by a rapid deflation associated with the emission of gas and magma fragments always longer than the explosion itself (Ripepe et al., 2021b[160]). The progressive ground inflation is interpreted to be generated by magma ascent in the conduit forced out by gas bubble growth (Nishimura et al., 2009[137]; Genco and Ripepe, 2010[76]; Ripepe et al., 2021a[163]). Since ordinary explosions are often interpreted by the gas slug model, Kawaguchi and Nishimura (2015)[102] calculated ground tilt induced by a gas slug ascending in a vertical conduit using a model of James et al. (2008)[97]. Their simulation shows that a gas slug moving in the conduit acts as a deflation source rather than inflation, suggesting a need to modify the gas slug model. Recent laboratory analogue experiments presented that gas-poor, crystal-rich nature of magma in the shallow system may significantly affect gas bubble behaviour in the final part of the conduit and thus eruptive dynamics. The existence of a viscous cap at the top of the conduit has been suggested to explain the observed dynamics (Gurioli et al., 2014[82]; Capponi et al., 2016a[45]; 2016b[45]; 2017[44]; Oppenheimer et al., 2020[144]). Gas bubbles may be trapped beneath a plug of crystal mush, forcing their coalescence into the conduit to generate an eruption (Suckale et al., 2016[184]; Barth et al., 2019[22]; McKee et al., 2022[125]). Although Genco and Ripepe (2010)[76] documented the time series of the inflation-deflation cycles reflecting the underground gas/magma movement, they did not estimate the pressure source using fundamental geodetic inversions. Therefore, a detailed analysis of the gradual inflation and estimation of its pressure source is very important for understanding the dynamics of gas and magma ascent before ordinary explosions.

At Stromboli, also the lava effusions episodically interrupt the ordinary activity with a frequency of 5–15 years (Barberi, 1993[20]). The latest notable events occurred on 28 December 2002, 27 February 2007 and 7 August 2014 (Pioli et al., 2008[155]; Barberi

et al., 2009[21]; Valade et al., 2016[198]). Common precursors of these events can be observed several months before the effusion onset and are characterized by the increases in tremor activity, VLP amplitude and acoustic emission (e.g. Burton et al., 2008[41]; Martini et al., 2007[121]; Ripepe et al., 2009[159]; Valade et al., 2016[198]), as well as inflation of the summit crater area and the slope of Sciara del Fuoco detected by GB-InSAR (e.g. Tarchi et al., 2008[191]; Casagli et al., 2009[46]; Di Traglia et al., 2014[61]), which reflects the increase of magma supply in the shallow feeding system. About ∼12-15 h before the onset, ground inflation of the volcano edifice is detected by tiltmeters (Marchetti et al., 2009[117]; Valade et al., 2016[198]), which coincides with the increase in the rockfall (landslide) activity and the related seismicity besides infrasound and thermal activity transition at the summit eruptive vents (Ripepe et al., 2009[159]). Lava effusion is initiated by slope failure induced by a lateral dyke intrusion (Tommasi et al., 2008[197]; Barberi et al., 2009[21]; Valade et al., 2016[198]). After the onset, the progressive collapse of the summit crater wall and the progressive decrease in effusion rate (Spampinato et al., 2008[180]; Neri and Lanzafame, 2009[135]; Valade et al., 2016[198]), accompanied by exponential deflation of ground tilt (Bonaccorso et al., 2008[39]; Marchetti et al., 2009[117]; Valade et al., 2016[198]). On 30 December 2002, 2 days after the 28 December 2002 lava effusion, this high slope stability caused a limited landslide of the Sciara del Fuoco that triggered a ∼10 m high tsunami wave hitting the northern coast of the island (Tinti et al., 2003[195]; Tinti et al., 2008[196]). Magma level decrease caused by lava discharge is tracked by the polarization analysis of the VLP signals (Marchetti and Ripepe, 2005[118]; Giudicepietro et al., 2009[78]; Ripepe et al., 2015[161]). These syn-effusive phenomena are comprehensively explained by a model of lava drainage from the upper conduit beneath the summit area caused by the gravity of magma above the effusive vent (Ripepe et al., 2015[161]). This model suggests the existence of shallow magma storage at shallow (<500 m depth) magma system, although a geodetic pressure source generating the syn-effusive ground deflation has not yet been estimated.

Paroxysms and major explosions are more energetic than ordinary explosions. The term "paroxysm" is an ambiguous and local definition from Barberi (1993)[20] and subsequent literature has continued to use it, which is different from the classical terms of volcanic eruption types (Figure 1.1). Several studies suggest that paroxysms at Stromboli can be defined as the Vulcanian eruption in style (Calvari et al., 2006[43]; D'Auria et al., 2006[57]; Giordano and De Astis, 2021[77]), although it has several points different from

classical Vulcanian eruptions observed at, for example, Sakurajima (Japan) and Santiaguito (Guatemala). Indeed, paroxysms have similar characteristics to Vulcanian eruptions (Clarke et al., 2015[53]) such as short-lived (few minutes), vent clearing, cannon-like blasts, sometimes associated with pyroclastic flows and phenomenologically identical to Vulcanian eruptions (Giordano and De Astis, 2021[77]). Paroxysm is characterized by large volumes of ejected material ($> 10^4$ m^3), convective plumes rising to several kilometres (>3 km) above the vents and tsunamigenic pyroclastic flows running down the Sciara del Fuoco (e.g. Harris et al., 2008[84]). Several studies classify volcanic eruption types based on the volume discharge and the duration of single eruption (e.g. Tadeucci et al., 2015[187]); Figure 1.1a). In the aspects of the volume discharge ($> 10^4$ m^3) and the duration (few minutes), therefore, paroxysms share the same range as the Vulcanian eruption. Major difference between them is the mechanical process that confines overpressure beneath the surface. For Vulcanian eruption, formation of plug (or cap) at eruptive vent by magma cooling and solidification, which generates the overpressure beneath the plug until it reaches a failure strength of rock. On the other hand, because Stromboli's upper conduit is filled with relatively less-viscous magma, flow resistance is considered to play a roll to generate the overpressure, which is interpreted as a "weak plug" (Oppenheimer et al., 2020[144]). Paroxysms are quite rare (Bevilaqua et al., 2020[27]), but four paroxysmal events occurred in the last two decades (5 April 2003, 15 March 2007, 3 July 2019 and 28 August 2019) and are investigated by multidisciplinary studies (e.g. Calvari et al., 2006[43]; Barberi et al., 2009[21]; Ripepe and Harris, 2008[162]; Pistolesi et al., 2011[156]; Andronico et al., 2013[15]). Three paroxysms in 2003, 2007 and 28 August 2019 occurred at the final stage of lava effusions initiated by dyke intrusions at the mountain flank. Therefore, it is inferred that a certain amount of magma is withdrawn from the upper conduit and decompress the shallow magma reservoir. As a result, volatile-rich magma is raised from the deeper storage to generate paroxysm (Aiuppa et al., 2010[2]; Calvari et al., 2011[42]; Ripepe et al., 2015[161]; Ripepe et al., 2017[165]). This type of paroxysm triggered by such shallow process is called a "top-down paroxysm" (Aiuppa et al., 2021[3]). The 3 July 2019 paroxysm is accompanied by small lava pouring from the vents, which, however, is the only one among the four events that unexpectedly occurred without the large-scale flank lava effusion. This type is, contrarily, called a "bottom-up paroxysm" (Aiuppa et al., 2021[3]). The 28 August paroxysm occurred at the end of the lava-effusive phase subsequent to the 3 July paroxysm (Plank et al., 2019[157]; Aiuppa et al., 2021[3];

Laiolo et al., 2022[106]). Continuous measurement of persistent volcanic gas compositions and fluxes have revealed that that the two paroxysms in summer 2019 were preceded by detectable escalations in volcanic plume CO_2 degassing several weeks to months beforehand (Inguaggiato et al., 2020[94]; Aiuppa et al., 2021[3]). Petrological analyses on scoria and pumice ejected during paroxysms confirms the timescales of magma ascent and the envolvement of mafic (LP) magma that are recharged from deeper part (Métrich et al., 2021[129]; Pichavant et al.,2022[151]; Petrone et al., 2022[150]). These geochemical studies have provided the evidence of preceding magmatic processes at a deeper part a few days to month before the paroxysms that do not clearly appear in surface eruptive activity or geophysical monitoring parameters. As a shorter-term precursor, geophysical studies reported that ground deformation emerges several minutes to hours before paroxysms (Giudicepietro et al., 2020[79]; Di Lieto et al., 2020[60]; Viccaro et al., 2021[202]; Ripepe et al., 2021a[163]; Mattia et al., 2021[123]). Ground deformation preceding paroxysms was detected by strainmeters at ∼60 min before the eruption onset (Giudicepietro et al., 2020[79]; Di Lieto et al., 2020[60]). At ∼10 min before the onset, rapid strain and tilt change indicating cvolcano inflation was also detected (Viccaro et al., 2021[202]; Ripepe et al., 2021a[163]; Mattia et al., 2021[123]). However, in spite of the different origins of involved magma from HP (ordinary explosion) to LP (paroxysm), the ground deformation associated with the paroxysm shares the same exponentially increasing inflation as for the major and ordinary explosion, suggesting the scale-invariant conduit process of the explosive dynamics at Stromboli volcano (Ripepe et al., 2021a[160]). Therefore, similarities and differences in the ground deformation among these different-scale explosions are key to understanding their eruptive dynamics and triggering mechanisms.

1.3 Motivation and objective of the doctoral thesis project

1.3.1 Volcanological background and significance of Stromboli volcano

Volcanoes show various eruption types that must be due to different physical processes from effusive (e.g. lava flow, lava dome) to explosive (e.g. Hawaiian, Strombolian, Vulcanian, Plinian and phreatic) dynamics. These differences are primarily controlled by magma properties (e.g. basaltic, andesitic and silicic) and magma ascent process and fluid-solid interaction underground. It is important to understand the mechanisms of various volcanic eruptions and their activity change for forecasting volcanic eruptions and

temporal evolution of subsequent volcanic crises. However, the mechanism of volcanic eruption and its variety have not been well understood mainly because of two reasons. First, we have not met with many cases of volcanic eruptions enough to understand their mechanisms, as the occurrence of volcanic eruptions is generally less frequent and contemporary measurement techniques have been developed in these decades. Second, although the location where volcanic eruptions occur (volcanic vent) can be relatively predictable, tough environment of mountains and dangerous eruptions hinder field measurement near the volcanic vent. Therefore, it is important to study highly active and accessible volcanoes to obtain fundamental knowledge applicable to other volcanoes or valuable for a general understanding of the mechanism of volcanic eruptions.

Stromboli volcano, Italy, is one of the "natural laboratories" of basaltic eruptions (e.g. Hawaiian eruption, Strombolian eruption, lava flow and basaltic explosive eruption) alongside Kilauea volcano (Hawaii) and Mt. Etna (Italy) (Tadeucci et al., 2015[187]). At these volcanoes, thanks to their high activity of repetitive eruptions and relatively good accessibility, permanent multiparametric geophysical and geochemical measurement networks with a broad range of sensors (e.g. geodetic, seismic, acoustic, visible, infrared, electromagnetic and gravimetric, ultraviolet) are deployed to monitor volcanic activity and signals of eruptions. The combined use of these measurement techniques provides an integrated understanding of the geometry of the volcanic system and the dynamics of volcanic eruptions (e.g. Harris and Ripepe, 2007[83]) that cannot be revealed by an individual measurement approach. Among these three volcanoes, Etna and Kilauea are thousands of meters-high basaltic shield volcanoes, and their eruptive activity is characterized by general basaltic activities, for example, Hawaiian eruption (lava fountain), Strombolian eruption, and effusive lava flow. Stromboli is a 925 m-high basaltic stratovolcano island and exhibits slightly different activity: Strombolian eruption and effusive lava flow, typical basaltic activity, and also paroxysmal explosion (paroxysm), Vulcanian-like violent explosive eruption (Fig. 1.1). Unlike Etna and Kilauea, Stromboli is a relatively small mountain lower than an elevation of a thousand meters, and its active eruptive craters (at 780 m a.s.l.) can be observed from a mountain peak at 920 m a.s.l. This accessibility allows us to install temporary stations at a very close ($\sim$200 m) distance to the active vents and record geophysical signals associated with volcanic eruptions that cannot be easily detected at other volcanoes. Indeed, pioneering studies of geophysical observations at Stromboli volcano have contributed significantly to the advancement of understanding

the dynamics of Strombolian eruption (e.g. Vergniolle et al., 1996[201]; Harris and Ripepe, 2007[83]). Therefore, it can be said that Stromboli is the most ideal target for studying the mechanism of volcanic eruptions, particularly, different-type eruptions with a broad range of magnitude and explosivity.

1.3.2 Previous studies of ground deformation at Stromobli volcano

To study the eruptive mechanisms of Stromboli volcano, we take the approach of ground deformation, which provides information on magma movement beneath the volcanic edifice (Section 1.1). Ground deformation at Stromboli volcano has been monitored since 2002 to present by permanent geophysical networks operated by several research groups in Italy. L'Istituto Nazionale di Geofisica e Vulcanologia (INGV) has operated borehole tiltmeters, borehole dilatometers and GPS stations around the mountainside area (elevation of <200 m a.s.l. and distance of 1–2 km from the vent; Bonaccorso, 1998[32]; Mattia et al., 2004[124]). Laboratorio di Geofisica Sperimentale of the University of Florence (LGS-UNIFI) has operated borehole tiltmeters around the summit area (elevation of >500 m a.s.l. and distance of <1 km from the vent; Marchetti et al., 2009[117]; Genco and Ripepe, 2010[76]). The summit crater zone is surrounded by these geodetic stations, except for the direction of the Sciara del Fuoco, north-west (NW) of the summit area, which is characterized by a steep slope and high instability as rockfalls, landslides, and lava flows frequently occur. In spite of this limitation of access to the NW side, ground-based interferometric synthetic aperture radar (GB-InSAR) has been installed to monitor the crater area and the Sciara del Fuoco slope (Di Traglia et al., 2014[61]). Using these networks, previous studies analyzed ground deformation associated with the different-type eruptions of Stromboli to estimate the geodetic pressure source (e.g. Mattia et al., 2004[124]; Bonaccorso et al., 2008[39]; Ripepe et al., 2021a[163]; Viccaro et al., 2021[202]). Pressure source of ground deflation associated with lava effusion that occurred in 2007 is estimated at a depth of 2.6 km (Bonaccorso et al., 2008[39]), while those of ground inflations preceding paroxysm are estimated at shallower part (depth of < 1 km, Mattia et al., 2004[124]; Ripepe et al., 2021a[163]; Viccaro et al., 2021[202]).

However, there are several problems with these studies (Table 1.2). First, most of the previous studies focused on the individual events of large-scale eruptions: lava effusions (e.g. Bonaccorso et al., 2008[39]; Marchetti et al., 2009[117]) and paroxysms (e.g. Mattia et al., 2004[124]; Bonaccorso et al., 2012[35]; Di Lieto et al., 2020[60]; Viccaro et

al., 2021[202]; Mattia et al., 2021[123]), although Stromboli's regular activity is ordinary (Strombolian) explosions (Genco and Ripepe, 2010[76]). It is necessary to deal with these different-type eruptions systematically, especially ordinary explosions, to achieve a consistent understanding of the dynamics of different eruptions and their activity transition. Second, due to the limitation of the station distributions, few studies analyzed data in near-vent stations (e.g. Genco and Ripepe, 2010[76]; Ripepe et al., 2021a[163]), which is very important to resolve shallow conduit dynamics during magma ascent. Third, most of them modelled ground deformation using analytical solutions derived by assuming an infinite flat surface, although Stromboli's mountain topography is characterized by a steep ($\sim 30°$) slope. These analytical modellings can be performed with a small calculation cost but may produce an inaccurate result. In addition, it is necessary to use a topography-including numerical model for calculating accurate ground deformation generated by a shallow pressure source at a similar level or above the elevation of stations. Only Viccaro et al. (2021)[202] used a numerical model including the effect of topography for inversions of two paroxysms in the summer 2019 and estimated a spherical pressure source above the sea level, that is, at 325 m a.s.l. and 250 m a.s.l., respectively. For these reasons, the volcanic pressure sources of Stromboli volcano, especially at the shallow (>0 m a.s.l.) system, and their similarity and difference among the variety of eruption types are not fully understood and thus necessary to be updated.

1.3.3 Aim and methodology of the thesis

In this thesis, we aim to update the understanding of the volcanic pressure source at Stromboli volcano to propose a comprehensive model for a shallow volcanic system and the mechanism of the different-type eruptions (ordinary explosion, paroxysm and lava effusion). To achieve this goal, we take an integrated approach to the three eruption types, applying the state-of-the-art techniques of ground deformation studies as mentioned in Section 1.1. In Chapters 2 and 3, we show data analyses of ground tilt signals to examine characteristics of ground deformations and derive the measured tilt vectors used for pressure source estimation in Chapter 4. We focus on previous events or periods when most near-vent stations were available. At Stromboli, regardless of the steep topography and tough mountain and island environment, the LGS-UNIFI has installed and maintained the near-vent geophysical monitoring network around the summit area including acoustic, seismic and ground tilt (Ripepe et al., 2004[164]). Thanks to their continuous

effort, geophysical data substantial both in quantity and quality has been recorded over the past 20 years (from 2002 to the present). We also use temporary tilt stations installed during Italy-Japan collaboration research in 2014 and permanent borehole tiltmeters of the LGS-UNIFI multi-parametric network. We further apply a technique to derive tilt signals from broad-band seismometers to compensate coverage of tilt stations. In Chapter 4, we show the estimation of volcanic pressure sources. For calculating theoretical ground deformation, numerical modelling (finite element method, FEM) is used to take volcano topography into account. Then, grid-search-based inversions of the observed tilt vectors for a volcanic pressure source are performed in several steps. Chapter 5 is the discussion. We present an updated picture of the shallow magma system of Stromboli volcano based on an interpretation of our result. We further propose a mechanical model for the pressurization processes to relate the estimated pressure change to physical parameters of magma discharge. This gives posterior support for the robustness of the estimated pressure source parameters. In addition, we demonstrate the usability of seismometers for ground deformation monitoring based on the technique used in our data analysis. Chapter 6 is the conclusions of the thesis.

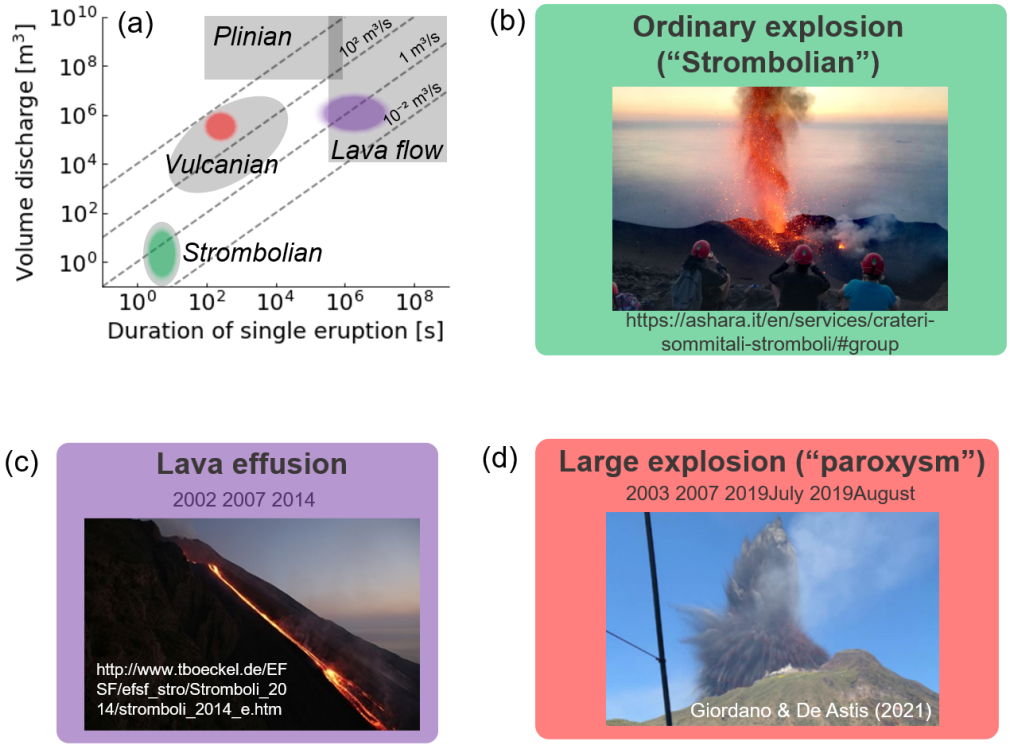

Figure 1.1: Variety of eruption types at Stromboli volcano illustrated with volume discharge and duration of the single eruption. (a) Plot of volume discharge and the duration of single eruption. Typical ranges for representative volcanic eruption types (Plinian, lava flow, Vulcanian and Strombolin) taken from Nakamichi and Aoyama (2016)[133] are marked by grey shaded areas. Colored ellipses indicate typical range for volcanic eruptions at Stromboli volcano: ordinary explosion (a: green, e.g. Ripepe et al., 1993[167]); lava effusion (c: purple, e.g. Valade et al., 2016[198]); paroxysm (d: red, e.g. Pistolesi et al., 2011[156]). (b), (c) and (d) represent pictures of ordinary explosion, lava effusion and paroxysm, respectively.

Literature	Eruption event	Deformation model (Analytical/Numerical)	N. of stations
Genco & Ripepe (2010)	>2,000 ordinary explosions in 2008	Infinite open conduit (Bonaccorso & Davis, 1999)	5 (5)
Bonaccorso+ (2008)	2007 lava effusion	Prolate (Yang, 1989)	5 (0)
Marchetti+ (2009)		Crack (Okada, 1992)	2 (2)
Mattia+ (2004)	2003 pre-paroxysm	Crack (Okada, 1992)	6 (3)
Bonaccorso+ (2012)	2007 syn-paroxysm	Sphere (Mogi, 1958)	2 (0)
Di Lieto+ (2021)	2019 July&August syn-paroxysm	Sphere (Mogi, 1958)	2 (0)
Viccaro+ (2021)	2019 July & August pre-paroxysm	Sphere (FEM)	5 (3)
Ripepe+ (2021a)		Finite open conduit (Bonaccorso & Davis, 1999)	5 (5)
Mattia+ (2021)		Sphere (Mogi, 1958)	6 (3)
This study	>800 Ordinary explosions in 2014	Sphere/ellipsoid (FEM)	5 (5)
	2014 lava effusion		5 (5)
	2019 July pre-paroxysm		6 (6)

Figure 1.2: Summary of the ground deformation studies of Stromboli volcano. The target event of analysis (green: ordinary explosion; purple: lava effusion; red: paroxysmal explosion), ground deformation model (black: analytical; red: numerical) and the number of stations are listed. For deformation model, column color represent modelling performed in corresponding study (white: inversion; grey: forward modelling). For number of stations, the number of stations close to the active crater (<1.2 km) are written in red in brackets

Chapter 2

Observation network and data

We analyze tilt data associated with the three different-type eruptions at Stromboli volcano (Figure 2.1). For the analysis of ordinary explosions, in addition to permanent tilt stations operated by LGS-UNIFI, we use data from three temporary tilt stations which were installed close to the summit craters from May to September 2014. This temporary observation aimed to examine the volcanic pressure source of ordinary explosions because it is necessary to use high-precision sensors near the eruptive vent to detect very tiny (10^{-9}–10^{-6} radian) short-lived (seconds to minutes) signals associated with ordinary explosions. Since the same station network was operative when a lava effusion occurred on 7 August 2014, we analyze tilt signals associated with this lava effusion. For the analysis of paroxysm, we focus on the 3 July 2019 paroxysm because the number of available stations is the largest (six stations) among the geophysically observed four events (i.e. 2003, 2007, July 2019 and August 2019), and this event has been intensely studied by other geophysical and geochemical approaches. The tilt data recorded by the permanent stations are used both period for the 2014 (ordinary explosio and lava effusion) and 2019 (paroxysm) (green mark in Figure 2.1b). Besides, for the analysis of the paroxysm, the tilt record is also derived from broadband seismometers. Figure 2.2 summarizes the stations we used in the following analyses.

2.1 Permanent borehole-type tilt stations

The Laboratorio di Geofisica Sperimentale (LGS) of the University of Florence has been operating an integrated geophysical network including seismometers, acoustic sensors, tiltmeters and thermal cameras at Stromboli volcano since January 2003 (Figure 2.1a; e.g.

Ripepe et al., 2004[164]; Ripepe et al. 2009[159]). Three permanent tiltmeters (LSC, OHO and LFS in Figure 2.1b) are located at an elevation of >500 m a.s.l. within ∼1 km distance from the summit craters (Genco and Ripepe, 2010) and are equipped with Pinnacle 5000T electrolytic borehole biaxial sensors installed at a depth of ∼5.5 m with a nominal resolution of 1 nrad (10^{-9} radian). Analogue tilt record is smoothed by an internal Sallen-Key type low-pass filter with a cutoff frequency of ∼0.033 Hz (period of ∼30 s) and digitalized with a sampling frequency of 1 Hz. Digital data is recorded on on-site flash memory, and then is radio-transmitted to the monitoring centre (Centro Operativo Avanzato; COA) of the Department of Civil Protection on the island. The data are collected, processed and displayed on the monitors of the COA and the website of LGS (http://lgs.geo.unifi.it/) in real time. The Y-axis of the tiltmeter is aligned toward the summit craters, which results in one radial (Y-axis) and one tangential (X-axis) tilt component. The exact orientation of the tiltmeter's axis is measured by an internal digital compass, and the tilt components are transformed into East-West (EW) and North-South (NS) axes by comparing the tilt to the seismic signal associated with teleseismic earthquakes (Marchetti et al., 2009[117]; Genco and Ripepe, 2010[76]).

2.2 Temporary platform-type tilt stations in 2014

The 2014 effusive eruption started on 7 August after ∼4 months of increased explosive activity (Valade et al., 2016[198]). From 19 May 2014 to 6 June 2015, three temporary tiltmeters (CPL, PZZ and RFR) were deployed (Figure 2.1b) within a close distance (<400 m) from the summit craters (Valade et al., 2016[198]; Kondo et al., 2019[103]). These stations were equipped with 701-2A platform biaxial bubble-type sensors (Jewell Inc.) installed at a depth of about 50 cm. Each instrument was connected to a data logger HKS-9550 (Keisokugiken Corp.) and digitized with a sampling frequency of 100 Hz and a resolution of 24-bit. The orientation of tiltmeter's Y-axis was set to the magnetic north by an analogue compass. The orientations and relative amplitudes of these tiltmeters were corrected by comparing P- or surface wave particle motions of several teleseismic earthquakes that occurred between June and July 2014. Tilt records of the permanent (LSC, OHO and LFS) and temporary stations (CPL, PZZ and RFR) are used to analyze ground tilt events from 1 June to 15 August in 2014. The tiltmeters at the temporary stations were embedded in a shallow (50 cm) hole. We do not use the NS component of

PZZ after 20 July 2014 because of saturation.

2.3 Permanent broad-band seismic stations in 2019

In 2019, five permanent broad-band seismic stations (SCI, ROC, STR, PZZ and SDK) were deployed around the summit craters. SDK is located on the slope of the Sciara del Fuoco. These stations were equipped with CMG-40T broad-band seismometers (Güralp Inc.) with a sensitivity of 800 V/(m/s) and a flat-response range of 60–0.01 s (SDK) or 30–0.01 s (the other four stations). Signals were digitized by a 24-bit Güralp CMG-24 converter with a sampling frequency of 100 Hz, and then were radio-transmitted to the monitoring centre, COA. Two paroxysmal explosions occurred on 3 July and 28 August 2019. Three of the five seismic stations were damaged by the first paroxysm. PZZ and SDK were destroyed by a volcanic blast immediately after the eruption onset, and SCI stopped a few minutes after the eruption onset due to the fire caused by the ejected materials. Although the first paroxysm seriously damaged our monitoring network, these five seismic stations and permanent borehole tilt station OHO provided clear ground deformation signals before the eruption (Ripepe et al., 2021a[163]).

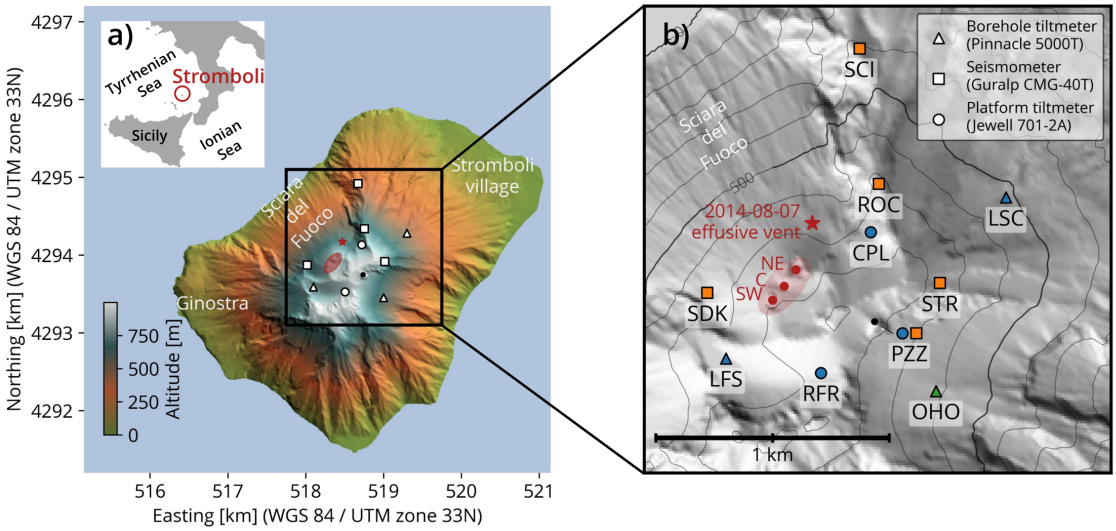

Figure 2.1: Topography map and tiltmeter network of Stromboli volcano. (a) Location and topography of Stromboli Island and tiltmeter network. (b) Zoom-up of the summit area showing the summit crater terrace (red-filled ellipse) and eruptive vents (red circle): the northeast (NE) vent, the central (C) vent and the southwest (SW) vent. The red star indicates the vent of the 7 August 2014 effusive eruption opened at 5 a.m. UTC. The location of the tilt stations is indicated by triangles (permanent tilt stations equipped with borehole tiltmeter Pinnacle 5000T), squares (permanent broad-band seismometer Güralp CMG-40T) and circles (temporary tilt stations equipped with platform tiltmeter 701-2A), which are used for 2014 (blue), the 3 July 2019 paroxysm (orange) and both events (green).

Station			East [km]	North [km]	Elevation [m]	Depth [m]
OHO	P	14 19	519.000	4,293.450	615	5.5
LFS	P	14	518.100	4,293.590	738	5.5
LSC	P	14	519.300	4,294.280	525	5.5
CPL	J	14	518.721	4,294.131	747	0.5
PZZ	J	14	518.736	4,293.748	854	0.5
	G	19				-
RFR	J	14	518.507	4,293.528	820	0.5
SCI	G	19	518.673	4,294.917	400	-
ROC	G	19	518.755	4,294.338	710	-
STR	G	19	519.017	4,293.913	795	-
SDK	G	19	518.021	4,293.871	640	-

Figure 2.2: Locations, instruments and operational periods of tilt and seismic stations. Locations are shown in the coordinate of WGS 84 UTM zone 33N. Operational periods are indicated by "14", 2014 and "19", 2019. Types of instruments are shown: P, Pinnacle 5000T; J, Jewell 701-2A; G, Güralp CMG-40T.

Chapter 3

Data analysis of ground tilt signals

3.1 Ordinary explosion

First, we show data analysis of ordinary explosions that occurred during the temporary observation from May to August 2014. Ground deformation associated with ordinary explosions was classified into four stages and selected by semi-automatic picking of the tilt signals associated with each explosion. In the following, we explain the method to extract the tilt signals of each explosion and examine the basic characteristics of the tilt vectors.

3.1.1 Data processing

Since tilt records at the temporary stations (CPL, PZZ and RFR) are sampled with 100 Hz, we decimate them to 1 Hz by averaging over 1 s to be consistent with the data of the permanent stations. Tilt records have several data missing. Such data gaps shorter than 10 s in the tilt record are interpolated by using a cubic spline function. We then apply a Butterworth-type low-pass filter with a cutoff frequency of 0.02 Hz to remove short-period signals (Figure 3.1). Ground tilt signals associated with ordinary explosions and effusive eruptions were recorded at most of the stations. However, due to their high sensitivity, the tiltmeters also record ground deformation associated with other environmental effects such as tides, rainfall and barometric pressure changes (e.g. Agnew, 1986[1]; Anderson et al., 2010[9]). Moreover, the tiltmeters installed in a shallow depth are affected by temperature changes that may be caused by thermoelastic strain in the subsurface, generating diurnal and seasonal tilt variation (Berger, 1975[26]; Harrison and Herbst, 1977[85]; Bonaccorso et al., 1999[38]). Tilt recorded by the platform tiltmeters (CPL, PZZ and RFR), buried at a depth of $\sim$50 cm, and a borehole tiltmeter LSC show a significant diurnal variation

of ∼5 μrad (Figure 3.1). Ground tilt associated with ordinary explosions is characterized by a duration of $\sim 10^2$ s and amplitude of $\sim 10^{-1}$ μrad (Genco and Ripepe, 2010[76]). To retrieve these events, we apply a Butterworth-type high-pass filter with a cutoff period of 6 h that removes long-period signals such as temperature-induced diurnal oscillations. We analyze the tilt records from 1 July to 14 July (filled with blue in Figure 3.1) which are continuously recorded at all six tilt stations. During this period, eruptive activity was characterized by more intense explosive activity than usual and nine short-lived lava overflows from the summit vents (Valade et al., 2016[198]).

3.1.2 Classification of tilt signals and event selection

Processed tilt signals based on the flow of Section 3.1.1 are shown in Figure 3.2. Tilt component EW or NS nearly directing to the summit at each station are shown. Positive amplitude indicates the uplift towards the summit craters, while negative represents the down-lift. The observed ground deformations are characterized by the uplift and down-lift signals similar to the deformation reported in Genco and Ripepe (2010)[76], representing ground inflation and deflation around the craters. These characteristics are common to five stations (CPL, PZZ, RFR, LFS and OHO in Figure 3.2). Only LSC does not show a clear tilt signal associated with the ordinary explosions, probably due to the larger distance (∼1 km) from the summit crater or for worse coupling with the ground. For this reason, LSC data are not used in the following analyses. Tilt amplitudes range from 50 to 300 nrad at the stations located at an elevation >600 m a.s.l. and a distance of <500 m from the summit craters.

We divide the inflation-deflation cycle into four stages: A) gradual inflation, B) rapid inflation, C) rapid deflation and D) recovery process. These four stages of the tilt cycle are defined by using the seismic VLP signal recorded in the NS component of RFR. To retrive the seismic VLP signal, we apply a different filter on the unfiltered tilt records. We use a band-pass filter with 20–100 s (plot in the bottom of Figure 3.3b), instead of the low-pass filter of 50 s (0.02 Hz). The VLP onset and end are defined by using an amplitude threshold of 25 nrad. This threshold was heuristically defined as a half amplitude of the root mean square of the seismic VLP signals recorded from 1 July to 14 July 2014. We assume that the onset and the end of VLP seismic signals coincide with the onset of the rapid inflation (stage B) and the end of the recovery process (stage D), respectively. The gradual inflation (stage A) is defined from the end of VLP to the onset of the following

VLP. The rapid inflation (stage B) is defined from the onset of VLP to the peak of the tilt signal, followed by the rapid deflation (stage C) from the peak to the bottom of the tilt signal. The recovery process (stage D) is defined from the bottom of the tilt signal to the end of VLP. Tilt particle motion of all the stations indicates the same back-azimuth for all four stages (Figure 3.3c), suggesting that the pressure source does not change the lateral position during the inflation-deflation cycle and remains stable. Note that tilt signals during rapid inflation (stage B), rapid deflation (stage C) and recovery process (stage D) may be contaminated by translational motions associated with the seismic VLP signals (e.g. Aoyama and Oshima, 2008[16]).

Sometimes, two explosions can occur at a time shorter than a full cycle, partially overlapping the gradual inflation (stage A). To exclude such consecutive events (less than 10%), we analyze tilt cycles that satisfy the criterion on three durations: (i) duration of VLP (from the VLP onset to the end of the following VLP in Figure 3.3b), $T_{VLP} < 200$ s; (ii) durations of rapid inflation of < 30 s; (iii) duration of rapid deflation of $<$50 s. To pick high signal-to-noise ratio events, we further impose thresholds for the duration of gradual inflation T_{GI} to be $T_{GI} > 50$ s, and the maximum amplitude of the seismic VLP signal, $A_{VLP} > 100$ nrad.

3.1.3 Characteristics of ground tilt of the selected events

Using the above criteria, we automatically pick 868 ground tilt events, and for each of them, we measure the amplitude and the back-azimuth of tilt vectors of the four stages. We find that the recovery process (stage D) is sometimes unclear and noisy by visual inspection. We then decide not to include stage D in the analyses.

Duration of the gradual inflation (T_{GI}) mainly distributes between 50 s and 300 s, with a median of 215 sec, whereas the duration of the rapid inflation (T_{RI}) and rapid deflation (T_{RD}) distributes around 10–25 s (median of 16 s) and 25–35 s (median of 30 s), respectively (Figure 3.4).

Amplitudes of stage A, gradual inflation, at RFR ($\sim$400 m from the C crater) generally distribute below $<$100 nrad, with a peak at around $\sim$60 nrad (Figure 3.5b), whereas rapid inflations (stage B) show amplitude ranging between 50 and 250 nrad with a median at $\sim$120 nrad, and rapid deflation (stage C) ranges between 100 to 500 nrad with a median of $\sim$300 nrad. As expected, the amplitude of the three stages at a distant station (e.g. CPL in Figure 3.5c) is smaller than RFR. Tilt amplitudes are almost constant during the

analyzed term. Only on 12 July, during frequent lava overflows (Valade et al., 2016[198]), we measure a slight increase in rapid inflation and deflation. However, it is not clear whether this amplitude variation reflects a change in the eruptive activity.

Tilt back-azimuth for the three stages generally points to the summit craters (Figure 3.6). Only CPL and LFS stations have a direction of ∼30 degrees (north side) and ∼45 degrees (south side) different from the summit craters, respectively. Overall, tilt directions of the five stations do not converge to a single point, suggesting that the observed tilt may be affected by volcano topography, non-isotropic source shape, finite-size source or heterogeneity of the volcano edifice. For pressure source estimation, we use the median amplitude and azimuth of the tilt signals for each station (green lines in Figure 3.6; Figure 3.7).

3.2 Lava effusion

Second, we show data analysis of the lava effusion that occurred on 7 August during the temporary observation. Ground deflation associated with lava effusion is retrieved from tilt records. We also examine the temporal variation of ordinary explosions before and after the lava effusion to suggest implications for the shallow magma system of Stromboli.

3.2.1 Characteristics of tilt signals

During our experiment, an effusive eruption occurred on 7 August at 05:00 UTC, at a lateral vent located at an elevation of ∼670 m a.s.l. along the Sciara del Fuoco, preceded by the period characterized by increasing eruptive activity and magma level for ∼3 months (Valade et al., 2016[198]). Ground deformation was recorded by the tiltmeters before and during the effusive eruption (red vertical bar in Figure 3.1). Only the CPL station, the closest (∼200 m) to the effusive vent, recorded, almost 15 h before the onset, inflation of ∼13 μrad linearly directed towards the effusive vent (Figure 3.8). This inflation was accompanied by a minor collapse of a portion of the NE crater and by a large rockfall along the Sciara del Fuoco, suggesting the lateral intrusion of a dyke from the main conduit towards the effusive vent (Valade et al., 2016[198]). The high linearity of tilt vector motion suggests that the pressure source of the inflation was stably localized near the effusive vent. After the eruption onset, all the stations recorded a similar exponential-like deflation lasting a couple of days with the tilt vector pointing to the same back-azimuth

direction of the summit craters. This ground deformation has been interpreted as caused by the discharge of $\sim 1.6 \times 10^6$ m^3 of lava flow from the central magma plumbing system beneath the summit crater area through the dyke that occurred in the first 48 hours (Valade et al., 2016[198]; Ripepe et al., 2017[165]).

Ground tilt motion at CPL clearly includes the additional contribution of the intruded dyke between the summit area and the effusive vent (Valade et al., 2016[198]). To remove this effect and extract the deflation of the main pressure source beneath the summit area, we use the difference of tilt amplitude from −15 h to +48 h instead of from the effusion onset (0 h) to +48 h for the observed tilt used for the pressure source estimation of the lava effusion (purple arrows in Figure 3.8c). This tilt vector of CPL (−15 h to +48 h) directs the summit crater area, whereas the tilt motion from 0 h to +48 h directs between the summit and the effusive vent.

3.2.2 Characteristics of ground deformation associated with ordinary explosion before and after lava effusion

Here, we examine the temporal variation of gradual inflation signals (stage A) of ordinary explosions for all stations. During the whole analysis period of 1 June to 15 August, we picked 4862 events by applying the same criteria used for the analysis of 1 to 14 July (868 events). After the onset of lava effusion, inflation-deflation tilt cycles and the VLP seismicity resumed, although the surface phenomena at the vent (e.g. magma ejection and acoustic signal) ceased due to the decrease of magma level in the conduit (Ripepe et al., 2015[161]; Valade et al., 2016[198]). This magma level change can be tracked by the depth (back-azimuth) of VLP particle motions (Ripepe et al., 2015[161]).

Figure 3.9 shows tilt amplitude variation of the gradual inflations. From 1 June to 7 August (lava effusion), tilt amplitudes are generally stable as they show small fluctuations in the 7-day average (orange line in Figure 3.9). After 7 August, RFR and OHO show a slight decrease in amplitude, although the amplitude of CPL remains the same level as those of before lava effusion. Figure 3.10 shows the variation of tilt amplitude ratio relative to RFR. As shown in Figure 3.9, amplitude ratio CPL/RFR increases after the 7 August lava effusion. Figure 3.11 shows tilt azimuth variation of the gradual inflations. Tilt azimuths show large variations up to a few tens of degrees in each explosion due to a low signal-to-noise ratio. After 7 August, CPL and OHO show slight change in azimuth of $<\sim 10^\circ$. Overall, there is no evidence of drastic change in the tilt vector, for example,

reversal of tilt direction or significant increase/decrease of amplitude, in the temporal variation of gradual inflations. These results suggest that the shallow volcanic structure acting as a pressure source for ordinary explosive activity remains almost stable regardless of lava effusion. However, it also implies that ground deformation associated with ordinary explosions can be used to infer slight variations of the shallow volcanic structure same as the VLP seismicity.

3.3 Paroxysm

We analyze a paroxysmal explosion that occurred at 14:45:43 UTC on 3 July 2019. Ground deformation is retrieved from the permanent borehole tiltmeter and broad-band seismometers. We also analyze ordinary activity from 1 July to 4 July to examine relationship between ordinary explosions and paroxysm.

3.3.1 Data processing

Tilt produced by the 3 July 2019 paroxysm was recorded by one borehole tiltmeter (OHO) and five broad-band seismometers (SCI, ROC, STR, PZZ and SKD) (see Section 2 and Ripepe et al., 2021a[163]). Since the broad-band seismometers have a frequency response down to 30 s or 60 s, tilt components are derived from seismic signals (Rodgers, 1968[170]; Battaglia et al., 2000[24]; Aoyama and Oshima, 2008[16]; Genco and Ripepe, 2010[76]; Lyons et al., 2012[114]). Recently, tilt motions are derived from the broad-band seismograms at many volcanoes worldwide (e.g. Sanderson et al., 2010[175]; Fontaine et al., 2014[69]; Vandemeulebrouck et al., 2014[199]; Aoyama and Oshima, 2015[17]; Maeda et al., 2017[115]; Honda et al., 2018[89]). At Stromboli, previous studies succeeded in retrieving the ground tilt associated with ordinary explosions (Wielandt and Forbriger, 1999[206]; Genco and Ripepe, 2010[76]) and paroxysmal explosions (Pino et al., 2011[153]; Viccaro et al., 2021[202]; Ripepe et al., 2021a[163]; Mattia et al., 2021[123]). Tilt signals are represented by a time integral of ground velocity seismogram $v(t^{'})$ multiplied by a transfer factor (Genco and Ripepe, 2010[76]):

$$\tau(t) = -\frac{\omega_0^2}{g}\int_0^t v(t^{'})dt^{'}, \tag{3.1}$$

where t is the time, $\tau(t)$ is the tilt, ω_0 is the natural angular frequency (equivalent to $2\pi/T_0$, where T_0 is the natural period), and g (9.8 m/s^2) is the gravitational acceleration. The contribution of the ground acceleration included in the formula is negligible below its

natural frequency ($0 < \omega < \omega_0$). Using the natural period T_0 of 60 s for SDK and 30 s for the other stations, we calculate the transfer factor $-\omega_0^2/g$ for each seismic station. We follow a procedure similar to Genco and Ripepe (2010)[76] to retrieve tilt signals (Figure 3.12): (i) decimate the ground velocity sampled at 100 Hz to 1 Hz by averaging over 1 s; (ii) remove the mean of the velocity signal; (iii) integrate the velocity signal into a displacement by trapezoidal integration; (iv) low-pass filter (Butterworth-type causal filter) below the natural frequency of 60 s to remove higher frequency signals; (v) multiply the filtered displacement signal by the transfer factor $-\omega_0^2/g$. In addition to procedure (iv), we apply a high-pass filter at 1 h to reduce the effect of the daily thermal noise with amplitude higher than the preceding inflation on the seismic-derived tilt records (e.g. Pino et al., 2011[153]). We apply the same filters to the borehole tiltmeter OHO (Figure 3.13)

3.3.2 Characteristics of tilt signals before the onset of the paroxysm

Ground inflation associated with the 3 July 2019 paroxysm shows a unique signal starting from ∼3–4 hours before (Figure 3.14). At 11:20 (−3.5 hours), the tilt signal in the borehole station OHO shows a small step-like inflation with ∼0.1 μrad (arrow 1). This signal is followed by slow inflation lasting for ∼2 hours. Relatively rapid inflation with ∼0.2 μrad at 13:40 (∼ −1 hour, arrow 2), which is followed by deflation starting from 13:46 (arrow 3) and lasting for ∼45 minutes (blue vertical lines in Figure 3.15ab). This episodic inflation-deflation signal was also recorded by dilatometers of INGV (Giudicepietro et al. (2020)[79]; Di Lieto et al. (2020)[60]). We define this signal from ∼ −3.5 h to ∼ −10 min as "preceding phase". Ground inflation re-emerges from ∼10 minutes before, at 14:35 (Ripepe et al., 2021a[163]; Viccaro et al., 2021[202]; Mattia et al., 2021[123]). We define this signal from −10 min to the onset of the paroxysm (0 s) as "final inflation". Even during these ground deformation signals related to the paroxysm are observed, inflation-deflation tilt cycles associated with ordinary explosions are clearly recorded like as regular state of volcanic activity (Figure 3.15). In this study, we mainly analyze the final inflation to be used for the pressure source estimation.

Final inflation: ∼10 minutes before the onset

To analyze the final inflation, in addition to the tilt retrieval procedure (iv), we apply a high-pass filter at 1 h to reduce the effect of the daily thermal noise with amplitude higher than the preceding inflation on the seismic-derived tilt records (e.g. Pino et al.,

2011[153]). Figure 3.15 shows the filtered tilt signals. Final inflation before the 3 July paroxysm starts ∼600 s (10 min) before the eruption onset (Ripepe et al., 2021a[163]) occurred at 14:45:43 UTC at all the stations (Figure 8cd), which was also indicated by strainmeters (Giudicepietro et al., 2020[79]; Di Lieto et al., 2020[60]). At 150 s before the explosive onset, ground inflation accelerated at all the stations. In this accelerated phase, the NS component of STR showed a box-shape tilt step. This signal probably coincides with an occurrence of a volcano-tectonic (VT) earthquake that occurred at 14:44 UTC at a depth of 0.77 km beneath the summit (Giudicepietro et al., 2021) or anomalous local effect. Meanwhile, the NS component of SDK, which is located on the slope of the Sciara del Fuoco, showed significant tilt change to the opposite direction from the initial phase (−600 to −200 s: red-filled in Figure 3.15) and the last two ordinary explosions (two down-black arrows in Figure 3.15). This oppositely directed signal is probably due to an effect of an additional local pressure source (e.g. opening of a shallow small crack very close to the station) induced by final magma ascent, the VT earthquake, or increasing instability of the station, which is located inside the steep slope of the Sciara del Fuoco. Same as for stage B during the ordinary explosions, this rapid acceleration of the ground inflation before the paroxysm could also be contaminated by translational motion. Errors of tilt signals calculated as a 2σ (standard deviation) of the filtered tilt records from 10:00 to 13:00 are shown to infer the signal-to-noise ratio of each station (Figure 3.15cd).

For the pressure source estimation, we use only the amplitude of tilt recorded between −600 and −200 s before the explosion onset (red vector in Figure 3.16ab). The tilt vector of the paroxysmal explosion generally directs to the summit crater area. Back-azimuth of tilt vectors both for the ordinary (stacked tilt of 868 events, green vector in Figure 3.16a) and paroxysmal explosion (final inflation) recorded at PZZ and OHO well match with each other with a difference of only ∼4 degrees. Also, the amplitude ratios of tilts observed at the two stations are almost the same, with a difference of less than 10%. These agreements of tilt back-azimuth and amplitude in two station at different location and elevation implies similarity of horizontal location and depth of the pressure source centroid. This strongly suggests a common and stable pressure source responsible for ground deformations during both ordinary and paroxysmal explosions. Thus, both ordinary and paroxysmal explosions are probably induced by the same portion of the volcanic system. Since the amplitude ratio between the tilt signals at different stations is constant over the time of inflation (Ripepe et al., 2021a[163]), the source of inflation is assumed to be stable in the same

location, and the amplitude of the tilt calculated in the −600 to −200 s time interval can be used to determine the parameters of the pressure source associated with the paroxysm. Indeed, tilt vectors of the full inflation calculated from −600 s to 0 s is comparable to that of −600 s to −200 s except for SDK (Figure 3.16b), which supports the temporal stability of the pressure source. Ripepe et al. (2021a)[163] excluded SDK from pressure source estimation to utilize the full inflation from −600 s to 0 s. This study uses only the initial part to include SDK, the station only located at west of the summit craters, which provides a better constraint on the source inversions.

Preceding deformation: from ∼3.5 h before the onset

Ground deformation before the 3 July paroxysmal explosion is characterized by the preceding phase starting ∼3.5 hours before the onset and episodic inflation-deflation at ∼1 hour before as recorded by the permanent borehole tiltmeter OHO (Figure 3.14). These signals are also visible in the seismic-derived tilt stations (Figure 3.17). Since the seismic-derived tilt records significant diurnal variations as mentioned in Figure 3.12, we apply a high-pass filter with a cut-off period of 6 hours to reduce such effect. Figure 3.17 shows the high-pass filtered signals that are linear-detrended with 11:30-13:00 for visibility. The episodic inflation-deflation signal at ∼1 hour before (light blue line in Figure 3.17) can be recognized in most of the stations excepting tilt components with low signal-to-noise ratio, for example, SCI, ROC and the NS component of STR. In all the stations, the tilt motion of this signal directs to the summit area, as the polarity of the signal is consistent with that of the final inflation. This indicates that the preceding deformation signal is generated by neither a local phenomenon occurring at a neighbour of OHO nor outside of the station network but a pressure source beneath the summit area. Moreover, the tiltmeter of OHO has recorded the same characteristic signal in the last three paroxysms (15 March 2007, 3 July 2019 and 28 August 2019, Figure 3.18). This reproductivity demonstrates the robustness of the preceding signal before paroxysms and its importance for understanding the dynamics of magma ascent responsible for triggering paroxysms. Besides, although the signal-to-noise ratio of this signal is comparable to that of ordinary explosions (i.e. amplitude of ∼0.1 μrad) and thus not as high as the final inflation, it may be useful for forecasting paroxysms through an early-warning (EW) system based on ground deformation (Ripepe et al., 2021a[163]).

3.3.3 Activity of ordinary explosions before the paroxysm

Here, we examine ordinary explosions that occurred from 1 to 3 July. The 3 July 2019 paroxysm happened in the normal volcanic activity of ordinary explosions with medium activity level without any obvious precursors such as lava effusion which induces depressurization of the volcanic system and may trigger rapid ascent of magma ejected during paroxysms from deeper part (Calvari et al., 2011[42]; Ripepe et al., 2017[165]), or increase of geophysical monitoring parameters (e.g. tremor amplitude, number of ordinary explosions and intensity of acoustic emission). Since the ordinary activity was suddenly interrupted by the paroxysm on 3 July 2019, it is important to investigate the similarity and differences between them to understand the triggering mechanism of paroxysms. Ripepe et al. (2021a)[163] showed the scale-invariance between pre-explosive inflations of ordinary and paroxysms, suggesting common conduit dynamics among different-type explosive eruptions. However, tilt signals (Figure 3.14, 3.15) indicate that even during the final inflation before the onset of the paroxysm (−600 s to 0 s), ordinary explosions repeatedly occurred every 5–10 min as usual. This means that paroxysms are driven by a physical process independent of ordinary explosions, whereas two common stations in our analyses (PZZ and OHO) share similar tilt vectors (Figure 3.16a).

The tilt amplitude of two tilt stations at different elevations can be used for a simple estimation of the relative depth change of pressure source (e.g. Takeo et al., 2013[190]). We thus examine the amplitude ratio of tilt associated with ordinary explosions using OHO (at 615 m a.s.l.) and PZZ (at 854 m a.s.l.). The other seismic station (SCI, ROC, STR and SDK) indicate not enough signal-to-noise ratio to measure the tiny ($\sim< 0.5\mu$rad) inflation-deflation signals associated with ordinary explosions. We manually selected 11 events from 1 July to the onset of the paroxysm on 3 July and calculated the amplitude ratio (OHO/PZZ) for gradual inflation (stage A) and rapid inflation (stage B) (Figure 3.19). The tilt amplitude ratio of gradual inflation is 0.15±0.13. Similar to our data analysis in 2014 (Section 3.2), it shows a large variation due to a low signal-to-noise ratio. On the other hand, that of rapid inflation is calculated to be 0.22±0.05. This tilt amplitude ratio for the paroxysm is 0.21 for −600 s to −200 s and 0.26 for −600 s to 0 s (Figure 3.16), and are within the range of amplitude ratio of gradual inflation. This suggests that the pressure source of the paroxysm and the ordinary explosions before the paroxysm is basically the same. This agrees with the similarity of two tilt vectors (Figure 3.16a) and supports the similarity and temporal stability of the pressure source.

3.4 Summary

We have analyzed tilt signals associated with ordinary explosion, lava effusion and paroxysmal explosion at Stromboli volcano. Observed tilt vectors of three eruption types used for the pressure source estimation are summarized in Figure 3.20. The ground tilt cycles of ordinary explosions can be classified into four stages: (A) gradual inflation, (B) rapid inflation, (C) rapid deflation and (D) recovery process. The observed tilt vectors calculated by stacking 868 events that occurred from 1 to 14 July 2014 show tilt amplitude ranging from 8.6 to 56.6 nrad and generally direct towards the summit craters, while several stations show misorientation up to ∼30 degrees. Ground deformation associated with the 7 August lava effusion is characterized by local ground inflation with tilt amplitude of ∼13 μrad induced by dyke intrusion ∼15 h before the effusion onset and exponential decay of ground deflation lasting for >2 days that is well correlated in all stations. A difference of tilt signal between −15 h and +48 h is used for representative tilt vector for pressure source estimation, whose amplitude ranges from 6.6 to 26.8 μrad. Data analysis using tilt signal retrieved from seismogram also confirms unique and robust ground deformation starting ∼3.5 hours before paroxysms recorded by borehole tiltmeter OHO. These tilts generally direct to the summit crater area and share a similar deformation field to the ordinary explosion.

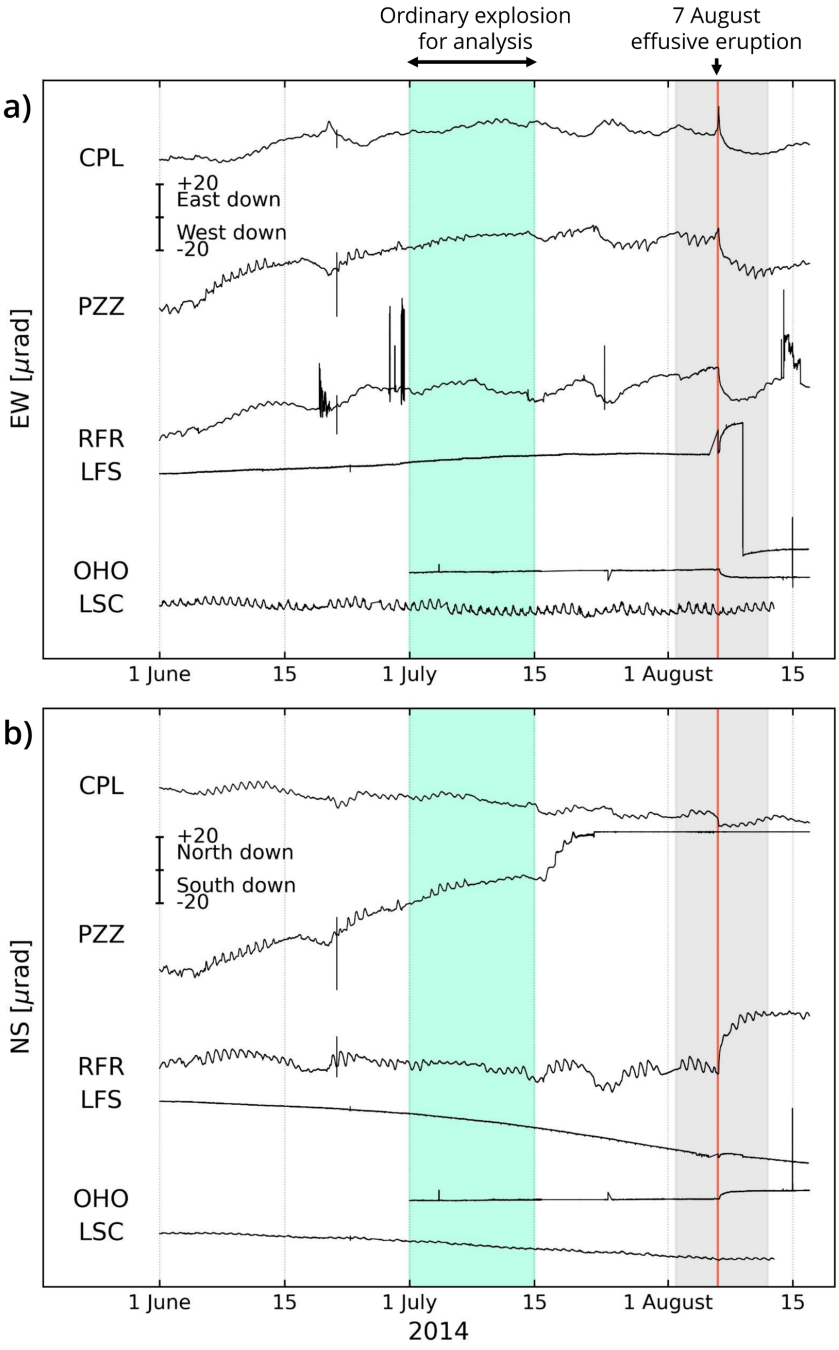

Figure 3.1: Ground tilt records from 1 June to 18 August 2014 (a: EW components, b: NS components). Positive tilt change indicates a down-lift of the east or north direction. The red vertical bar indicates the onset of the 7 August effusive eruption. The period used for the analysis of ordinary explosions is highlighted in blue.

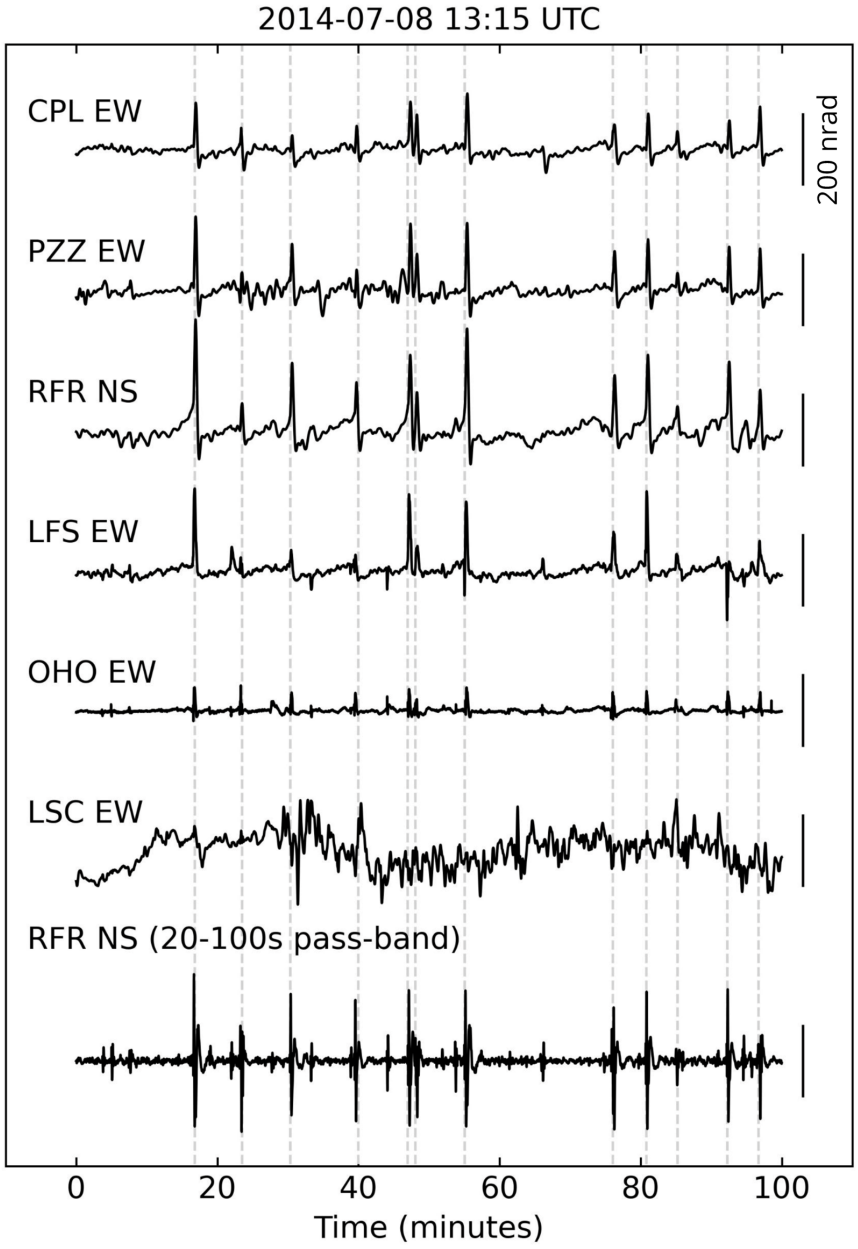

Figure 3.2: An example of ground tilt signals at six stations. Horizontal components (NS or EW) almost directing to the summit craters are shown at each station. The polarities of the signals at RFR and LFS are reversed to show an uplift toward the summit craters in positive values. Dashed grey lines indicate the occurrence times of small explosions. Very-Long-Period (VLP) signals extracted by applying a band-pass filter of 20–100 s on the north component of RFR are shown at the lowest.

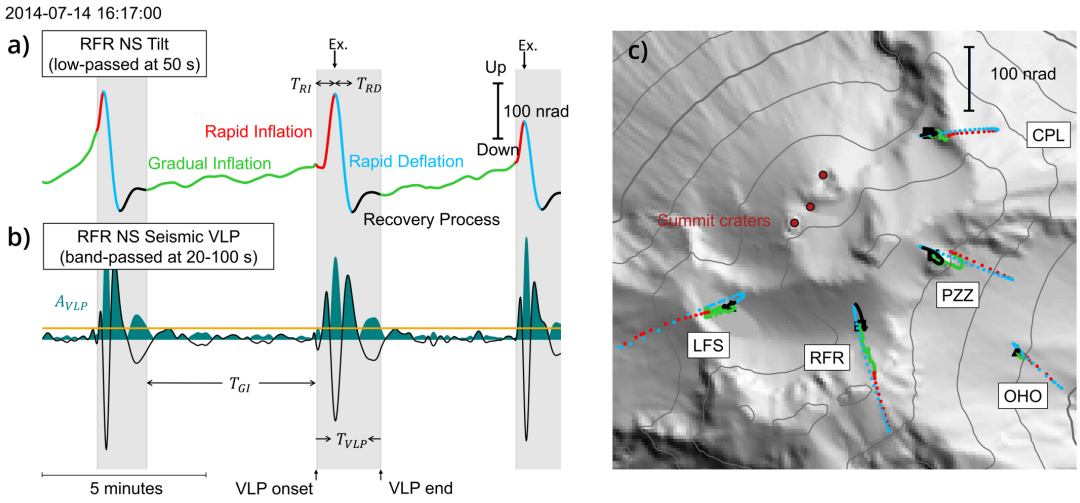

Figure 3.3: Classification of the inflation-deflation tilt cycle into four stages: gradual inflation, rapid inflation, rapid deflation and recovery process. (a) Tilt signal of the NS component of RFR (low-passed at 50 s, black line). Ex. indicates the occurrence time of each ordinary explosion. (b) Seismic VLP signal of the NS component of RFR (band-passed at 20–100 s, black line). The green shade indicates the absolute amplitude of the seismic VLP signal. The VLP onset and VLP end indicate the onset and end time of a VLP signal determined by imposing the threshold of the absolute amplitude on the seismic VLP signal. (c) Example of tilt motion of a single tilt cycle. The direction of the tilt vector indicates the direction of the down-lift.

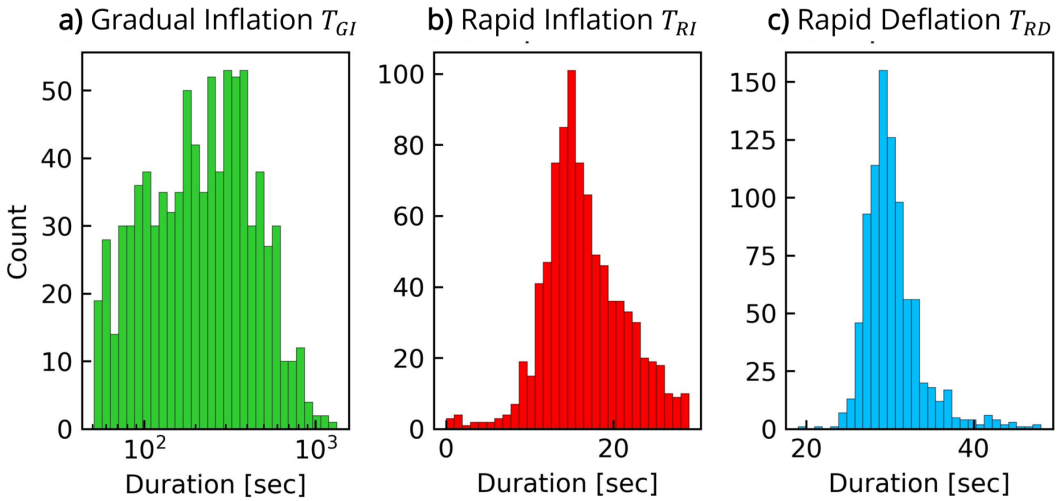

Figure 3.4: Histograms of the duration of the ground tilt for the three stages. Note that tilt events with rapid inflation of greater than 30 s and the rapid deflation of 50 s are not used to avoid the false selection of consecutive events. The horizontal axis of (A) is plotted on the log scale.

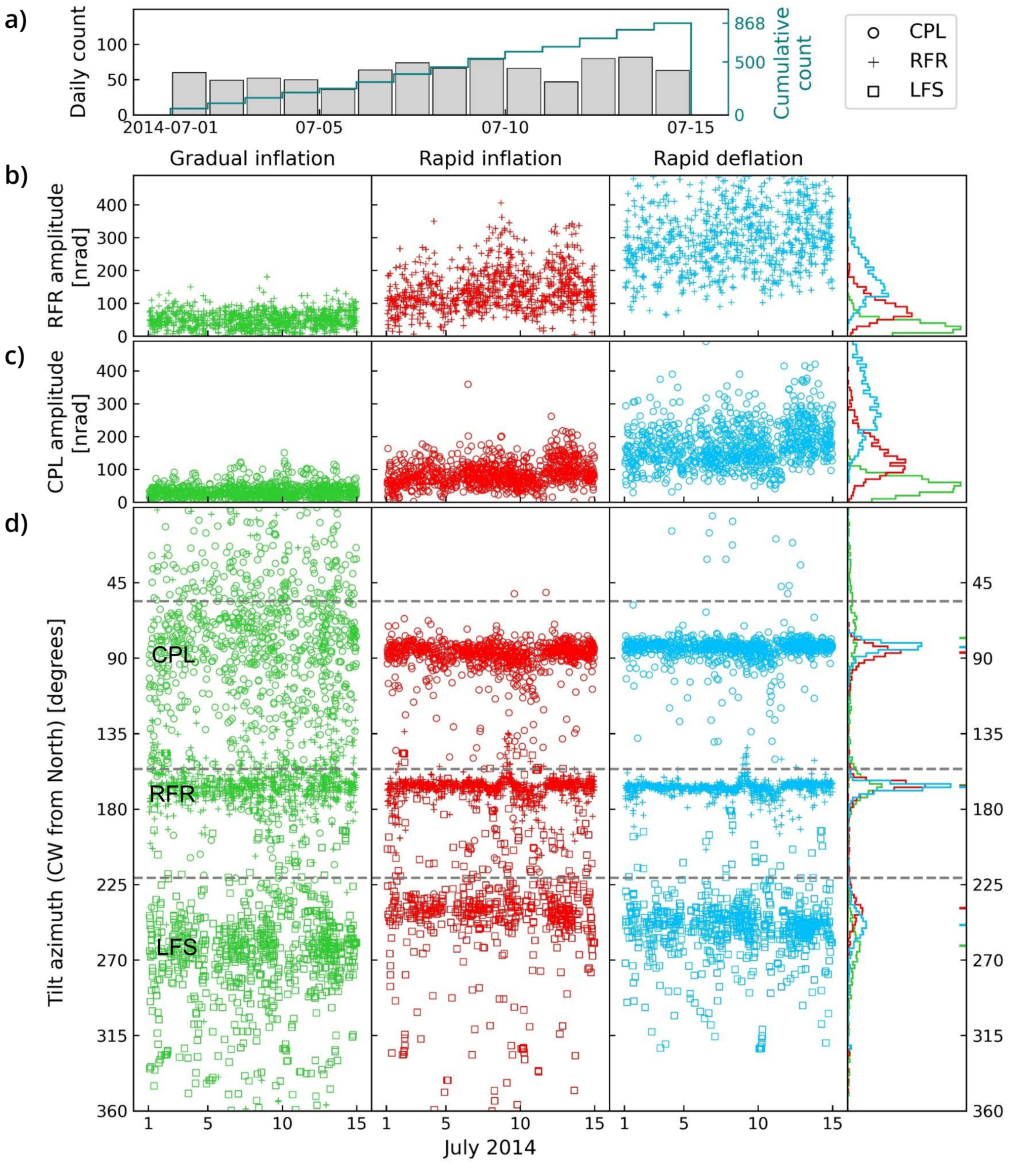

Figure 3.5: Temporal evolution of the parameters of the extracted tilt event for the three stages. a) daily and the cumulative number of events. b) Tilt amplitude of RFR. c) Tilt amplitude of CPL. d) Tilt azimuth of CPL, RFR and LFS. Dashed grey lines indicate the directions from each station to the C crater. The tilt azimuth of rapid deflation is reversed to compare with the gradual and rapid inflation easily. The right panels show histograms of the parameters.

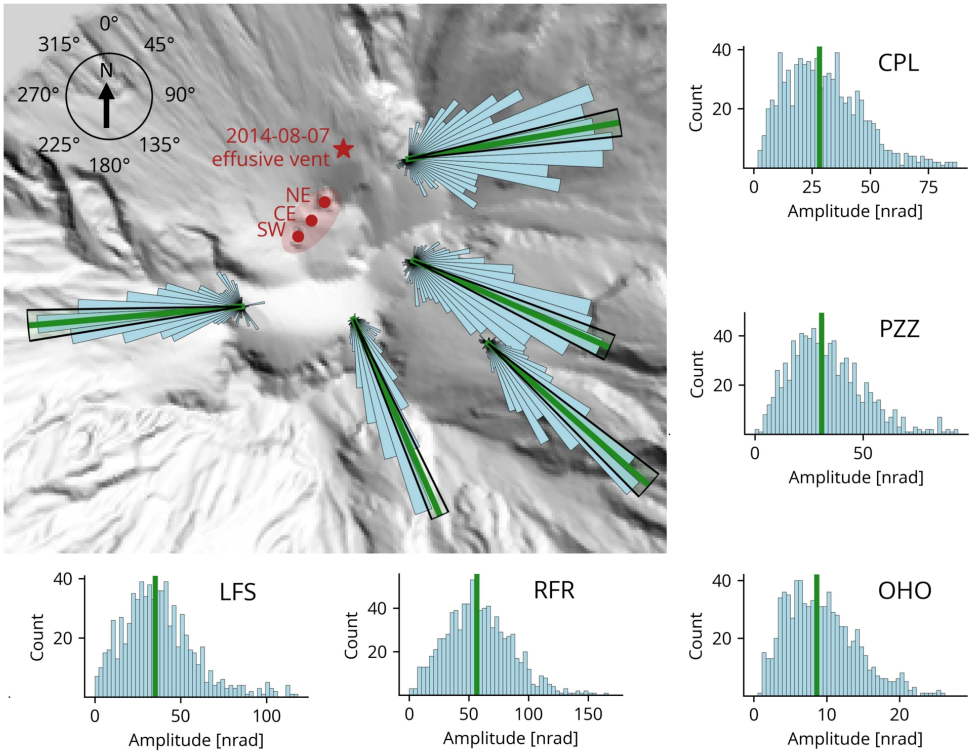

Figure 3.6: Azimuths and amplitudes of gradual inflations from 1 to 15 July. Rose plot of tilt azimuths of gradual inflations calculated from 860 events of ordinary explosions. The bar step is 5 degrees, and each histogram is normalized by its modal value. Panels around the rose plot indicate amplitude distributions for each station. The green bar shows the median value used for a representative tilt vector. For the rose plot, the 95% confidence interval (2 × standard error) is drawn by black circular sectors.

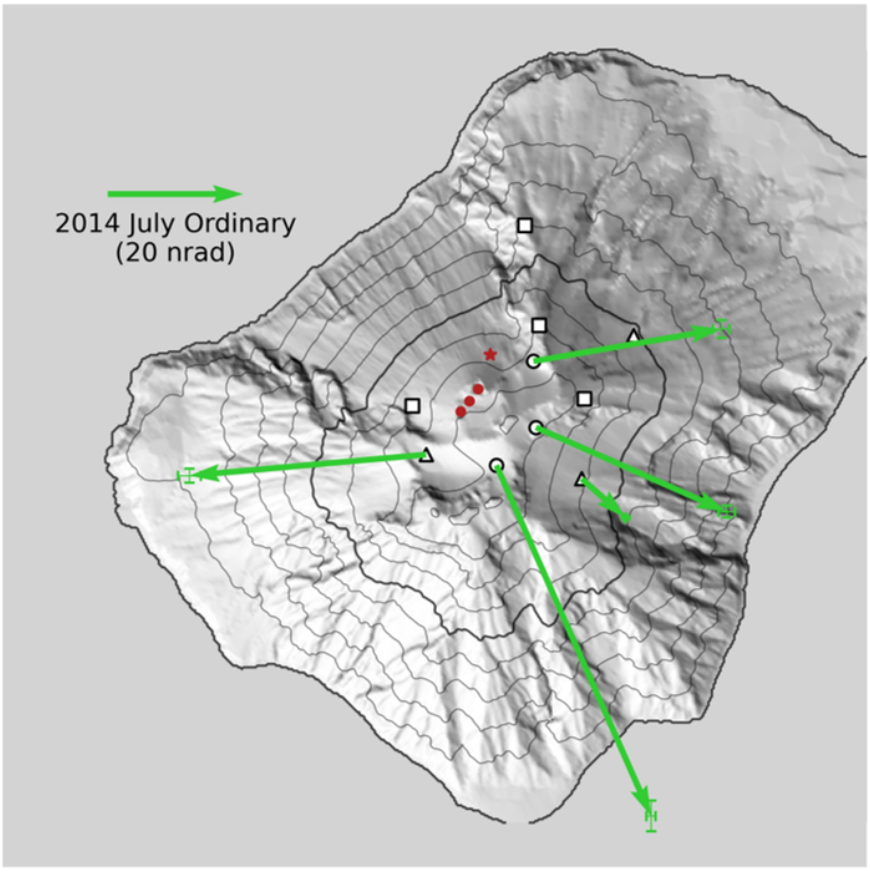

Figure 3.7: Representative tilt vector for the ordinary explosions (green). Summit craters (NE, C and SW) and the effusive vent are indicated by red circles. (2 × standard error) is drawn by green errorbars.

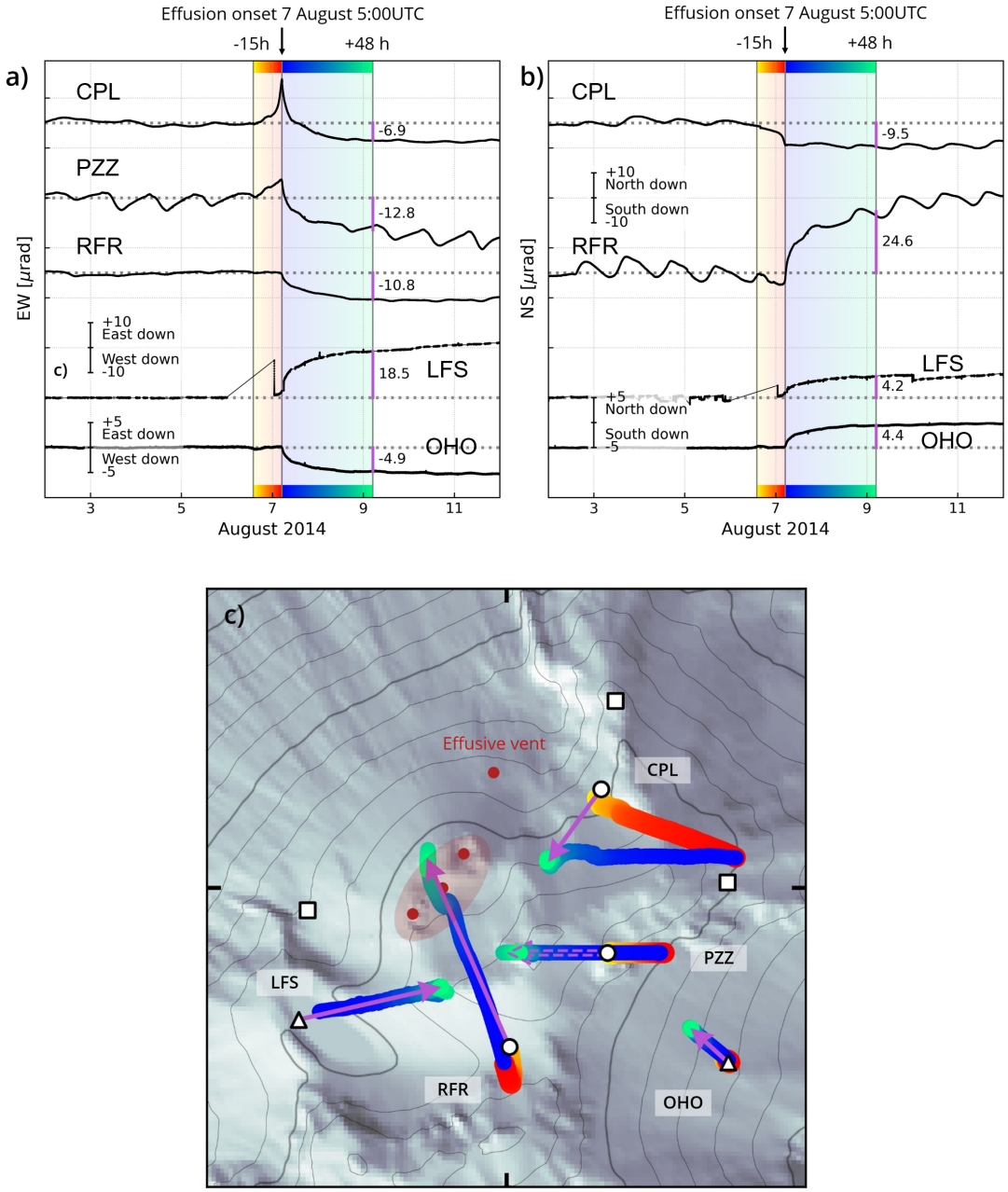

Figure 3.8: Ground tilt associated with the 7 August 2014 effusive eruption. (a), (b) Tilt records from 4 August to 11 August 2014. (a) the EW components, and (b) the NS components. The preceding phase to the effusion onset (−15 h to 0 h) is filled with the gradient from yellow to red, and the effusive phase is filled with the gradient from blue to green. (c) Tilt vector of the 7 August 2014 effusive eruption (purple). The eruptive craters are marked by red circles. Tilt vector motions during the preceding phase (−15 h to 0 h; yellow to red) and effusive phase (0 h to +48 h; blue to green). The new effusive vent at ∼670 m a.s.l. in the Sciara del Fuoco and the summit craters are marked by red circles.

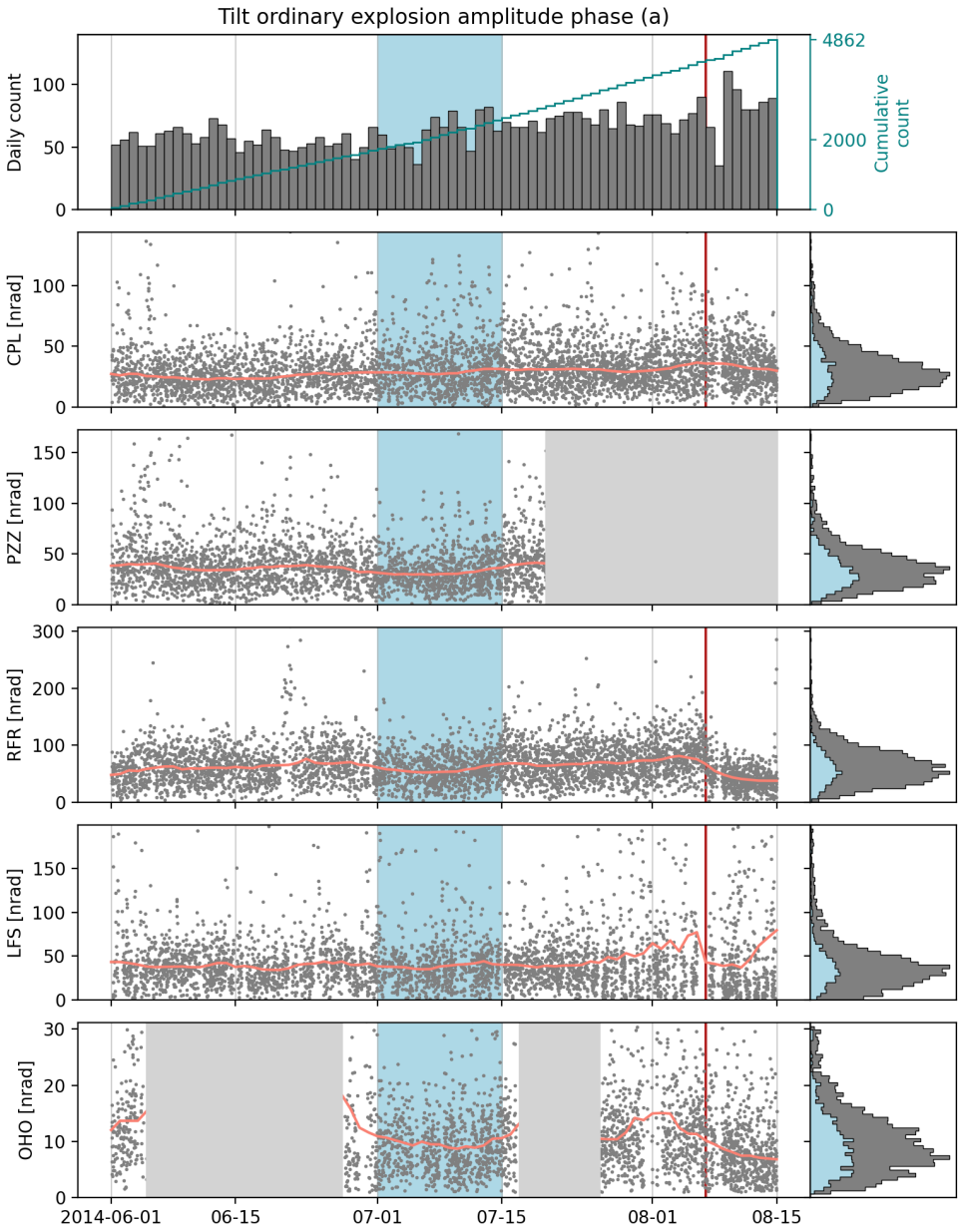

Figure 3.9: Temporal evolution of tilt amplitudes of the selected tilt event for gradual inflation (stage A) for the whole period with the daily and the cumulative number of the events. 7 days-moving averages are plotted as orange lines. The vertical red line indicates the 7 August lava effusion. The right panels show histograms of the parameters (grey: whole period, light blue: 1–14 July).

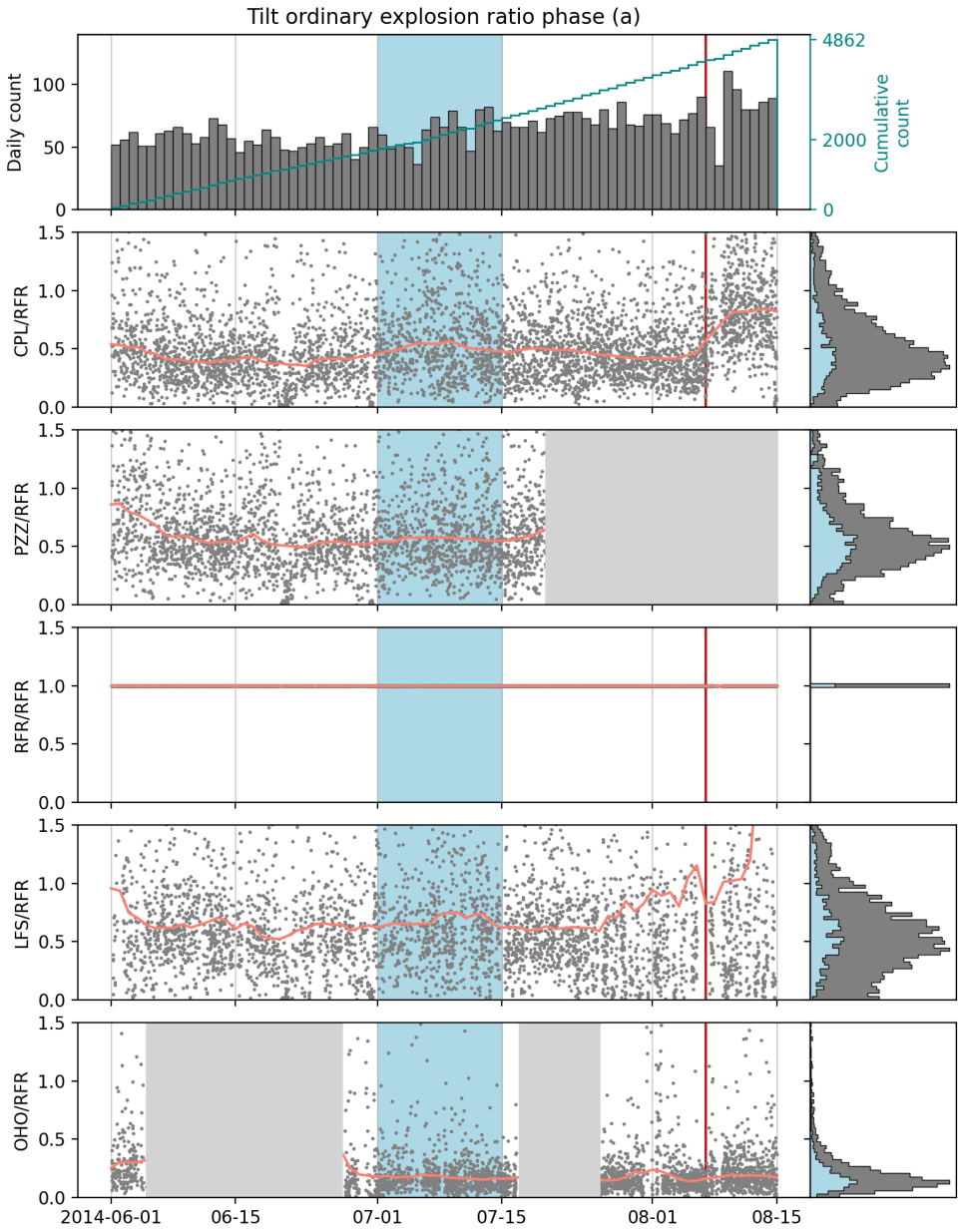

Figure 3.10: Temporal evolution of tilt amplitude ratios to RFR of the selected tilt event for gradual inflation (stage A) for the whole period with the daily and the cumulative number of the events. 7 days-moving averages are plotted as orange lines. The vertical red line indicates the 7 August lava effusion. The right panels show histograms of the parameters (grey: whole period, light blue: 1–14 July).

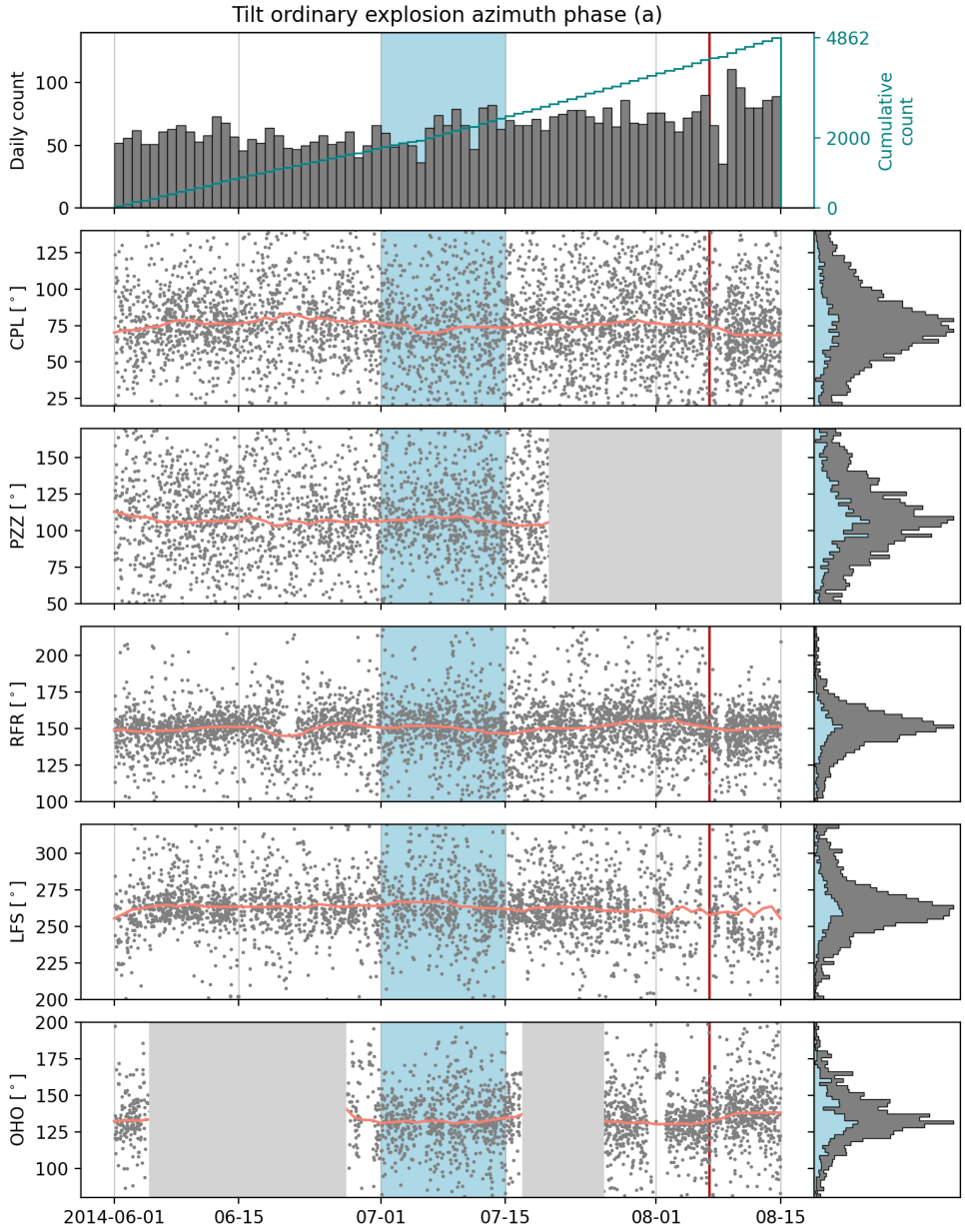

Figure 3.11: Temporal evolution of tilt azimuths of the selected tilt event for gradual inflation (stage A) for the whole period with the daily and the cumulative number of the events. 7 days-moving averages are plotted as orange lines. The vertical red line indicates the 7 August lava effusion. The right panels show histograms of the parameters (grey: whole period, light blue: 1–14 July).

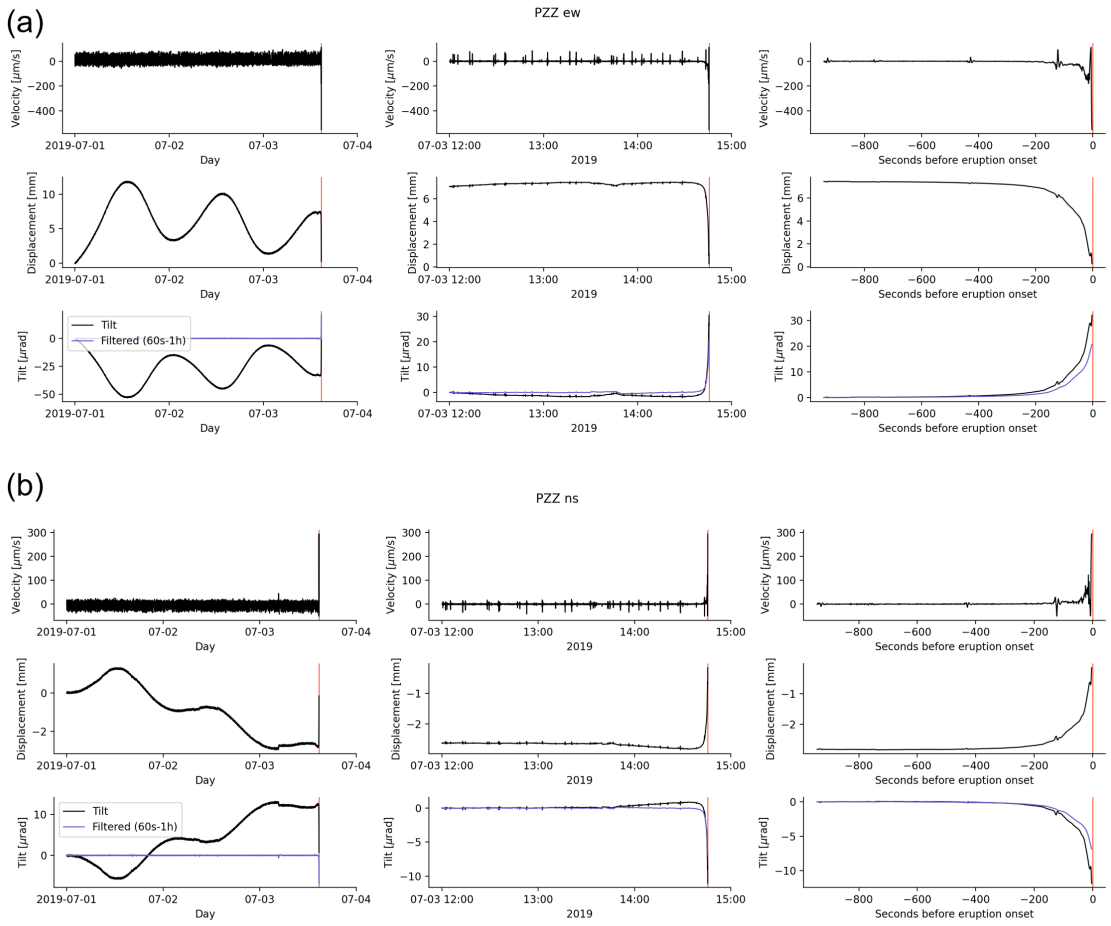

Figure 3.12: Data processing for retrieving tilt signals from seismic signals. The black and purple lines indicate tilt and filtered ones. (a) the EW component and (b) the NS component of station PZZ. The onset of the 3 July paroxysm (14:45:43 UTC) is indicated by a red vertical line. Upper, middle and bottom panales indicate velocity, displacement and tilt signals, respectively. Filtered tilt signals are drawn by purple lines. Signals are shown for three different time windows (Left: 1 to 4 July, 3 days; center: 12:00 to 15:00 UTC, 3 hours; right: −1000 to 0 s).

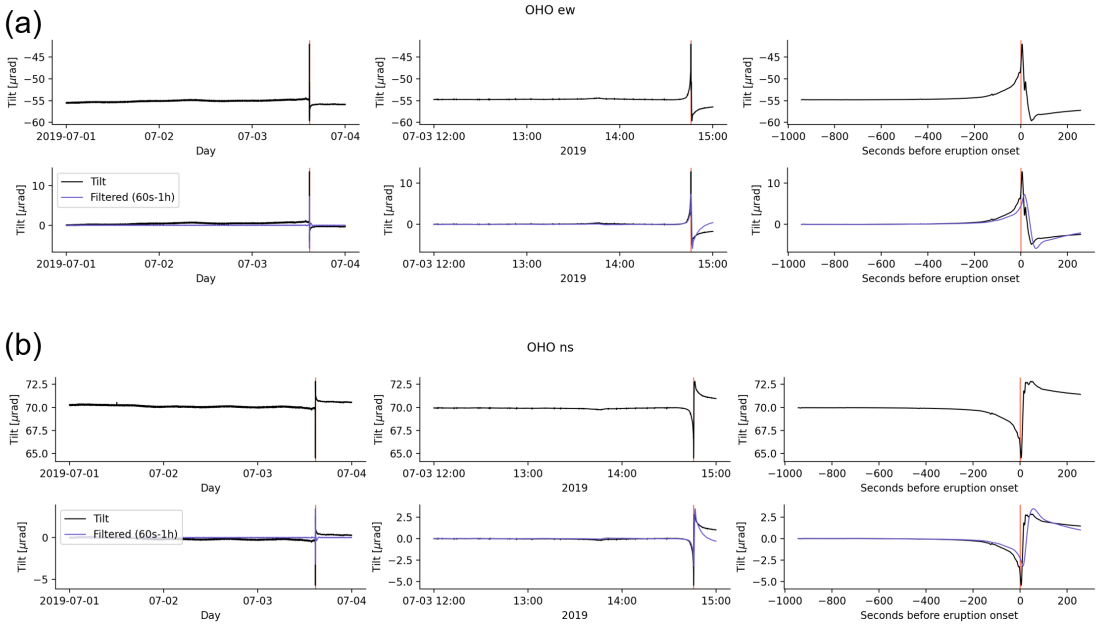

Figure 3.13: Data processing for borehole tilt station. The black and purple lines indicate tilt and filtered ones. (a) the EW component and (b) the NS component of station PZZ. The onset of the 3 July paroxysm (14:45:43 UTC) is indicated by a red vertical line. Upper and bottom panales indicate raw and filtered tilt signals, respectively. Signals are shown for three different time windows (Left: 1 to 4 July, 3 days; center: 12:00 to 15:00 UTC, 3 hours; right: −1000 to 0 s).

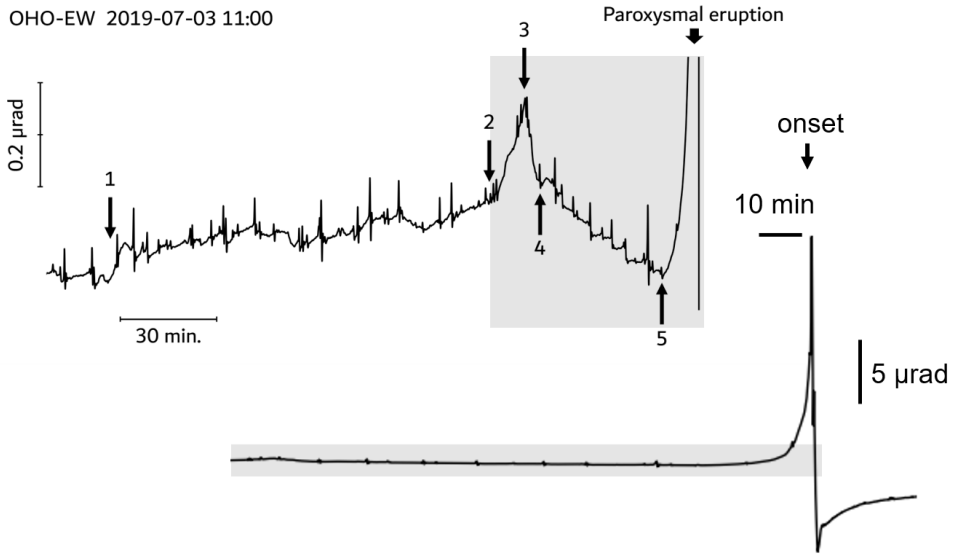

Figure 3.14: Tilt signals of the EW component of borehole station OHO associated with the 3 July 2019 paroxysm. The shaded grey area indicates the same time window (from 75 min to 0 min before the onset of the paroxysm) in each panel.

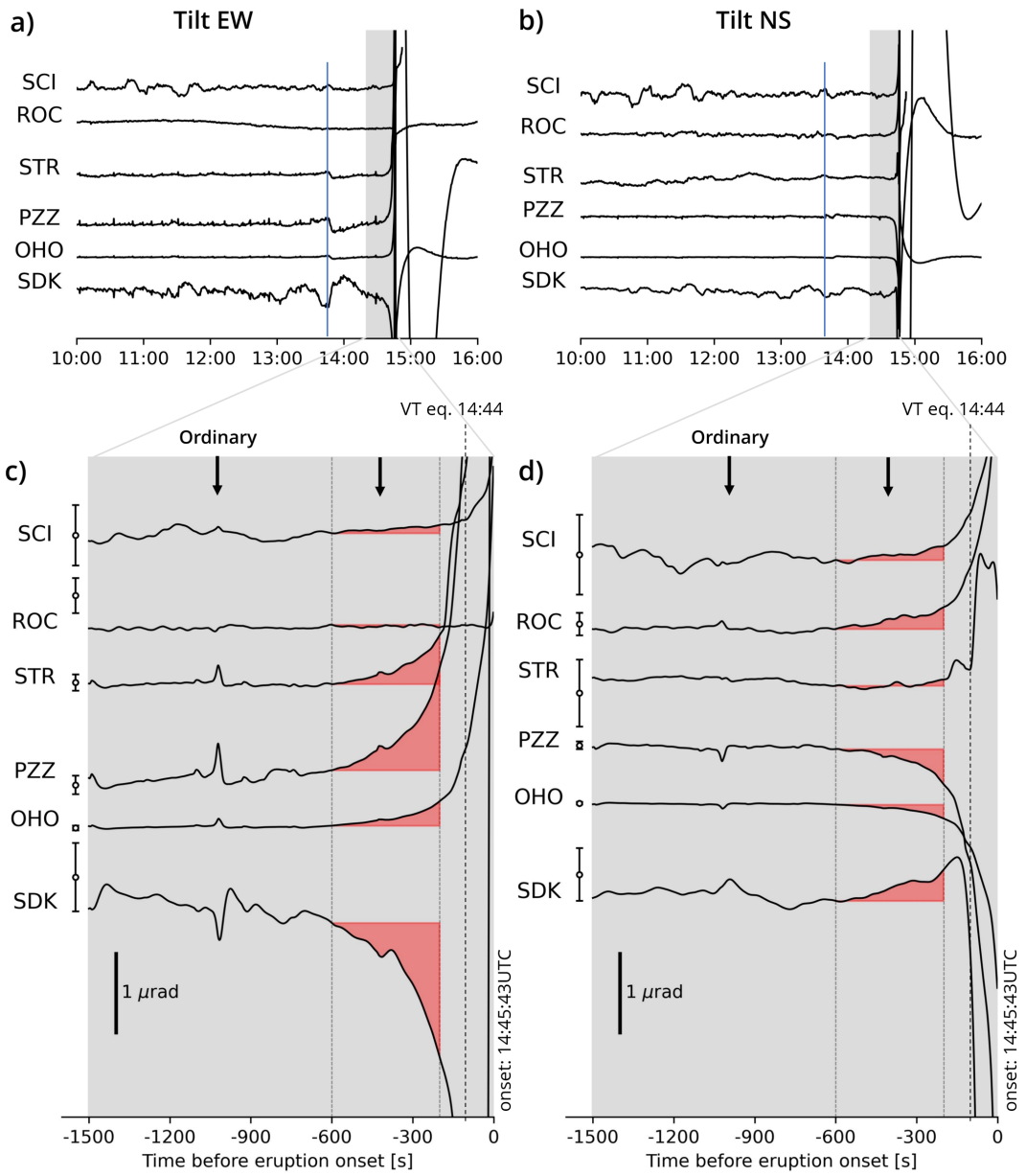

Figure 3.15: Tilt signals associated with the 3 July paroxysmal explosion. (a), (b) Tilt records of the EW (a) and NS (b) components from 10:00 to 16:00, 3 July 2019. The vertical blue bar indicates a small inflation-deflation tilt preceding ∼60 min to the eruption onset 14:45:43 UTC. (c), (d) Tilt records during −1500 s to the onset (0 s). Baseline and noise level calculated from 10:00 to 13:00 is shown by a circle with an error bar on the left side of each panel. The observed tilt vectors are calculated from the tilt amplitude of −600 s to −200 s (red-filled areas). Ordinary explosions occurred even during the pre-paroxysmal inflation (black arrows).

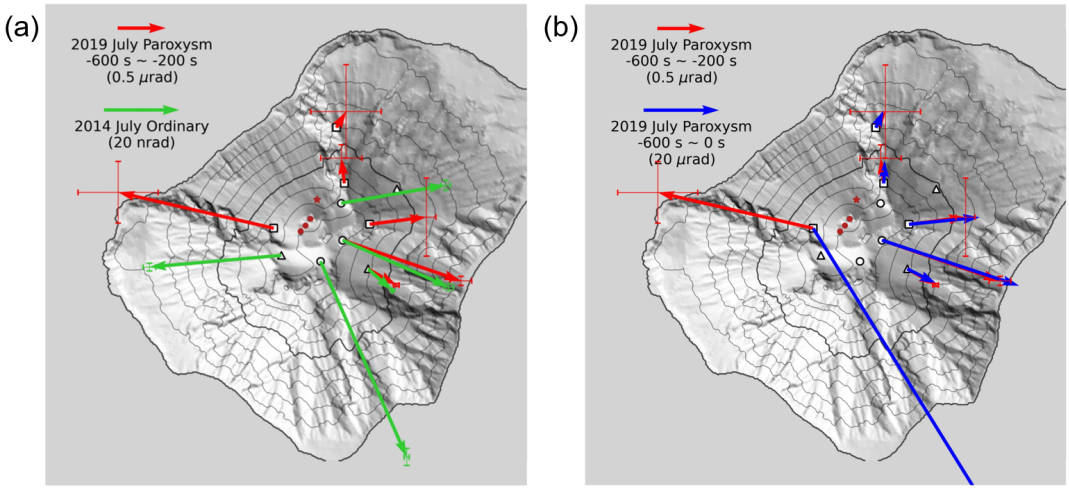

Figure 3.16: Observed tilt vector for the 3 July 2019 paroxysm. Red arrows indicate the observed tilt vector (−600 to −200 s). Measurement error (2×standard deviation; red error bar) is calculated from tilt motion high-passed at 1 h from 10:00 to 13:00. (a) Comparison with the observed tilt vector (green arrow) and measurement error (2×standard error green error bar) calculated from stacking 868 events. (Figure 3.7). (b) Comparison with a tilt vector calculated from -600 to 0 s.

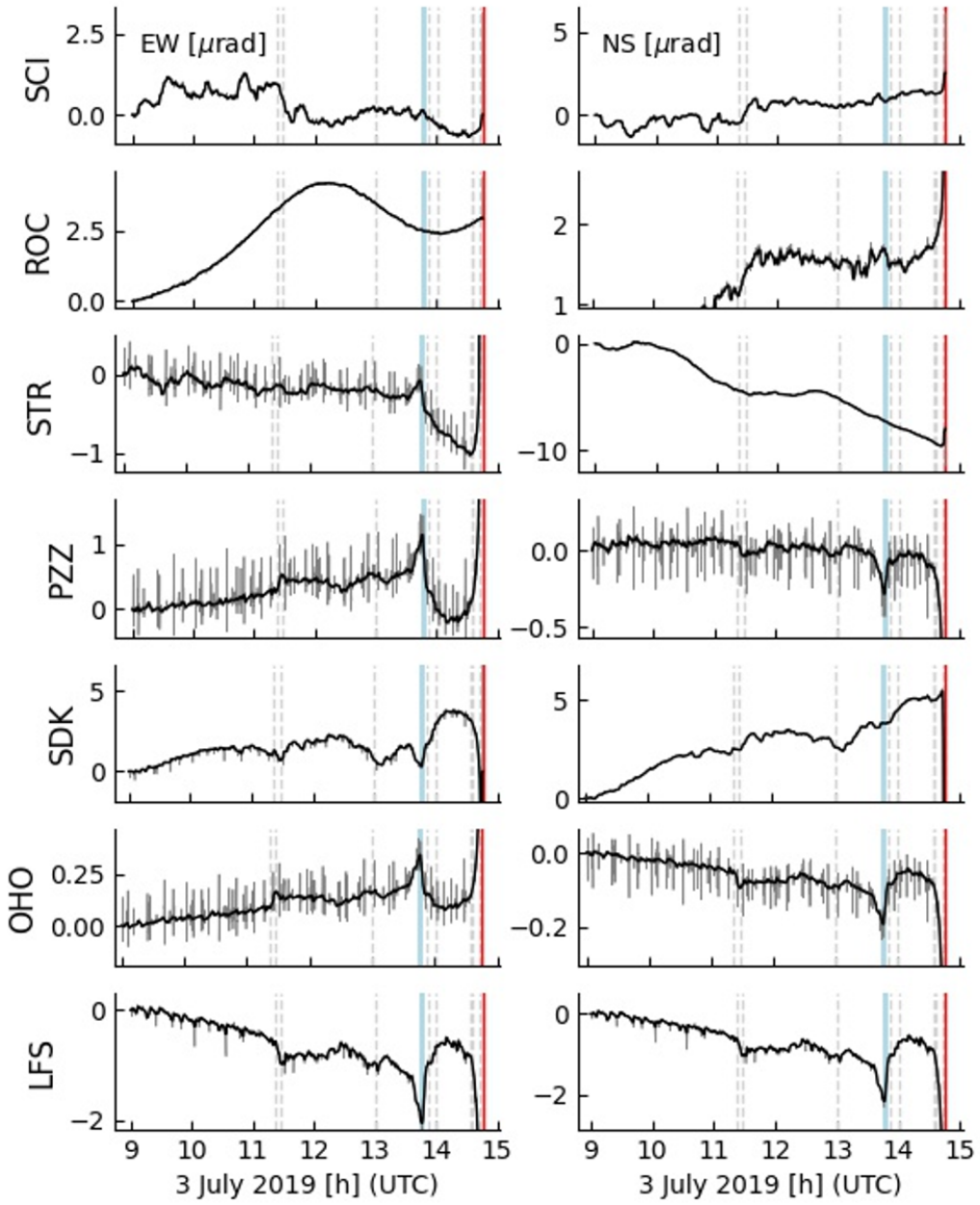

Figure 3.17: Tilt signals of the preceding phase recorded in borehole tiltmeters (OHO and LFS) or retrieved from seismometers. Grey and black lines indicate raw tilt and smoothed tilt (120 seconds moving median), respectively. Vertical red and blue lines indicate the paroxysm onset and the peak of the preceding phase, respectively.

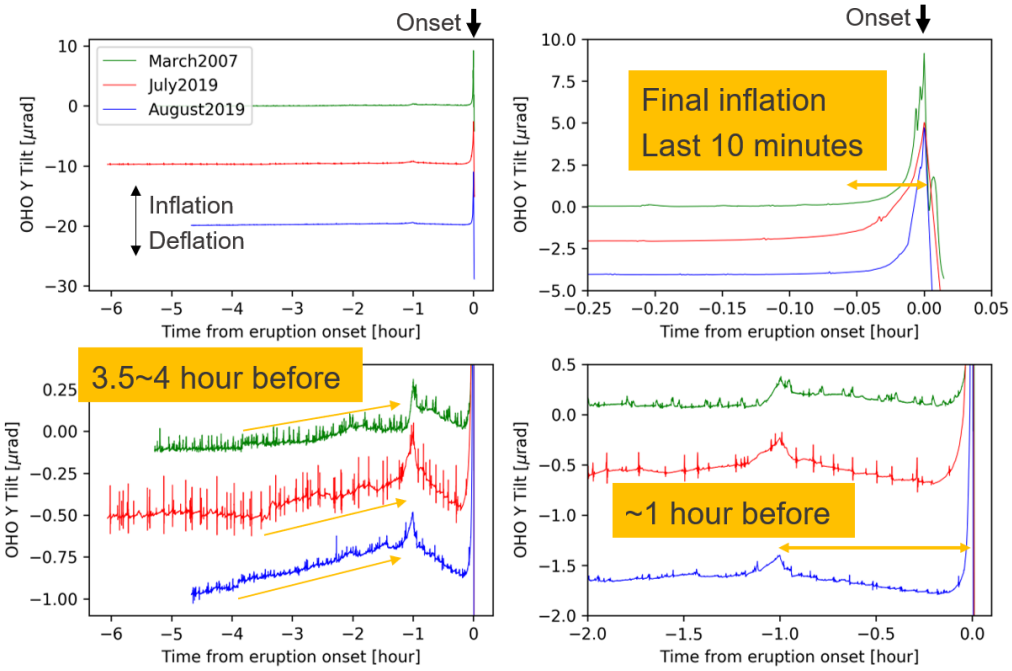

Figure 3.18: Tilt signals before the last three paroxysms (March 2007: green, July 2019: red; August 2019: blue) recorded in the radial component of borehole tiltmeter OHO. Four subplots are shown in different timescales and amplitude ranges.

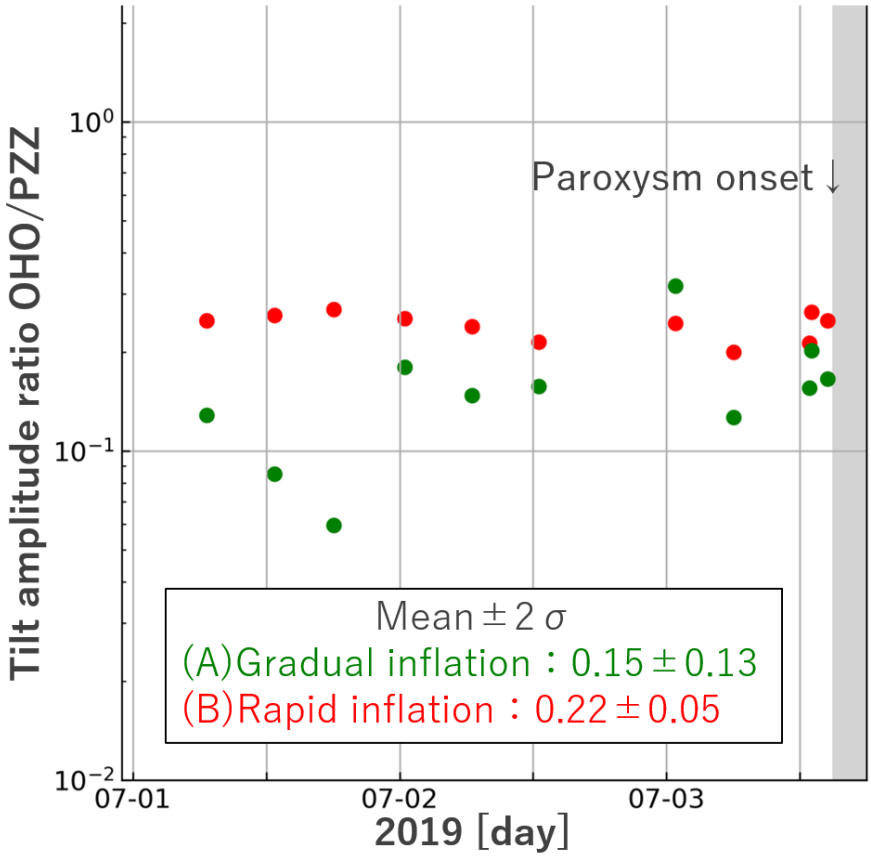

Figure 3.19: Tilt amplitude ratio of OHO/PZZ calculated for the hand-picked 11 ordinary explosions that occurred from 1 July to the onset of the paroxysm. Green and red scatters indicate the tilt amplitude ratio for gradual inflation (stage A) and rapid inflation (stage B), respectively.

2014		CPL	PZZ	RFR	LFS	OHO	
Ordinary explosion	Tilt EW [nrad]	27.732	28.154	22.817	−34.960	6.478	
	Tilt NS [nrad]	4.780	−12.466	−51.856	−3.113	−5.719	
	Amplitude [nrad]	28.141	30.790	56.654	35.098	8.641	
	Azimuth [degrees]	80.2	113.9	156.3	264.9	131.4	
7 August Effusion	Tilt EW [urad]	−6.864	−12.823	−10.755	18.537	−4.853	
	Tilt NS [urad]	−9.470	No data	24.601	4.232	4.438	
	Amplitude [µrad]	11.696	-	26.849	19.014	6.576	
	Azimuth [degrees]	35.9	-	156.4	257.2	132.4	
2019		SCI	ROC	STR	PZZ	SDK	OHO
3 July Paroxysm	Tilt EW [µrad]	0.099	−0.032	0.589	1.228	−1.617	0.294
	Tilt NS [µrad]	0.168	0.263	0.074	-0.423	0.374	−0.168
	Amplitude [µrad]	0.195	0.265	0.594	1.299	1.660	0.339
	Azimuth [degrees]	30.5	353.1	82.8	109.0	283.0	119.7

Figure 3.20: Measured tilt amplitudes for the ordinary explosion, lava effusion and paroxysm used for the inversions. Tilt amplitude and azimuth are converted from EW and NS tilt. Tilt azimuth is shown as clockwise from north in degrees.

Chapter 4

Estimation of volcanic pressure source

In this chapter, We invert the observed tilt vectors associated with the ordinary explosions, the 3 July 2019 paroxysm and the 7 August 2014 lava effusion to determine the location and shape of the pressure source. We calculate the ground deformation caused by an ellipsoidal pressure source using a finite element method (FEM), including the effect of the surface topography. To reduce the computational costs of numerical calculations, we perform grid-search-based inversions in several steps. First, we invert the best-fit location (centroid) assuming a spherical source model independently for the three data sets (ordinary explosion, paroxysm and lava effusion). Since the independent inversions return similar results for both ordinary explosion and paroxysm, we then combine the two datasets to estimate a common source from an inversion using an ellipsoidal source model. We show this best-fit model can also reproduce the ground deflation associated with lava effusion.

4.1 Method

4.1.1 Forward modelling of ground tilt

We calculate the ground deformation generated by a pressure source cavity buried in an elastically homogeneous material (Figure 4.1). Numerical computations are performed in the commercial FEM software COMSOL Multiphysics 5.3a (https://www.comsol.com) using a 3-D modelling domain in the structural mechanics module (e.g. Hickey and Gotts-

mann, 2014[87]). The topographic surface is represented by a digital elevation model (DEM) with a resolution of 10 m. We do not include any bathymetric data and consider the topography as a flat surface below sea level. This simplification generates negligible effects on the ground tilt because our tilt network is installed far above the sea level at the lowest elevation >400 m a.s.l. The model geometry is constructed as a hemisphere larger than the size of the island (radius of ∼2 km) with a radius of 10 km and a fixed boundary to prevent boundary effects (Figure 4.1a). Finer mesh resolution (up to 10 m) is applied around the source and the free surface within 1 km of the Central crater to cover all the tilt stations. The homogeneous elastic medium is generated with a Poisson's ratio ν of 0.25 and a rigidity μ of 1.3 GPa (Genco and Ripepe, 2010[76]).

The pressure source is represented by a triaxial ellipsoidal cavity with the centroid located in the cartesian coordinate X, Y, Z and the length of semiaxes a, b, c. A spherical source model is realized by setting $a = b = c$. The general orientation trend of volcanic structures such as volcanic dykes, focal mechanisms and faults exposed to the surface at Stromboli volcano is ∼50 degrees counter-clockwise from the east to the north (E50°N), which is primarily controlled by regional tectonic stress field (Bonaccorso, 1998[32]; Tibaldi et al., 2001[194]; Finizola et al., 2002[68]; Chouet et al., 2003[51]; Mattia et al., 2004[124]; Cesca et al., 2007[49]). We thus assume that the direction of the X-axis is fixed at E50°N and neglect the rotations of the ellipsoid (Figure 4.1b). We define this rotated coordinate as (SX, SY, SZ), whose origin point is set at 0 m a.s.l. beneath the Central (C) crater (Figure 4.1b). The pressure change of the source is applied as a boundary load on the wall of the ellipsoidal cavity. In this case, ground tilt τ generated by a pressure change of an ellipsoidal cavity at a position (SX, SY, SZ) with semiaxes (a, b, c) is expressed as

$$\tau = \frac{\Delta P}{\mu} G(SX, SY, SZ, a, b, c; \nu), \tag{4.1}$$

where ΔP is the pressure change, μ is the rigidity and $G(SX, SY, SZ, a, b, c; \nu)$ is the Green's function derived from the numerical calculation as a function of the Poisson's ratio ν (assumed constant at 0.25) and six free parameters SX, SY, SZ, a, b and c. A typical FE model generates $\sim 2.5 \times 10^4$ tetrahedral elements and solves one forward model in ∼140 s with our personal computational environment.

We conduct a benchmark test to evaluate the accuracy of a numerical solution by comparing it with an analytical solution. Figure 4.2 shows radial tilt generated by a pressurized spherical source calculated by the analytical formula (Mogi, 1958[132]) and the numerical model assuming a flat surface. As shown in Figure 4.2b, the deviation

of numerically calculated tilt relative to that of analytical tilt is less than ∼1%. Since our tilt stations are located at a distance of >∼200 m from the eruptive vent, although it is limited to a flat surface, we can assume that the numerical model can sufficiently reproduce ground tilt with an accuracy of ∼99.8% (deviation of ∼0.2%).

4.1.2 Grid-search-based inversion

Pressure source parameters are constrained by grid-search analyses. The misfit between models and observations is defined by measuring the misfit function (ratio of the sum of square observations to the residual sum of squares expressed as a percentage):

$$J = \sqrt{\frac{\Sigma_{i=1}^{N}(\tau_i^{obs} - \tau_i^{calc})^2}{\Sigma_{i=1}^{N}(\tau_i^{calc})^2}} \times 100[\%], \tag{4.2}$$

where N is the number of the observed tilt (generally equivalent to the two components times the number of stations), τ_i^{obs} is the observed tilt at ith data, and τ_i^{calc} is the calculated tilt.

4.2 Result

4.2.1 Independent inversions with a spherical source

We determine the position (SX, SY, SZ) of the source centroid for three datasets of ordinary explosion, lava effusion and paroxysm (step 1 in Figure 4.3; Figure 3.20) independently. We fix the radius of a sphere to be 100 m, considering the morphological feature of the summit crater terrace with about 150×75 m (Harris and Ripepe, 2007) and the gravity-driven magma drainage model proposed by Ripepe et al. (2015)[161]. Ground tilt is calculated for 539 centroid locations in the 300×300 m large area centred −200 m to +100 m in the SX direction and −200 m to +100 m in the SY direction around the summit crater terrace, and an elevation SZ from 200 m to 700 m a.s.l. with a step size of 50 m.

The best-fit centroid for the ordinary explosion is determined at $SX = -50$, $SY = -100$, and $SZ = 500$ m with a misfit J of 31.3% (Figure 4.4ab) from analysis of data of five stations (CPL, PZZ, RFR, LFS, OHO; green vectors in Figure 4.4b). The best-fit model (black vectors) well explains the observed tilt vectors (red vectors) at OHO and RFR. The model can reproduce the tilt amplitudes at CPL, PZZ and LFS, whereas the tilt azimuth differs 20-30 degrees from the observation. The pressure change associated with

ordinary explosions is 4.6 kPa, which is in good agreement with the pressure calculated from the static displacement of the VLP seismic signal (Ripepe et al., 2021b[160]). To evaluate the constraints on model parameters, here we refer to a range of the top 5% of the forward models with the smallest misfit. The good station coverage along NE-SW direction well constrains the SX location, as the top 5% of the smallest misfit (26 models, <40.1%) distribute in 3 grids (−100 m to 0 m). However, due to a weak coverage on the northwest side of the Sciara del Fuoco, the ranges of the top 5% models are −150 m to 0 m (4 grids) and 400 m to 650 m (6 grids) for SY and SZ, respectively, and there is a trade-off between SY and SZ.

The best-fit source for the July 2019 paroxysm is located at $SX = -50$, $SY = -100$, and $SZ = 550$ m with a misfit J of 27.2% (Figure 4.4cd) from the data of six stations (SCI, ROC, STR, PZZ, SDK, OHO; red vectors in Figure 4.4d), which differs of only one grid (+50 m in the SZ direction) from the location of the ordinary explosion recorded in 2014. Residuals for the paroxysm are very similar to that of the ordinary explosion, although the residuals are larger in the southwest and the deeper regions of the investigated volume, probably due to the weak geometrical coverage of the stations in this direction. Except STR and ROC, which show very small amplitude, the observed tilt vectors are well explained by the best-fit model. The pressure change is estimated to be 0.134 MPa. This is much smaller than the pressure calculated from the maximum amplitude of tilt (5.9 MPa; Ripepe et al., 2021[163]). This is because the pressure change 0.134 MPa is calculated from analysis of the initial part (−600 to −200 s) of the inflation.

We perform a similar grid-searching with a spherical source to estimate a depressurized source for the effusive eruption. We use the tilt at five stations (CPL, PZZ, RFR, LFS, OHO; Table 3.20 “7 August Effusion”; purple vectors in Figure 4.5) in the time interval from −15 h to +48 h around the eruption onset recorded. Ground tilt is calculated for 693 centroid locations in the 300×400 m large area centered −200 m to +100 m in the SX direction and −300 m to +100 m in the SY direction around the summit crater terrace, and an elevation SZ from 200 m to 700 m a.s.l. with a step size of 50 m. The best-fit centroid for the effusive eruption is estimated to be at $SX = -100$, $SY = -200$, and $SZ = 450$ m with a misfit J of 17.1%. Note that the north component of PZZ is excluded from the inversion because of the saturation. The best-fit model (black vectors) well reproduces the observed tilt. The pressure change is −2.7 MPa. The misfit distribution shows a pattern similar to the inversion results of ordinary and paroxysmal explosions.

The best-fit centroid is located about 100–200 m south of the summit. This difference is probably due to the difference in tilt direction of CPL, despite the lack of the north component of PZZ. CPL shows ∼30 degrees difference in back-azimuth of the observed tilt vectors between ordinary (green) and effusion (purple), while the other stations apart from the effusive vent show agreement. Because CPL is the only station that records large inflation before the effusive onset, this difference is most probably affected by the local contribution of the lateral dyke around the new vent.

4.2.2 Joint inversions

The results of independent inversion show that the ground deformations associated with ordinary explosion and paroxysm are generated mainly by the same shallow pressure source. This is consistent with the scale-invariance of the different explosive eruptions (Ripepe et al., 2021a) and indicates a volcanic structure or magma dynamics which in the final part of the feeding conduit remains stable for a long time. To improve the solution of the source location, we increase the coverage of the tilt station network by combining the tilt of the ordinary explosions with the tilt of the paroxysms (step 2 in Figure 4.3). The combined tilt vectors are jointly inverted by calculating an objective function J^{joint}, which equally balances the best-fit of the two inversions:

$$J^{joint} = \frac{J^{ordinary} + J^{paroxysm}}{2}, \tag{4.3}$$

where $J^{ordinary}$ and $J^{paroxysm}$ are the misfit for the ordinary explosions and the July 2019 paroxysm solutions defined by eq. (4.2). In this formulation, difference of tilt amplitudes in ordinary explosions and paroxysm is normalized by the sum of observed tilt (denominator of eq. 4.2) Source parameters are optimized by minimizing eq. (4.3), and pressure change is linearly obtained for each event.

The best-fit spherical source of the joint inversion is estimated to be located at $SX = -50$, $SY = -100$ and $SZ = 500$ m with J^{joint} =29.7% (Figure 4.4ef), using all the eleven observed tilt vectors at nine stations (Figure 3.20). As expected, the location remains almost at the same position as the centroid previously estimated. Similarly, also the pressure changes of 4.6 kPa for ordinary explosion and 0.15 MPa for the July 2019 paroxysm are not different from previous results. Only the resolution of the residual maps is sensibly improved owing to the complementarity of the two statoin networks.

Using the position of the centroid of the spherical source calculated by the joint in-

version, we search for the best axial parameters (a, b, c) within ± 1 grid (50 m) in each direction (3×3×3=27 locations) which fit an ellipsoid pressure source (step 3 in Figure 4.3; Figure 4.6). Axial parameters are set free to change between 50 and 200 m with a step of 50 m. The inversion shows that the ellipsoidal source also remains located at $SX = -50$, $SY = -100$, and $SZ = 500$ m, and has semiaxes of $a = 100$, $b = 150$, and $c = 100$ m, which is almost compatible with a spherical ellipsoid (Figure 4.6a). Pressure at the source is slightly reduced to 2.6 kPa for ordinary explosions and 0.089 MPa for the July 2019 paroxysm. The misfit of the joint solution J^{joint} is 27.6%, whereas the independent misfits are $J^{ordinary} = 30.3\%$ for the ordinary and $J^{paroxysm} = 24.5\%$ for the paroxysmal explosion.

4.2.3 Linear inversion of effusive eruption

When a pressure source is set to be at the best-fit spherical pressure source location of the ordinary explosion, the misfit J is 24.0%, and the observed ground deflation of lava effusion is also well explained. We thus interpret that the depressurization source associated with lava effusion is located in the same portion of the shallow magma system as the explosive activities. We then assume the same source configurations as the best-fit ellipsoidal model of 100×150×100 m at the elevation of 500 m a.s.l. and linearly estimate a pressure change of -1.27 MPa with a misfit of 25.9%. (step 4 in Figure 4.3; Figure 4.7). The best-fit model can also well explain the ground deformation pattern of the effusive eruption. We conclude that, at Stromboli, three types of eruptive activity (ordinary explosion, paroxysm and lava effusion) share a common pressure source in the shallow plumbing system.

4.3 Validation of inversion results

4.3.1 Resolution of the inversion results

In this study, the source parameters, especially SY and SZ, are weakly constrained for all the calculated inversions. For each of the independent inversion with a spherical source, the top 5% of the smallest misfit is basically 2–3 grids (50–100 m), 4–5 grids (150–200 m) and 6 grids (250 m) for SX, SY and SZ, respectively. The weak constraint on SY (northwest-southeast) is due to the lack of stations in the Sciara del Fuoco, northwest of the summit craters. Besides, the constraint on SZ (elevation) is probably improved by increasing the vertical coverage of stations. This means that it is still necessary to extend

the coverage of tilt stations to improve the constraints on these model parameters.

The best-fit model using the joint inversion of the ellipsoidal source increases the fitting at PZZ and LFS, but we find it difficult to reproduce the direction of the observed tilt at CPL and LFS. We searched for a model that minimizes the misfit at CPL and LFS among the forward models calculated for the inversions with a sperical source (539 models), but we could not find such a model. We also calculated several forward models with an oblate or rectangular shape as a representative of a crack-like pressure source. We tested similar source geometries to the previous studies that estimated the seismic or geodetic source to be a northeast-southwest crack (Chouet et al., 2003[51]; Mattia et al., 2004[124]), but they can not reproduce both tilt vectors of CPL and LFS. As the misfit is not significantly reduced by these forward models, we suggest that the nearly spherical source estimated in our inversions is a better candidate for a pressure source model than the others. Another explanation for these large misfits might be complexities not included in our pressure source models, such as local mechanical boundaries (e.g. local cracks along NE-SW) or heterogeneity of elastic properties related to a structural anomaly of density (Linde et al., 2014[113]) and seismic velocity (Patanè et al., 2017[147]). Stations with large misfits, CPL and LFS, are located along the northeast or southwest side of the summit craters so they may be affected by pre-existing cracks or dyke intrusion linked to effusive eruptions (Valade et al., 2016[198]).

4.3.2 Effect of pressure source radius

While the horizontal position SX of the centroid is relatively well constrained, whereas the SY and SZ coordinates do not converge well. The shape of the ellipsoid (semiaxes a, b, c) shows trade-offs among each other (Figure 4.6a), with aspect ratios of $b > a \approx c$. As expected, there is also a trade-off (Figure 4.6a) between the pressure change ΔP and the source volume ($V = 4/3\pi abc$), that is a large source with a small pressure change generates similar deformation to a small source with a large pressure change. On the other hand, the moments of the source ($V\Delta P$) are well constrained at $\sim 0.16 \times 10^9$ Nm for the ordinary explosions and $\sim 5.6 \times 10^9$ Nm for the paroxysm, respectively.

To confirm this trade-off between the size (volume) and the pressure change of the source, we evaluate the sensitivity of varying sphere radius a_0 at the constant location of the best-fit spherical model ($(SX, SY, SZ) = (-50, -100, 550)$). Figure 4.9 shows the joint misfit of ordinary and paroxysm (eq. 4.3) and the volume-pressure trade-off calculated

for $a_0 = 10, 20, 50, 100, 150, 200, 250$ m. The result clearly confirms the low sensitivity of source radius a_0 to the misfit and thus the trade-off. This means that it is difficult to constrain the radius of the pressure source separately from the pressure change, which has been assumed to be 100 m in this study based on *a priori* information from previous studies. In Chapter 5, we show the validity of the assumed source radius (100 m) by other independent constraints on the pressure change using measured magma discharge and a mechanical model of magma ascent in the conduit.

4.3.3 Inversions with weighted least square criterion

We evaluate the stability of inversion results depending on the criterion of misfit evaluation. In this study, we did not consider the uncertainty of observed tilt vectors to evaluate the misfit function for grid searches (eq. 4.2). Here, we use another misfit function of the weighted residual sum of squares:

$$J^{weighted} = \sqrt{\frac{\Sigma_{i=1}^{N} \sigma_i^{-2} (\tau_i^{obs} - \tau_i^{calc})^2}{\Sigma_{i=1}^{N} \sigma_i^{-2} (\tau_i^{calc})^2}} \times 100[\%], \tag{4.4}$$

where σ_i is the standard deviation of the observed tilt. For ordinary explosions, we take the standard errors of each component (green error bars in Figure 3.16b) transformed from those of the tilt amplitude and azimuth distribution of 868 selected events (Figure 3.6). For paroxysmal explosion, we simply use the standard deviation of tilt records from 10:00 to 13:00 on 3 July 2019 as plotted in Figures 3.15 and 3.16.

Figure 4.8 indicates inversion results with a spherical source assuming the weighted misfit (eq. 4.4). The best-fit model for ordinary explosion (Figure 4.8a) is estimated at the same location as the independent inversion without observation errors (eq. 4.2, Figure 4.4a), with very similar misfit distributions. This result probably reflects that the variation of tilt uncertainties within different stations used for inversion of ordinary explosion is smaller than that for paroxysm. On the other hand, the best-fit model for paroxysmal explosion (Figure 4.8b) is estimated at $(SX, SY, SZ) = (0, -100, 450)$, although the independent inversion without observation errors (eq. 4.2, Figure 4.4b) results in $(SX, SY, SZ) = (-50, -100, 550)$, which differs one or two grids (50 or 100 m). Misfit distributions are also different from non-weighted ones. These discrepancies are due to the relatively large differences in noise level among tilt and seismic stations for the paroxysm (Figure 3.16). OHO and PZZ clearly show a higher signal-to-noise ratio than the other stations. In fact, the misfit in these two stations is well reduced (Figure 4.8d). Consequently,

joint inversion returns the same best-fit location as the weighted independent inversion of the paroxysm, which reflects a difference of minimum misfit for ordinary (33.9%) and paroxysm (19.4%) (Figure 4.8c).

4.3.4 Selection of the best-fit model

In the joint inversions, the ellipsoidal source (misfit $J = 27.6\%$) improves model fitting to the observed tilt with the spherical source (misfit $J = 29.6\%$). Because the improvement in the misfit is small (2.0%), the inversion with an ellipsoidal source may cause an over-fitting as the number of model parameters (6: SX, SY, SZ, a, b, c) is larger than that of spherical source (3: SX, SY, SZ). Hence, we examine the two best-fit models using Akaike Information Criterion (AIC). We use the finite correction of AIC (Sugiura, 1978[186]). The AIC value with the finite correction for the number of parameters k and the number of total samples n can be expressed as follow:

$$\mathrm{cAIC} = n(\log 2\pi + 1) + n \log \sigma^2_{min} + 2k + \frac{2k(k+1)}{n-k-1}, \tag{4.5}$$

where σ^2_{min} is the variance calculated by the model with minimum misfit and the observed tilt as $\sigma^2_{min} = \sum_i^n (\tau_i^{obs} - \tau_{min}^{calc})^2/(n-1)$. We use $n = 2$ components $\times 11$ stations $= 22$. c-AICs are calculated to be 140.61 and 147.70 for the spherical source ($k = 3$) and the ellipsoidal source ($k = 6$), respectively. This results suggests that the spherical source (smaller c-AIC value) may be a better model in terms of balance between model fitting and generalization.

Although the spherical source is better based on AIC, we choose the ellipsoidal source as the best model according to the following comparisons in Chapter 5 Discussion. Because only b is different in spherical ($b = 100$) and ellipsoidal ($b = 150$) models, pressure changes estimated for each model are in the same order (for example, sphere: 4.6 kPa and ellipsoid: 2.6 kPa for ordinary explosion). This means that the model selection (sphere or ellipsoid) does not have significant impact on the following discussion.

4.4 Summary

We inverted for the observed tilt vectors associated with the ordinary explosions, the 3 July 2019 paroxysm and the 7 August 2014 lava effusion to determine the location and the shape of the pressure source. Ground deformation is calculated by a finite element method (FEM) to include the effect of the surface topography. The pressure source is modelled

as an ellipsoidal cavity whose X-axis is aligned to E50°N (coordinate $(SX, SYSZ)$). The best-fit location for the ordinary explosion is estimated beneath the summit crater area at $(SX, SYSZ) = (-50, -100, 500)$ m, which is only one grid lower (-50 m in SZ) than that for paroxysmal explosion ($(SX, SYSZ) = (-50, -100, 550)$ m). For lava effusion, the best-fit model is located at $(SX, SYSZ) = (-100, -200, 450)$, which is apart horizontally $\sim$150 m from the central crater. Although these independent inversions returned slightly different locations of best-fit models, these results suggest that the pressure source of these eruptions is commonly located at a range of shallow ($<\sim$400 m depth, $>$400 m a.s.l.) portion of magma plumbing system beneath the summit crater area ($<\sim$200 m from the central crater). The best-fit model of the joint inversion that combines two datasets of the ordinary and paroxysmal explosion is estimated at the same location as that of the ordinary explosion ($(SX, SYSZ) = (-50, -100, 500)$ m) with the joint misfit of 29.7%. Ellipsoidal models are further calculated to evaluate if they can improve the fitness of tilt vectors and results in $(a, b, c) = (100, 150, 100)$ m with the joint misfit of 27.6%. However, the shape of the pressure source is weakly constrained to be ($b \geq a \approx c$). Constraint on the volume V and pressure change ΔP of the pressure source is very limited due to the trade-off. This ellipsoidal source can also well reproduce the deflation during lava effusion as the misfit of 25.9%. We assume this ellipsoidal source and corresponsding pressure change for ordinary explosion (2.6 kPa), paroxysm (0.089 MPa) and lava effusion (-1.27 MPa) to be the best-fit model parameters. In the following discussion, we firstly demonstrate the reliability of the source geometry and the depresurization associated with lava effusion (-1.27 MPa). This will consequently support the reliability of the estimated pressure changes for ordinary explosion and paroxysm, which will be used for further discussions.

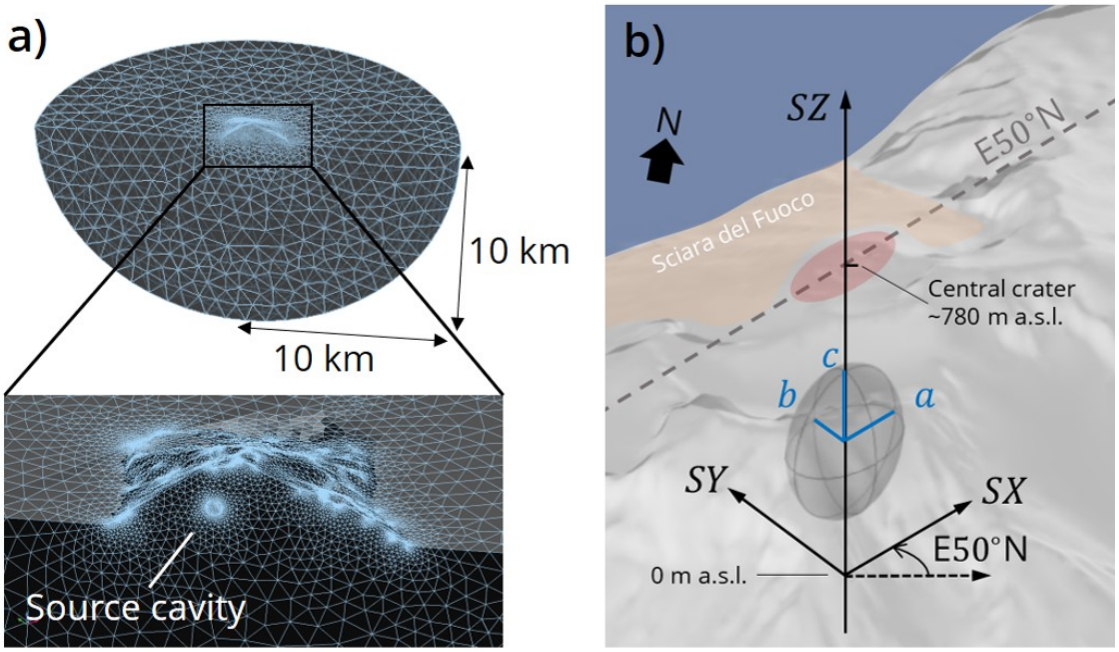

Figure 4.1: Geometry of the FE model and coordinate system (a) Cross-section of the FE model. The model is constructed by a hemisphere with a 10 km radius, a digital elevation model and a source cavity. The mesh resolution shown in (a) is coarser than that of actual calculations for visibility. (b) Definition of the coordinate system and source parameters.

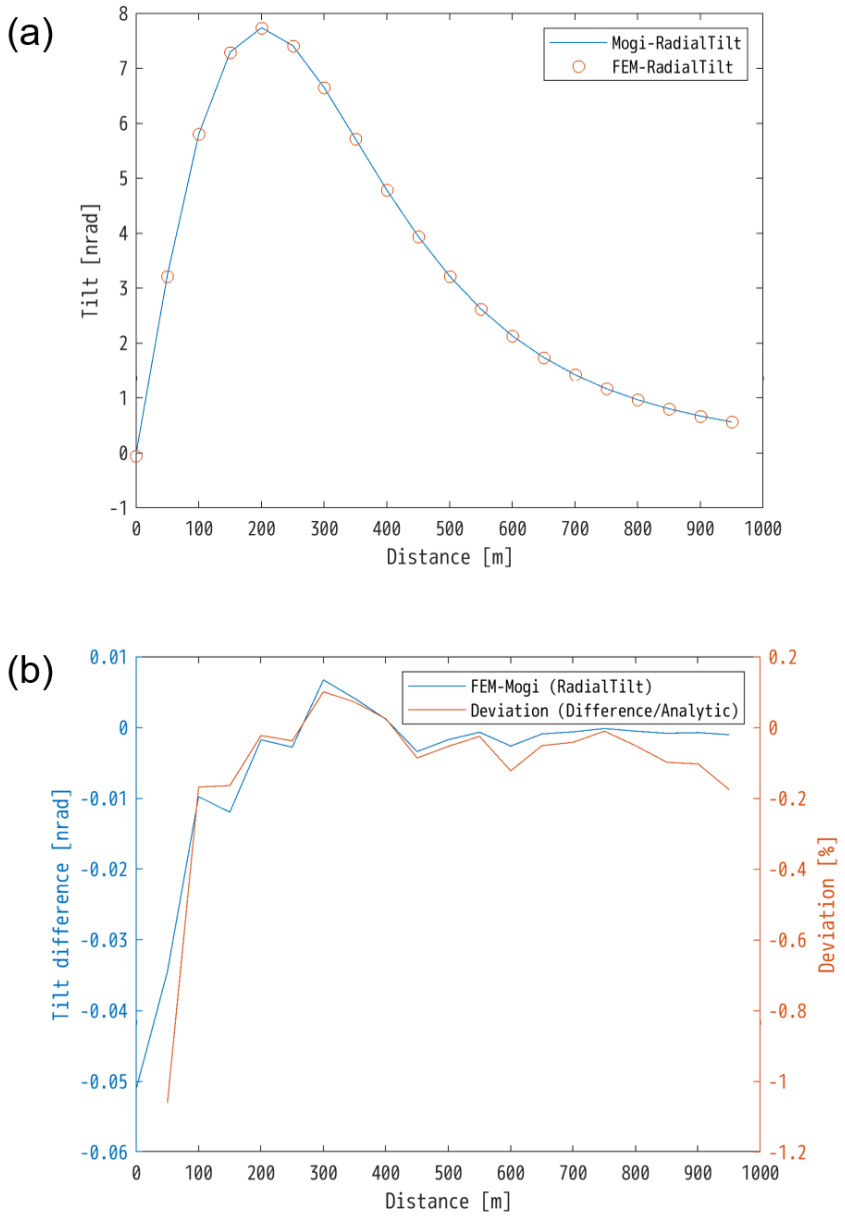

Figure 4.2: Benchmark test of the FE model. (a) The radial tilt of a spherical source with a radius of 10 m at a depth of 300 m. Blue and red lines indicate analytical solution (Mogi, 1958) and numerical solution (FEM), respectively. (b) Tilt difference (numerical-analytical) and deviation (difference/analytical)×100%.

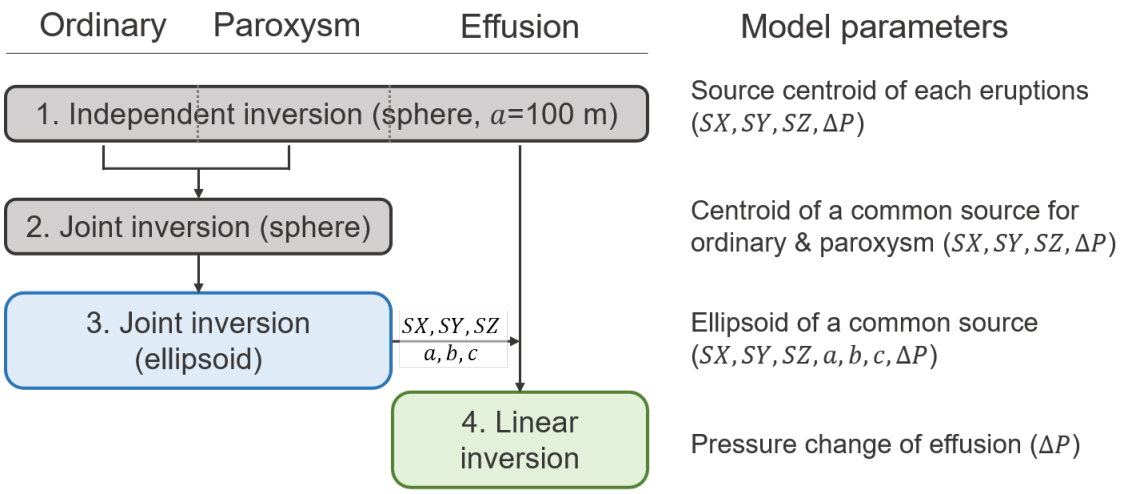

Figure 4.3: Work flow of the grid-search inversions.

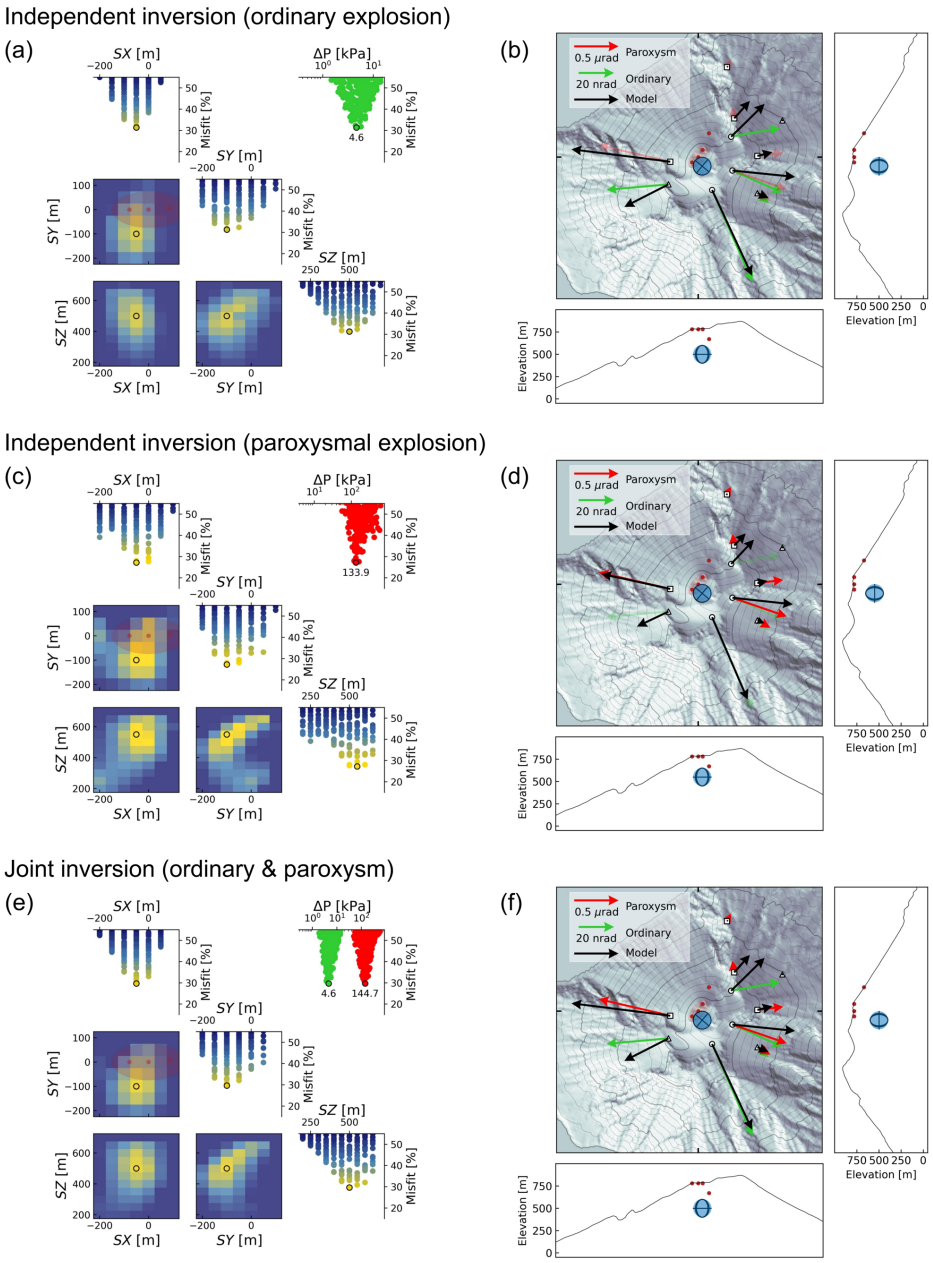

Figure 4.4: Inversions of ordinary and paroxysmal explosions using a spherical source. Independent inversion of ordinary explosions in 2014 (a and b), the July 2019 paroxysmal explosion (c and d) and joint inversion of both events (e and f). (a)(c)(e) Distributions of model parameters (SX, SY, SZ) with the misfit J in the inversion. 1-D distributions for individual parameters are shown in the diagonals. Correlations between pairs of the parameters are shown in the off-diagonals. The area of the summit crater terrace and vents are plotted in a SX-SY correlation map. 1-D distribution for the pressure change ΔP is plotted in the upper-right (ordinary: green; paroxysm: red). The best-fit model (minimum misfit) is marked by a black circle. (b)(d)(f) Tilt vectors of the ordinary explosion (green), the July 2019 paroxysm (red), and the best-fit model (black) are shown. The eruptive craters are marked by red circles. The projection of the sphere is drawn by black curves (sphere's three axes) and filled with a dark blue (sphere's body).

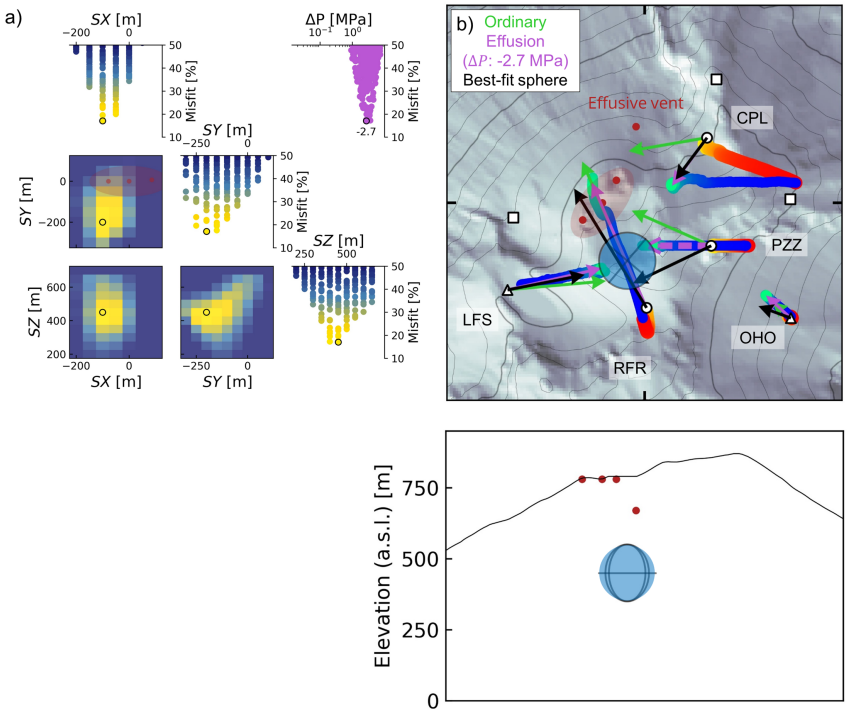

Figure 4.5: Independent inversion of lava effusion using a spherical source. (a) Distributions of model parameters (SX, SY, SZ) with the misfit J in the inversion for a spherical source. 1-D distributions for individual parameters are shown in the diagonals. Correlations between pairs of the parameters are shown in the off-diagonals. The area of the summit crater terrace and vents are plotted in a SX-SY correlation map. 1-D distribution for the pressure change ΔP is plotted in the upper-right with purple dots. The best-fit model (minimum misfit) is marked by a black circle. (b) Tilt vectors of the ordinary explosion (green, reverse direction), the 7 August 2014 effusive eruption (purple), and the best-fit model (black) are shown. The eruptive craters are marked by red circles. The projection of the sphere is drawn by black curves (sphere's three axes) and filed with a dark blue (sphere's body). Tilt vector motions during the preceding phase (-15 h to 0 h; yellow to red) and effusive phase (0 h to +48 h; blue to green). The new effusive vent at ~670 m a.s.l. in the Sciara del Fuoco and the summit craters are marked by red circles.

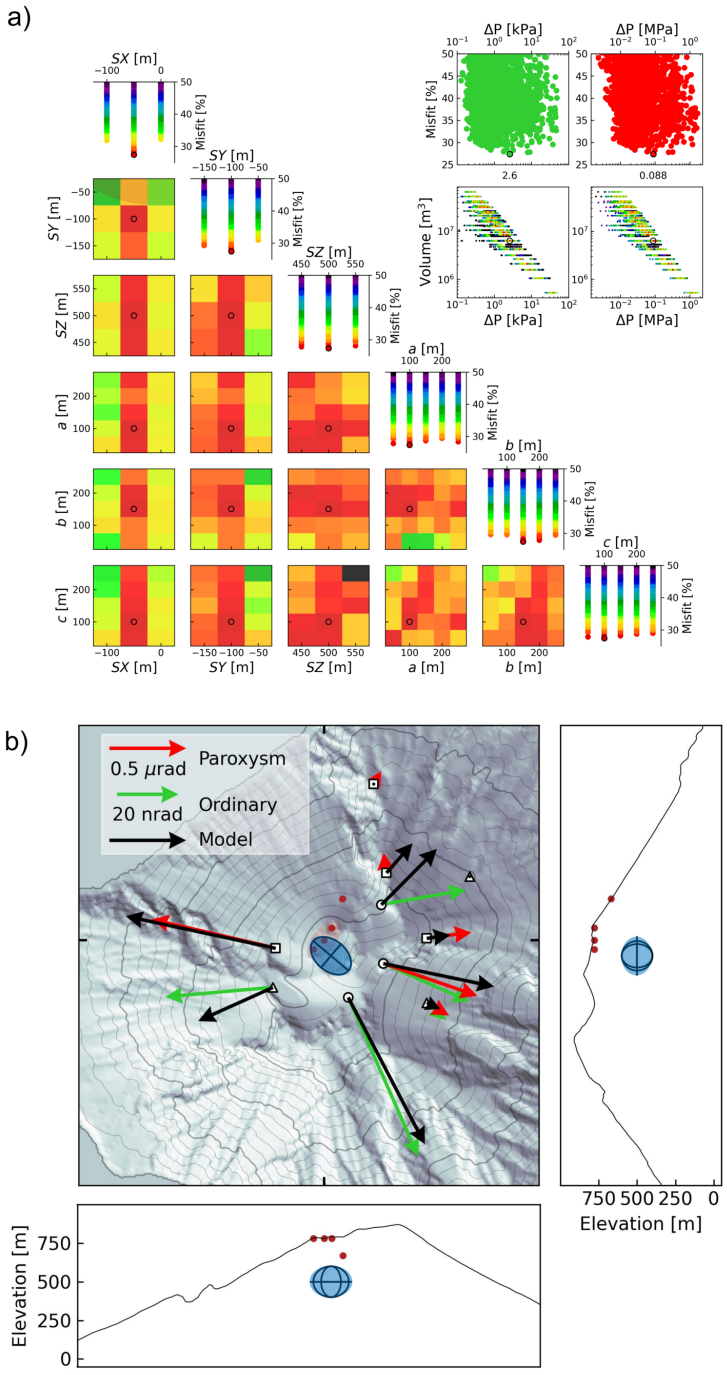

Figure 4.6: Joint inversion of the ordinary explosion and the July 2019 paroxysm using an ellipsoidal source. (a) Distributions of model parameters (SX, SY, SZ, a, b, c) with the misfit J in the inversion. 1-D distributions for individual parameters are shown in the diagonals. Parameter trade-offs between the pressure change and the volume of the source are shown in the upper right. The best-fit model (minimum misfit) is marked by a black circle. (ordinary: green; paroxysm: red). (b) Tilt vectors of the ordinary explosion (green), the July 2019 paroxysm (red), and the best-fit model (black) are shown. The eruptive craters are marked by red circles. The projection of the sphere is drawn by black curves (sphere's three axes) and filed with a dark blue (sphere's body).

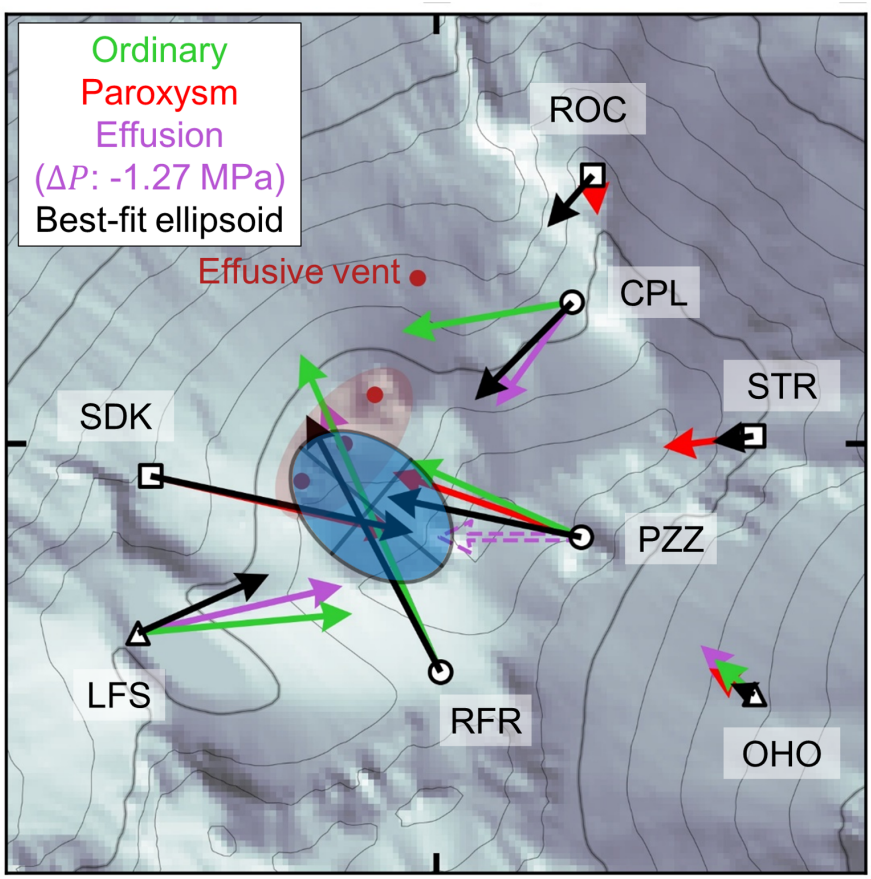

Figure 4.7: Comparison of the tilt vectors calculated from the best-fit ellipsoid in Section (black) with the observed ones: the ordinary explosion (green), the 3 July 2019 paroxysm (red) and the 7 August 2014 effusive eruption (purple). Note that the vectors for the ordinary explosion and paroxysm are shown in reverse directions. The best-fit pressure source is shown as a dark blue ellipsoid with black curves (ellipsoid's three axes). The new effusive vent at ~670 m a.s.l. in the Sciara del Fuoco and the summit craters are marked by red circles.

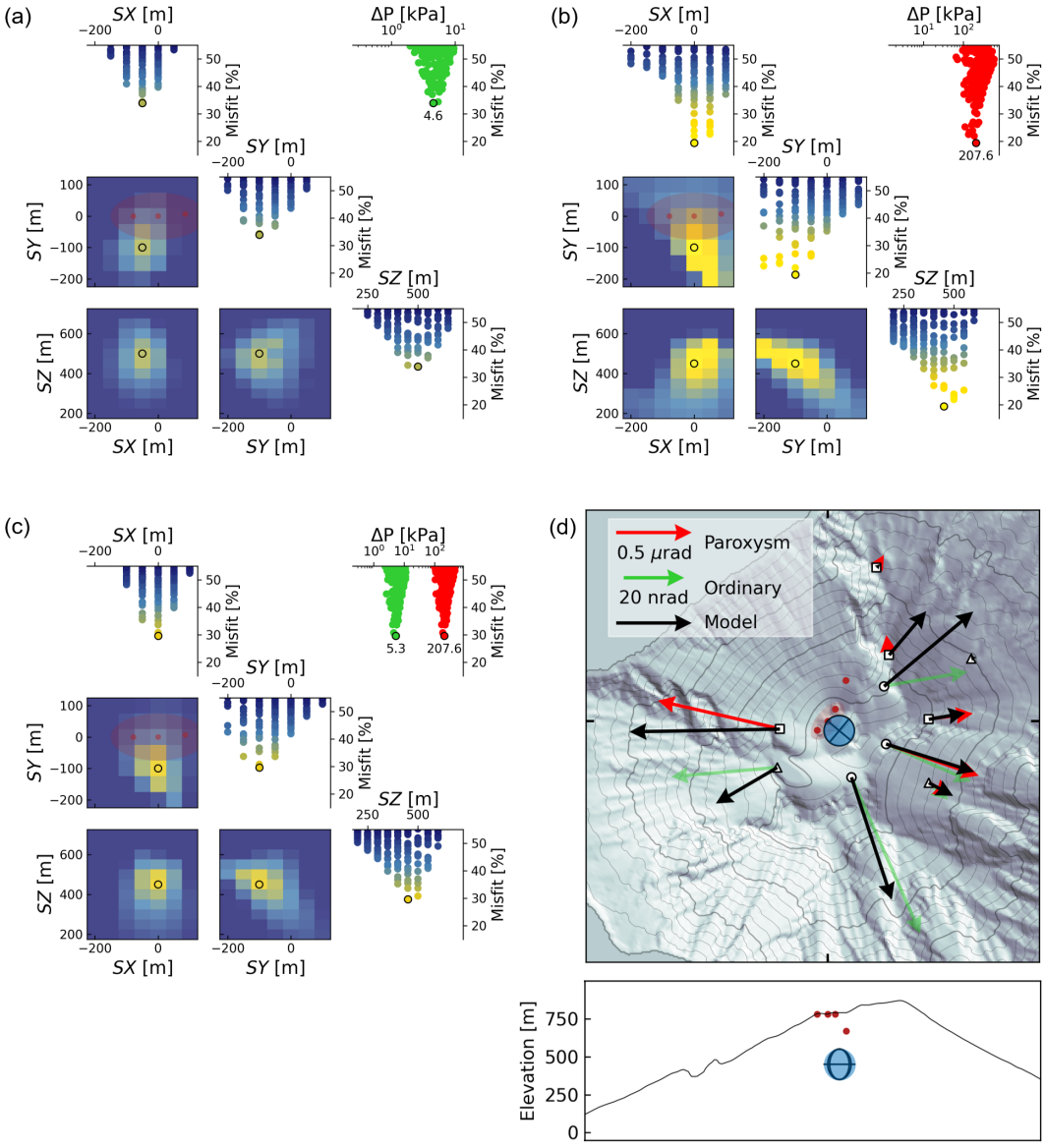

Figure 4.8: Inversions of ordinary explosion and paroxysm using a spherical source with the weighted least-square criterion. Independent inversion of ordinary explosions in 2014 (a), the July 2019 paroxysmal explosion (b) and joint inversion of both events (c). (a)(b)(c) Distributions of model parameters (SX, SY, SZ) with the misfit J in the inversion. 1-D distributions for individual parameters are shown in the diagonals. Correlations between pairs of the parameters are shown in the off-diagonals. The area of the summit crater terrace and vents are plotted in a SX-SY correlation map. 1-D distribution for the pressure change ΔP is plotted in the upper-right (ordinary: green; paroxysm: red). The best-fit model (minimum misfit) is marked by a black circle. (d) Tilt vectors of the ordinary explosion (green), the July 2019 paroxysm (red), and the best-fit model (black) of the joint inversion (c) are shown. The eruptive craters are marked by red circles. The projection of the sphere is drawn by black curves (sphere's three axes) and filled with a dark blue (sphere's body).

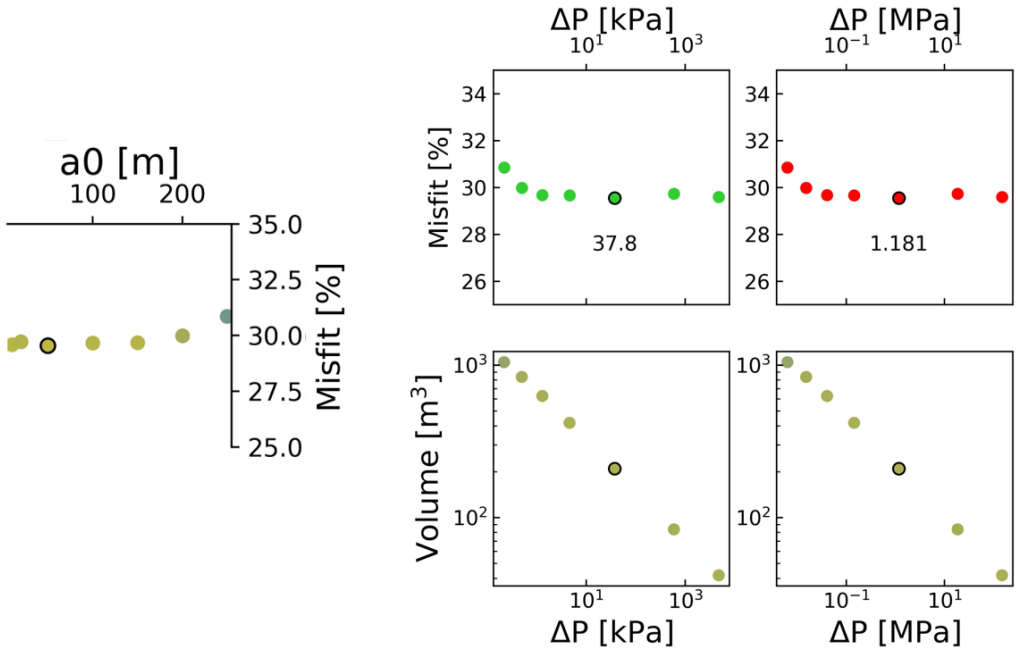

Figure 4.9: Misfit distribution of varying sphere radius a_0. The trade-off between the volume $V = 4/3\pi a_0^3$ and the pressure change ΔP is plotted.

Chapter 5

Discussion

5.1 Reliability of the estimated pressure source from the view of caldera-forming effusive eruption

Our inversion results show that the best-fit common source model derived for ordinary and paroxysmal explosions well explains the ground tilt vectors of the 2014 effusive eruption that accompanied a caldera collapse. Here, we firstly discuss the reliability of the result ($100 \times 150 \times 100$ m ellipsoid and its associated pressure changes) from the view of caldera collapse. We show how the geometry of the source and the amount of effusion-induced depressurization is reliable by referring to an analogue experiment and a mechanical model of lava effusion.

We validate the geometry of the estimated pressure source model from the aspect of caldera collapse. The exponential ground deflation after the effusion onset was accompanied by a progressive internal collapse of the crater walls (Valade et al., 2016[198]). These features are common to the latest effusive eruptions at Stromboli in 2002 and 2007 (Ripepe et al., 2017[165]) and generally observed in other caldera-forming effusive eruptions at basaltic volcanoes around the world (e.g. 2007 Piton de la Fournaise, Michon et al., 2007[130]; 2014 Bardarbunga, Gudmundsson et al., 2016[81]; 2018 Kilauea, Neal et al., 2019[134]). Since our estimated source depth is 280 m from the bottom of craters, the roof of the source comes to locate at ∼200 m beneath the surface (Figure 14a). Considering this subsidence as a caldera collapse, an aspect ratio of the reservoir roof width (diameter of the caldera, ∼200 m) to the reservoir roof thickness (∼200 m) is ∼1. Roche et al. (2000)[169] investigated the relationship between the aspect ratio and the amount

of subsidence based on analogue sand experiments. They demonstrated that the analogue calderas with an aspect ratio of 1 (5 cm thickness and 5 cm width) generate 0.65–1.5 cm (13–30% of the roof thickness and width) of subsidence. Scaling this result to Stromboli, we estimate the subsidence of 26–60 m, which is in good agreement with the observed subsidence of ∼45 m. This provides posterior support to the reliability of the geometry of our estimated source model.

Next, we demonstrate the validity of the estimated value of depressurization. The caldera collapse following the effusive eruption is associated with gravity-driven drainage of the magma column above the effusive vent (Ripepe et al., 2015[161] and 2017[165]; Gudmundsson et al., 2016[81]; Coppola et al., 2017[54]; Roman and Lundgren, 2021[171]). Therefore, we assume that the estimated pressure decrease recorded by tilt is equivalent to the magma-static pressure change ΔP (-1.27 MPa) associated with the effusion of the magma column induced by the gravity-driven magma drainage model. Assuming a cylindrical magma column with a radius R of 87 m (Ripepe et al. 2017[165]), we simplify the volume of effused magma V_E as:

$$V_E = \frac{\pi R^2}{g(1-\phi)\rho_{DRE}}\Delta P, \tag{5.1}$$

where ρ_{DRE} is the dense-rock-equivalent (DRE) density, ϕ is the vesicularity, and g is the gravitational acceleration. Assuming a vesicularity between 0 and 0.45 (Landi et al., 2009[107]) and a density $\rho_{DRE} = 2950$ kg/m^3 (Pioli et al., 2014[154]), we calculate a volume of effused magma V_E of 1.0–1.9$\times 10^6$ m^3. These values are almost equal to the volume of $\sim 1.6 \times 10^6$ m^3 previously measured by thermal anomalies (Valade et al., 2016[198]). This suggests that our inferred pressure change is consistent with the depressurization induced by the magma discharge from the conduit above the pressure source. Besides, this agreement also supports the reliability of the model parameters of our best-fit source inferred for the ground tilt measured during the ordinary and paroxysmal explosions, most notably for the volume ($100 \times 150 \times 100$ m), through the uncertain relationship between the volume and the pressure change ($V\Delta P$) as mentioned in Chapter 4. In the following, we thus use the estimated pressure changes of the ellipsoidal source for ordinary explosion (2.6 kPa) and paroxysm (0.089 MPa) to discuss the pressurization process of the source, assuming these pressure changes (and source volume) are constrained according to the discussion in this section 5.1.

5.2 Mechanical model of pressurization process of the source

5.2.1 Magma plumbing system of Stromboli volcano

The centroidal source depth of ~ -280 m (500 m a.s.l., Figure 5.1) found by the inversion of the ground deformation associated with ordinary explosions, paroxysms and effusive eruption agrees with many other previous studies (Chouet et al., 2003[51]; Mattia et al., 2004[124]; Marchetti and Ripepe, 2005[118]; Cesca et al., 2007[49]; Genco and Ripepe, 2010[76]; Ripepe et al., 2015[161]; Ripepe et al., 2021a[163], b[160]; Sugimura et al., 2021[185]), and it implies a shallow small magma reservoir or dyke-like feeding system. The horizontal location of the deformation source is also in good agreement with recent studies (Viccaro et al., 2021[202]; Ripepe et al., 2021a[163] and b[160]; Sugimura et al., 2021[185]; Mattia et al., 2021[123]), but it does not match with previous results that locate the centroid of the source outside the crater area and in the Sciara del Fuoco (e.g. Chouet et al., 2003[51]; Mattia et al., 2004[124]). This disagreement is most probably related to the poor coverage of the northwest part of the volcano edifice in the previous studies. The inferred size ($\sim$100 m) of the pressure source of gradual inflation may be also consistent with the lateral migration (50 m) of the seismic VLP source (Sugimura et al., 2021[185]). Besides, we do not have evidence of deformation induced by the deep magma storage at $\sim$1.5 km depth b.s.l. (Bonaccorso et al., 2008[39]; 2009[34]; 2012[35]; Patané et al., 2017[147]) interpreted as the reservoir of the HP magma (Burton et al., 2007[40]; Métrich et al., 2010[127]; Calvari et al., 2011[42]; Métrich et al., 2021[129]) feeding the ordinary Strombolian activity and the effusive eruptions. On the other hand, ground deformation recorded during explosive eruptions, as well as effusive one, shows amplitude increasing of almost one order of magnitude from the base towards the summit, suggesting a source better confined in the upper part rather than rooted deep in the volcano edifice.

Following the previous studies and our modelling of the 2014 effusive eruption, we then interpret that the estimated source of the ground deformation represents the shallow reservoir with $\sim$100 m radius feeding the active summit craters with narrow (diameter of $<\sim 5$ m) conduits. This shallow reservoir is inferred to be filled with highly degassed, viscous, denser stagnant magma, or crystal mush layer beneath the plug and supported by a mobile magma column where convective gas-liquid flows (Stevenson and Brake, 1998[182]; Suckale et al., 2016[184]; Barth et al., 2019[22]). Gas bubbles accumulate beneath this stagnant magma and are injected into the mush layer intermittently. The gas-rich magma

that accumulates below the stagnant magma may build up a pressure in the mush and induce a rise of the magma free surface.

5.2.2 Mechanical model

We model the mechanical process of pre-explosive ground inflation measured by the ground tilt with the uplift of the magma free surface in a narrow conduit connected to the magma reservoir (Figure 5.2). Several conduits might be necessary to be considered because several active vents that erupt are recognized in the crater area (i.e. NE, C and SW craters, Figure 5.1). In the present study, however, we assume one conduit connected with a magma reservoir as an ordinary explosion occurs at one of active vents. When two or three conduits are considered, the following estimations come to be changed by several factors but not in the order of magnitude. In such an open conduit-reservoir system, the pressure of the magma reservoir consists of the sum of static pressure generated by the magma column in the conduit and dynamic pressure associated with fluid flow in the conduit. When the reservoir is pressurized by magma supply from a deeper part, the height of the magma column in the conduit increases in response to the corresponding pressure increase in the reservoir. This height change of magma surface can be observed in other basaltic open-vent volcanoes with lava lakes, for example, Kilauea volcano in Hawaii. We thus use the same model that relates the pressure change of the reservoir to lava lake level change (Anderson et al., 2015[14]). We assume that the magma system is filled with a homogeneous liquid magma with the density ρ_l and the viscosity η. The magma-static pressure change ΔP^{stat} caused by the magma surface uplift Δh is expressed as

$$\Delta P^{stat} = \rho_l g \Delta h, \tag{5.2}$$

where g is the gravitational acceleration. From the volume change of magma in the cylindrical conduit with the radius of r calculated by $\Delta V = \pi r^2 \Delta h$, the pressure change ΔP^{stat} can be converted to the volume change as

$$\Delta V = \frac{\pi r^2}{\rho_l g} \Delta P^{stat}. \tag{5.3}$$

When the magma flow towards the vent is approximated as laminar flow in the cylindrical conduit driven by the pressure gradient (Poiseuille flow, e.g. Hreinsdóttir et al., 2014[91]), the pressure change beneath the conduit caused by the viscous magma flow is represented

by

$$\Delta P^{flow} = \frac{8\eta L}{r^2} u, \tag{5.4}$$

where $L = z_2 - z_1$ is the length of the conduit, z_2 is the depth of the conduit inlet, z_1 is the initial magma head depth, u is the flow velocity of magma in the conduit. Therefore, the pressure changes of the shallow magma reservoir estimated in our inversion ΔP can be represented as the sum of these two pressurization processes:

$$\Delta P = \Delta P^{stat} + \Delta P^{flow} = \rho_l g \Delta h + \frac{8\eta L}{r^2} u = \frac{\rho_l g}{\pi r^2} \Delta V + \frac{8\eta L}{r^2} u. \tag{5.5}$$

Equation (5.5) relates the estimated pressure change ΔP to the other physical parameters of magma discharge estimated by field measurement, which is, for example, the volume of magma discharge and upward velocity of the magma free surface.

5.2.3 Ordinary explosion

First, we evaluate the contribution of the two pressurization processes to the ordinary explosion. When the magma migrates upward in the conduit with a flow velocity u, the uplift of magma surface Δh can be expressed as $\Delta h = u\Delta t$, where Δt is the duration of ground inflation. In this case, the pressure change of the magma reservoir (Eq. 5.5) is expressed as:

$$\Delta P = \Delta P^{stat}(1 + \psi), \tag{5.6}$$

where $\psi = 8\eta L / \rho_l g r^2 \Delta t$ is the ratio of the flow-driving overpressure (ΔP^{flow}) to the magma-static overpressure (ΔP^{stat}). We use magma viscosity $\eta = 10^3$ Pa s (Kawaguchi and Nishimura, 2015[102]), conduit radius $r = 2.5 \pm 1.0$ m (Delle Donne and Ripepe, 2012[59]) and magma density $\rho_l = 2700$ kg/m^3 for the HP magma (Métrich et al., 2001[128]). The depth of the conduit inlet and the initial magma head depth are set to be $z_2 = 180$ m (∼600 m a.s.l.; upper edge of our best-fit ellipsoid and the source location of the VLP signal, Sugimura et al., 2021[185], Ripepe et al., 2021b[160]) and $z_1 = 30$ m (Harris and Ripepe, 2007[83]; Delle Donne and Ripepe, 2012[59]), respectively. The conduit length L is thus 150 m. Using the median duration time for gradual inflation (stage A) Δt of 215 s (Figure 3.4a), we obtain ψ =0.002–0.06. This indicates that the contribution of the flow-driving overpressure ΔP^{flow} is about two orders of magnitude smaller than the magma-static overpressure ΔP^{stat}. Because magma in the conduit at the

shallowest part (< 200 m depth), especially top a few meters is considered to be highly viscous more than 10^4 Pa s (Métrich et al., 2001[128]; Gurioli et al., 2014[82]). If we use larger viscosity $\eta = 10^4$ Pa s which is estimated by petrological analysis of HP magma scoria (Métrich et al., 2001[128]), we obtain ψ =0.02–0.6, which still indicates the smaller contribution of the flow-driving overpressure. Hence, the pressure increase for the ordinary explosion is assumed as follows:

$$\Delta P \simeq \Delta P^{stat} = \frac{\rho_l g}{\pi r^2} \Delta V. \tag{5.7}$$

For ordinary explosion, the pressure change is estimated to be ΔP=2.6 kPa using gradual inflation (stage A) (Figure 4.6). We consider the uncertainty of the estimated pressure change as 1.3 kPa (50% of the median) based on the tilt amplitude distributions (Figure 3.6). Assuming the conduit radius $r = 2.5 \pm 1.0$ m (Delle Donne and Ripepe, 2012[59]) and $\rho_l = 2700$ kg/m^3 for the HP magma (Métrich et al., 2001[128]), we calculate the magma surface uplift Δh =0.05–0.15 m and a volume change of magma ΔV =0.11–3.7 m^3. We convert the volume change of magma in the conduit to the volume of magma discharge measured by field observation by using a relation of $\Delta V^{'} = \Delta V/(1-\phi)$, where ϕ is the vesicularity of ejected materials. Using $\phi = 0.7$ for the ejected scoria (Lautze and Houghton, 2007[109]; 2008[110]), we obtain $\Delta V^{'}$ =0.36–12 m^3. This is in very good agreement with the typical volume range of materials ejected during a single ordinary explosion (1–30 m^3 of Ripepe et al., 1993[167]; Patrick et al., 2007[148]; Gaudin et al., 2014[75]; Bombrun et al., 2015[31]). This means that magma volume corresponding to the uplift of the magma surface due to the increase of magma-static pressure generated by the gas and magma supply is almost equal to the volume of ejected magma. This balance of pressure accumulation and release may control the stability of the long-lasting ordinary activity at Stromboli (Rosi et al., 2000[173]) because the magma free surface height is kept during repetitive Strombolain activities. If the volume discharge of a single ordinary explosion V_E does not balance with the volume increase $\Delta V^{'}$ in the conduit before the explosion, magma free surface must rapidly increase ($\Delta V^{'} > V_E$) or decrease ($\Delta V^{'} < V_E$), which will lead to different eruptive activity such as lava flow or disappearance of magma ejection.

This estimated volume corresponds to the amplitude of the gradual inflation stage A, which is at least ∼2 times smaller than the amplitude of the rapid inflation (stage B) (Figure 3.5). In the previous inversions and discussion, we focused on gradual inflation

(stage A) because the rapid inflation (stage B) might include a contribution of the translational motions associated with the seismic VLP signal. Therefore, tilt amplitude and corresponding pressure change are indefinable for the full ground inflation. Because the average tilt vectors of the gradual inflation (stage A) and rapid inflation (stage B) are generally similar and our source location is in good agreement with the location derived by using the full ground deformation waveform (Ripepe et al., 2021a[163]), we suppose that the stages A and B represent the full ground inflation. We also assume that the uncertain contribution of the translational motions associated with the seismic VLP signals is very limited and can be neglected (Ripepe et al., 2021b[160]). Although these are assumptions based on uncertain evidence, we can calculate the pressure of the full ground inflation as three times the pressure change for the gradual inflation. Using then the pressure of $2.6 \times 3 = 7.8$ kPa, we calculate a volume change of $\Delta V^{'}$ =1.7–23 m^3. This range also agrees with the measured volume of magma discharge.

On the other hand, in stage B, the gas bubbles may rapidly ascend in the upper part of the eruptive conduit so that additional magma pressure is built up due to the resistance of the conduit flow capped by a highly viscous layer at the top of the magma head (Kawaguchi and Nishimura, 2015[102]; Capponi et al., 2017[44]). We evaluate this effect by using Eq. (5.7) with tilt duration for rapid inflation (stage B) of Δt =15 s (Figure 3.4b). As a result, the ratio ψ is estimated to be 0.12–0.85 (Eq. 5.6), which indicates that the contribution of the flow-driving overpressure ΔP^{flow} is about one order of magnitude smaller or the same order as the magma-static overpressure ΔP^{stat}. This suggests that the effect of upward magma motion may contribute to the pressure increase of the reservoir during the rapid inflation ∼15 s before explosive onset.

Here, we summarize the physical process of an ordinary explosion based on our result and previous studies. Gradual inflation (A) starting ∼200 s before the onset of an explosion reflects the magma supply below the stagnant region in the shallow reservoir, which pushes the free surface of magma upwards in the conduit (A0 phase in Ripepe et al., 2021b[160], Figure 5.2b). The volume of magma consistent with the magma surface rise is comparable to the volume of magma fragments ejected during the following explosion. Rapid inflation (B) starting ∼15 s before the onset corresponds to the onset of a VLP signal, in association with a slug migration (preceding phase in Sugimura et al., 2021[185]; A1 phase in Ripepe et al., 2021b[160]). In this stage, ground deformation may be enhanced by the pressurization induced by the upward motion of magma (slug) in the conduit. After the explosive onset,

magma fragments are discharged in a short time (∼4 s; Ripepe et al., 2021b[160]). Rapid deflation (C) and recovery process (D) are caused by depressurization of the reservoir due to magma ejection, followed by a return to the initial state. These stages are linked to the oscillation of the magma column to restore magma-static equilibrium (Ripepe et al., 2021b[160]).

5.2.4 Paroxysm

Our inversion results suggest that ground inflation associated with paroxysmal explosions is generated by the same pressure source as ordinary explosions, which is considered as the primary factor that controls the self-similar inflation trend (Ripepe et al., 2021a[163]). The main factor that controls the difference in their eruption magnitudes is the escalation of gas-rich LP magma supply originating in the deep reservoir and its fast ascent in the shallow part (Métrich et al., 2021[129]; Viccaro et al., 2021[202]; Aiuppa et al., 2021[3]; Pichavant et al., 2022[151]; Figure 5.2c). Since the shallow pressure source for the paroxysm is the same as for the ordinary explosion, we apply the same model to the 3 July paroxysm with proper conduit length and magma density.

We first discuss the initial phase (−600 to −200 s) of ground inflation occurring before the paroxysmal onset, which is used for the inversion in Chapter 4. Considering the estimated pressure change $\Delta P = 0.089$ MPa, conduit radius $r = 2.5 \pm 1.0$ m, magma density $\rho_l = 2500$ kg/m^3 for the LP magma (Métrich et al., 2010[127]) and vesicularity of $\phi = 0.7$, we obtain volume change of $\Delta V' = 1.0$–3.7×10^2 m^3. This volume change is about three orders of magnitude smaller than the volume of ejected materials of $\sim 10^5$ m^3 (mass of $\sim 10^8$ kg; Giordano and De Astis, 2021[77]; Métrich et al., 2021[129]; Andronico et al., 2021[15]) measured on the ground surface. Because the amplitude of the initial phase (−600 to −200 s) of the inflation (∼0.34 μrad at OHO) used to calculate the pressure of 0.089 MPa is ∼45 times smaller than the measured maximum amplitude of the ground deformation already calculated for the full ground inflation (∼ 15 μrad at OHO; Ripepe et al., 2021a[163]), a large pressure change of $0.089 \times 15/0.34 = 3.9$ MPa is necessary to explain the volume change estimated from our ground deformation data analysis. Before the paroxysmal onset, the magma free surface was inferred to almost reach the vent ($z_1 = 0$ m) because small lava flow from the vents was observed from −45 minutes to −10 minutes (−600 s) (Giudicepietro et al., 2020[79]) and lava pouring from all vents was also observed from ∼200 s to the onset (Ripepe et al., 2021a[163]; Andronico et al., 2021[15]). Since

the estimated pressure change $\Delta P = 3.9$ MPa is equivalent to the magma surface uplift $\Delta h = 180$ m (Eq. 5.2), which overshoots the level of the vent, we suggest that the magma-static pressure is not suitable to model the pre-explosive inflation of the 3 July paroxysm. Therefore, we approximate the pressure increase as:

$$\Delta P \simeq \Delta P^{flow} = \frac{8\eta L}{r^2} u. \tag{5.8}$$

To calculate the flow velocity driven by the overpressure ΔP^{flow}, we use the parameters same as the ordinary explosion ($\eta = 10^3$–10^4 Pa s and $r = 2.5 \pm 1.0$ m). The depth of the conduit inlet and the initial magma head depth are set to be z_2 =180 m and z_1 =0 m, respectively. From a few tens of seconds before the onset of the paroxysm, lava pouring from four active vents at the summit craters was observed by cameras at the summit (Andronico et al., 2021[15]). We thus use the velocity considering the number of multiple vents $N_v = 4$:

$$u = \frac{N_v r^2}{8\eta L} \Delta P. \tag{5.9}$$

For ΔP^{flow} =3.9 MPa, the upward velocity of magma in the conduit is calculated to be 13.6–123 m/s and 1.36–12.3 m/s for the viscosity $\eta = 10^3$ and 10^4, respectively. This estimated upward velocity just before the explosive onset is well matched with the inflation velocity of magma free surface pouring from the vent during −43 s to 0 s measured by thermal imagery from the summit (∼2–30 m/s, Andronico et al., 2021) and the maximum ascent rate of expanding gas-magma mixture calculated from a conduit flow model (15.3 m/s, Ripepe et al., 2021a[163]). The estimated upward velocity is larger than the average ascent velocity of LP magma of 1–2 m/s (i.e. 1–2 hours from depths between 7 and 1.5 km) that are estimated from vesicle texture analysis (Pichavant et al., 2022[151]), and is smaller than the paroxysmal jet velocity of 200–250 m/s during 0 s to +2 s from the onset (Andronico et al., 2021[15]).

We note that a comparison of analytical solutions of ground tilt change caused by shear stress in the conduit (Nishimura, 2009[137]) with a radius of 2.5 m and a length of 180 m and pressurization of the spherical cavity (McTigue, 1987[126]) of a volume of $4/(3)\pi \times 100 \times 150 \times 100$ m^3 and a depth of 300 m returns that the contribution of shear stress is negligible (only ∼10%) in the observed tilt amplitudes. The shear stress acting on the wall induced by magma flow does not generate significant ground deformation, and ground inflation starting from ∼10 min before the paroxysm reflects the upward velocity of viscous magma flow in the conduit (Figure 5.2c).

5.2.5 Lava effusion

The mechanical process of ground deflation during lava effusion can also be explained by the magma-static pressure change similar to ordinary explosions (5.6). As shown in Section 5.1, volume decrease in the crater-terrace size conduit above the shallow magma chamber (∼87 m, Ripepe et al., 2017[165]) induced by gravity-driven magma drainage is expressed as Eq. (5.1), which indicates the same relationship to pressure change as Eq. (5.6). The magma-static pressure change in an open conduit has been applied to other basaltic eruptions, for example, the lava lake height change of Kilauea volcano (Anderson et al., 2015; Patrick et al., 2016) and large-scale effusive eruptions from the mountain flank accompanied by caldera collapse of the main plumbing system at Piton de la Fournaise, Bardarbunga and Kilauea.

5.3 Real-time calculation method of tilt signals from seismic records for improving ground deformation-based early-warning system

Monitoring sudden unexpected violent eruptions such as basaltic paroxysms and phreatic eruptions is crucial to understanding the eruptive dynamics and forecasting volcanic eruptions. Ground deformation is generated by magma or fluid transportation beneath the surface and thus is useful for detecting the eruptive precursors (Maeda et al., 2017[115]; Ripepe et al., 2021a[163]). Because these eruptions are generally small and occur in a short time, ground deformation is detectable by highly sensitive instruments such as tiltmeter, strainmeter and seismometer.

Because repetitive eruptions such as Strombolian eruption provides many pre-eruptive inflation events, there has been approaches to forecast upcoming eruptions based on ground tilt data (Manta and Taisne, 2019[116]; Ripepe et al., 2021a[163]). Manta and Taisne (2019)[116] proposed a method to infer controlling parameters (e.g. timing and magnitude) of Strombolian eruption from a single tilt station based on a Bayesian approach using a slug ascent model (James et al., 2008[97]). They tested the method to the tilt time series before eruptions of Semeru volcano, Indonesia, (Nishimura et al., 2012[139]) to show the sufficiency of the single station-based Bayesian estimation to estimate the timing and magnitude of future events. This result shows the potential of the automated tool

for real-time application for a monitoring (alert) system. Ripepe et al. (2021a)[163] developed an early warning system for paroxysms at Stromboli volcano. They applied a real-time pattern matching analysis of continuous tilt data with a template waveform calculated by the theoretical ground deformation (Nishimura, 2009[137]). This algorithm is tested using the tilt records from 2006 to 2020 (14 years) and it successfully identifies the paroxysms about 5 min before the onsets without any false alerts. At present, this early warning system is fully operational at Stromboli volcano. In the data analysis of paroxysms in this study, tilt signals are retrieved from horizontal seismogram. Although tilt signals retrieved from seismometer generally show poor signal-to-noise ratio compared to tiltmeters, seismometers can be easilly deployed at steep volcanoes in aspects of cost and installation. This means that real-time retrieval of seismic-derived tilt has a potential to be an alternative or complement to tiltmeters and contribute to developing automated alert (early warning) system. Here, as a first step to an early-warning system based on seismic-derived tilt, we design a real-time derivation system of tilt from a seismic signal with four infinite impulse response (IIR) filters based on the procedure of our post-processing used in the data analysis of the 3 July 2019 paroxysm.

We optimize the data processing flow of the seismic-derived tilt (section 3.2.1) for real-time processing. Because permanent tilt station OHO equipped with a Pinnacle 5000T tiltmeter has been used for the early warning system of paroxysmal explosions at Stromboli volcano (Ripepe et al., 2021a[163]), we design the system to reproduce the same instrumental response to the Pinnacle tiltmeter. The tilt record is smoothed by an internal analogue low-pass filter (Sallen-Key type circuit) with a cut-off period of $\sim$30 s and is sampled at 1 sample per second (sps). Because the velocity record of the CMG-40T broad-band seismometer is sampled at 100 sps, we decimate the velocity record from 100 sps to 1 sps. We insert a high-pass filter to reduce the effect of the long-period drift due to the integration of the velocity to calculate the displacement. As the final step, digital low-pass filter equivalent to the analogue Sallen-Key low-pass filter is used to reproduce the frequency response of the Pinnacle instruments. The system thus contains four IIR filters: (i) decimation from 100 sps to 1 sps by averaging over 1 s (100 samples of the last second); (ii) high-pass filtering of 3 h to remove accumulative drift due to integration and diurnal cycle; (iii) trapezoidal integration and multiplying the magnification factor to convert velocity to tilt; (iv) low-pass filtering by the digital Sallen-Key filter (Figure 5.5).

(ii) high-pass filter of 3 h

We applied a 2-pole Butterworth-type high-pass filter with a cut-off period of 3 h to the decimated velocity record with 1 sps. The transfer function of this filter is expressed as the Laplace transform ($s = j\omega$, where ω is the angular frequency):

$$H(s) = \frac{s^2}{\omega_c^2 + \frac{\omega_c}{Q}s + s^2}, \tag{5.10}$$

where ω_c is the cut-off angular frequency and Q is the quality factor. For the Butterworth type, the quality factor Q is determined as $1/\sqrt{2} = 0.707$. The cut-off angular frequency can be calculated as $\omega_c = 2\pi/T_c$, where $T_c = 3$ h is the cut-off period. To design an equivalent digital filter equivalent to the analogue one, we applied the bilinear transform method, which converts the Laplace transform (s) to the z-transform (z):

$$s \to \frac{2}{T}\frac{1 - z^{-1}}{1 + z^{-1}}, \tag{5.11}$$

where $T = 1$ s is the sampling period.

With the input waveform x_i and the output waveform y_i in the i-th step of the time series, this high-pass filter (Eq. 5.10) digitized by (Eq. 5.11) can be expressed as a following difference equation:

$$y_i = \frac{1}{a_0}[b_0 x_i + b_1 x_{i-1} + b_2 x_{i-2} - a_1 y_{i-1} - a_2 y_{i-2}]. \tag{5.12}$$

b_0, b_1, b_2, a_1, a_2 are filter coefficients:

$$\begin{aligned} b_0 &= \frac{4}{T^2} \\ b_1 &= -\frac{8}{T^2} \\ b_2 &= \frac{4}{T^2} \\ a_0 &= \omega_c^2 + \frac{2\omega_c}{QT} + \frac{4}{T^2} \\ a_1 &= 2\omega_c^2 - \frac{8}{T^2} \\ a_2 &= \omega_c^2 + \frac{2\omega_c}{QT} - \frac{4}{T^2}, \end{aligned} \tag{5.13}$$

where $T = 1$ sec is the sampling period, $\omega_c = 2\pi/T_c$ is the cut-off frequency (cut-off period $T_c = 3$ h), $Q = 1/\sqrt{2} \sim 0.707$ is the dampling factor for the Butterworth property.

(iii) integration and magnification filter

We applied a trapezoidal integration filter to the high-passed velocity record (Eq. 3.1). With the input waveform x_i and the output waveform y_i in the i-th step of the time series, trapezoidal integration is expressed as a 1-pole recursive filter:

$$y_i = m(b_0 x_i + b_1 x_{i-1}) - a_1 y_{i-1}, \tag{5.14}$$

where b_0, b_1, a_1 are coefficients of the integration filter and m is the magnification factor.

$$\begin{aligned} b_0 &= \frac{T}{2} \\ b_1 &= \frac{T}{2} \\ a_1 &= -1. \end{aligned} \tag{5.15}$$

$T = 1$ sec is the sampling period, and the magnification factor is calculated as $m = -\omega_0^2/g = (2\pi/T_0)^2 g$, where T_0 is the natural period of the seismometer (30 s or 60 s).

(iv) Sallen-Key type digital low-pass filter

We applied a Sallen-Key type digital low-pass filter to the displacement record. The transfer function of this analogue filter is expressed as the Laplace transform ($s = j\omega$, where ω is the angular frequency):

$$H(s) = \frac{\omega_c^2}{\omega_c^2 + \frac{\omega_c}{Q} s + s^2}, \tag{5.16}$$

where ω_c is the cut-off angular frequency and Q is the quality factor. For the Sallen-Key topology, the quality factor is determined as $1/2 = 0.5$, while $1/\sqrt{2} = 0.707$ for the Butterworth topology (Figure 5.3). The cut-off angular frequency can be calculated as $\omega_c = 1/\sqrt{RC}$, where $R = 10^6$ [Ω] is the resistance and $C = 4.7 \times 10^{-6}$ [F] is the capacitance. We also applied the bilinear transform (Eq. 5.11) to digitize the analogue filter expressed by Eq. (5.16). The reproduced digital filters can be applied by using the equation (5.12) and filter coefficients derived by equation (5.16) and (5.11) with the following filter coefficients:

$$\begin{aligned} b_0 &= \omega_c^2 \\ b_1 &= -2\omega_c^2 \\ b_2 &= \omega_c^2 \\ a_0 &= \omega_c^2 + \frac{2\omega_c}{QT} + \frac{4}{T^2} \\ a_1 &= 2\omega_c^2 - \frac{8}{T^2} \\ a_2 &= \omega_c^2 + \frac{2\omega_c}{QT} - \frac{4}{T^2}, \end{aligned} \tag{5.17}$$

where $T = 1$ s is the sampling period, $\omega_c = 2\pi/T_c$ is the cut-off frequency (cut-off period $T_c = 1/\sqrt{RC} \sim 29.53$ s), $Q = 1/2 = 0.5$ is the damping factor.

The series of filtering procedures is written in Matlab software. We confirmed the validity of the digital filter by applying it to a simulated time series (86400 samples) of white noise produced as the Gaussian distribution with a mean of zero and a standard deviation of 1 (Figure 5.4). The amplitude spectra of the unfiltered noise signal and the digital-filtered signal show the reliability of the digital filter (Figure 5.4b). We validate the filter's performance using our seismic stations equipped with CMG-40T broadband seismometer with a natural period of 30 s deployed at ∼30 cm depth. Figure 5.5 shows an example of real-time running of the filtering system. We used the EW component of the seismic station RND, which is installed at the same location as the tilt station OHO. Seismic data sampled at Stromboli is once stored in an online data server and then downloaded to a machine at the University of Florence. Figure 5.5a shows waveforms of each step: decimated velocity (1 sps), high-pass filtered velocity, displacement, tilt and low-passed tilt. Since we designed the IIR filters, the series of filtering can be performed very fast less than a second. Real-time running of the filter generally returns tilt signals with ∼20 s delay from the actual clock, which includes data transmission from the seismic station at Stromboli to the online data server, data download from the server to the machine in the laboratory in Florence, and visualization of the retrieved tilt signals on display. Because the final inflation before paroxysms starts ∼10 min before the onset and can be automatically identified about 5 min before by the early warning system currently in operation at Stromboli (Ripepe et al., 2021[163]), the filtering method is fast enough to be implemented in a future early warning system. The seismic-derived tilt from RND is compared to the real-time tilt record from OHO (Figure 5.5b). The noise level of the seismic-derived tilt is comparable to the amplitude of the inflation-deflation cycles, which consequently indicates a smaller signal-to-noise ratio than the borehole tiltmeter OHO. We also apply this filtering system to the EW component of STR before the 3 July 2019 paroxysm (Figure 5.6). The final ground inflation ∼10 min before (Figure 5.6a) and the preceding phase ∼1 h before (Figure 5.6b) reported in Ripepe et al. (2021a[163]) and this study are well reproduced by the filtering system. We suggest that real-time conversion of seismic-derived tilt may be a possible option for monitoring ground deformation because of its lower installation cost. Further, validation of the filtering system using more long-term data and implementation of the existing early warning system (Ripepe et al., 2021a[163])

will be the subject of future studies.

5.4 Future perspectives

This study proposed a basic model of shallow magma plumbing system and ground deformation model of Stromboli volcano based on data analyses of different-type eruptions. However, we focused on limited period or events of eruptions: ordinary explosions from June to August 2014, the 3 July paroxysm, and the 7 August lava effusion. Further analyses of ordinary explosions in other period (from 2004 to present), paroxysms (2002, 2007 and 2019 August) and lava effusion (2002 and 2007) using tilt and seismic data recorded by the permanent monitoring network will improve the understanding of stability and variation of the pressure source at the shallow system. Also, although tilt data of the three temporary stations in 2014 provided important data to constrain the pressure source of ordinary explosion, it is still necessary to improve station coverage to resolve the source parameters more. Near-vent temporary observation using platform tiltmeters or seismometers, for example, very-near-field ($\sim$100 m) seismic observation (Sugimura et al., 2021[185]) will contribute to constrain the horizontal location and shape of the pressure source. In addition, analyses of tilt, seismic and strain data recorded by permanent stations of the INGV located at lower elevation is important to develop more general ground deformation model of Stromboli volcano.

In this study, we applied a method to classify stages of tilt signals associated with ordinary explosions, which requires ad-hoc thresholds on tilt amplitude and duration. For long-term data analyses and real-time extraction of tilt signals and their classification, it is better to develop a more robust method that accurately identify tilt stages, for example, machine learning algorithms. Also, we used classic grid-searching for estimation of volcanic pressure source. However, based on this method, it is difficult to quantitatively evaluate uncertanties of model parameters. An inversion of ground deformation data based on Bayesian framework, for example, Markov-Chain Monte Carlo (MCMC) method (e.g. Anderson and Segall, 2013[11]) can be useful to evaluate the parameter uncertainties. Besides, it is necessary to increase calculation speed of a forward model using a finite element method for efficient performance of inversions based on the Monte Carlo approach. Because bottom-neck of calculation of a finite element method is the mesh generation, development of more effective meshing algorithm is important, for example, an algorithm

that only regenerate mesh around the pressure source and preserve mesh in the other part generated for previous forward model.

Ripepe et al. (2021a)[163] showed the self-similarity of ground inflation trend before ordinary explosion and paroxysm, which suggests the existence of a common conduit dynamics. If we assume that both ordinary explosion and paroxysm share the similar pressure source (shallow magma reservoir), which is suggested by this study, the self-similar trend can be explained by a smilar physical process of magma ascent in the feeding conduit towards the shallow magma reservoir, with different time scale (ordinary explosion: $\sim$200 s; paroxysm: 600 s) and different magnitude of pressurization (= different tilt amplitude) at the top of the feeding conduit (ordinary explosion: 2.6 kPa; paroxysm: 3.9 MPa). This difference of the pressurization rate in the shallow magma reservoir probably cause the difference of the main magma migration process in the open conduit above the shallow magma reservoir (ordinary explosion: magma-static height increase; paroxysm: viscous flow). Our conceptual model describes gradual inflation before ordinary explosion as a regular gas and melt supply and final inflation before paroxysm as a fast ascent of deep-originated LP magma. These gas-magma ascent processes are controlled by fluid dynamical processes, for example, dynamics of gas bubbles and magma mixture (Nishimura, 2009[137]; Kawaguchi and Nishimura, 2015[102]) and interaction with highly viscous magma in the upper conduit (Barth et al., 2019[22]; Oppenheimer et al., 2020[144]). Based on our conceptual model of Stromboli's magma plumbing system and shallow magma reservoir dynamics, further studies of numerical simulation of conduit flow or analogue experiment of gas bubble ascent will lead to quantitatively infer dynamics of magma ascent associated with the eruptions at Stromboli volcano.

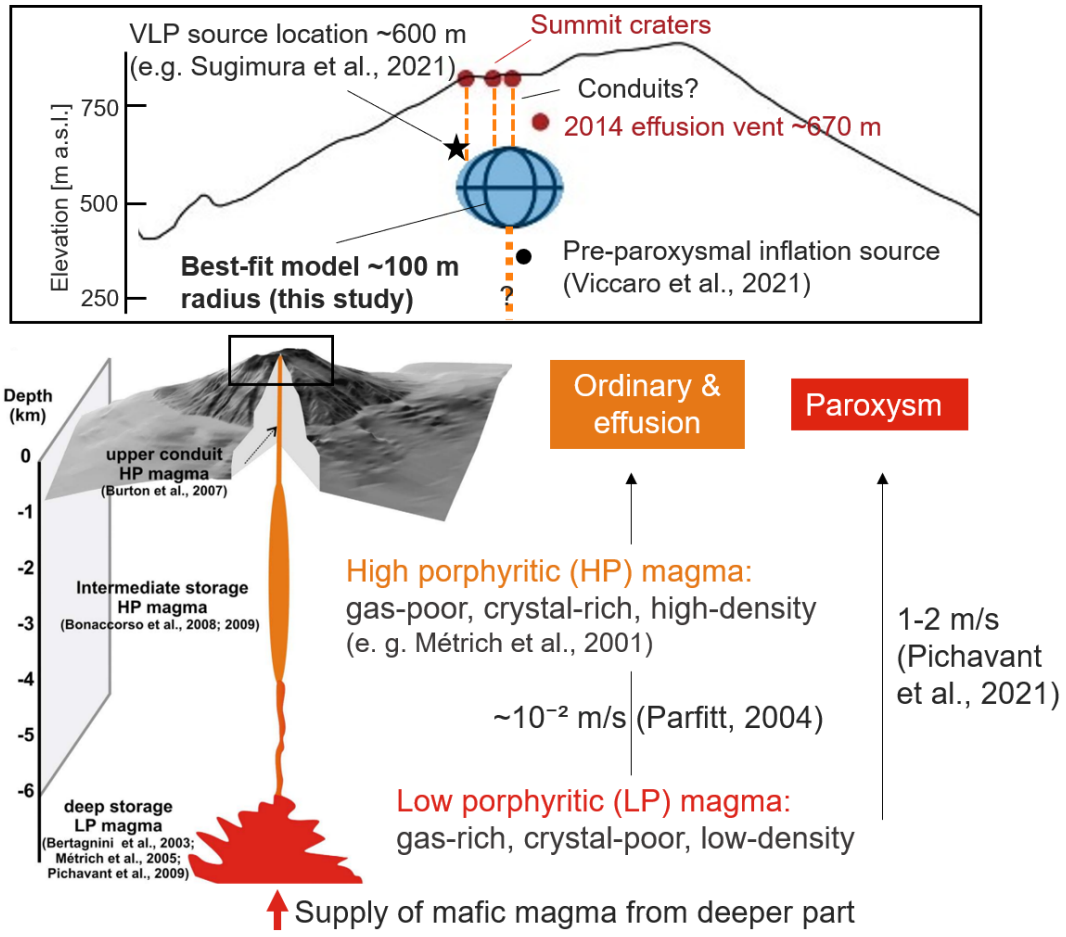

Figure 5.1: Schematic illustration of the deep and shallow magma plumbing system of Stromboli volcano.

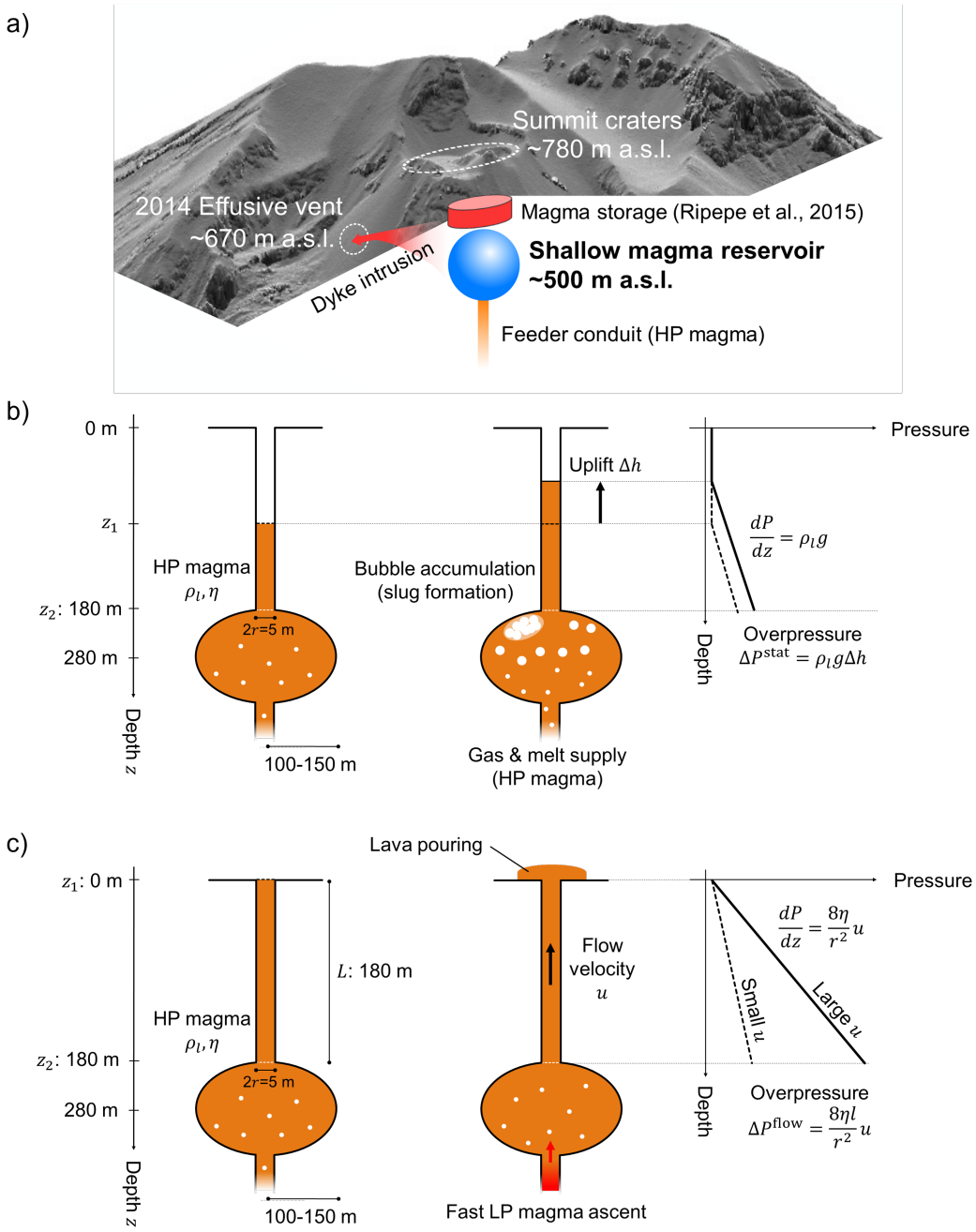

Figure 5.2: Schematic models of the shallow conduit-reservoir system and pressurization process of explosive eruptions at Stromboli. (a) The shallow magma plumbing system of Stromboli. The estimated pressure source (shallow reservoir; blue sphere) with ∼100 m radii is located at ∼500 m a.s.l. beneath the summit craters at ∼780 m a.s.l. (b, c) Mechanical model of pressurization process of the shallow magma reservoir with an opened conduit-reservoir system. (b) Pressurization process of gradual inflation before the ordinary explosion. Magma supply (gas ascent) into the shallow reservoir generates the uplift of the magma free surface in the eruptive conduit (∼2.5 m radius) and the gradual inflation (stage A) starting ∼200 s before the onset of an explosion. (c) Pressurization process of final inflation before the paroxysmal explosion. Although a fast ascent of gas-rich (LP) magma drives magma flow in the conduit and enlarges the pressurization, the same part of the shallow reservoir acts as a pressure source.

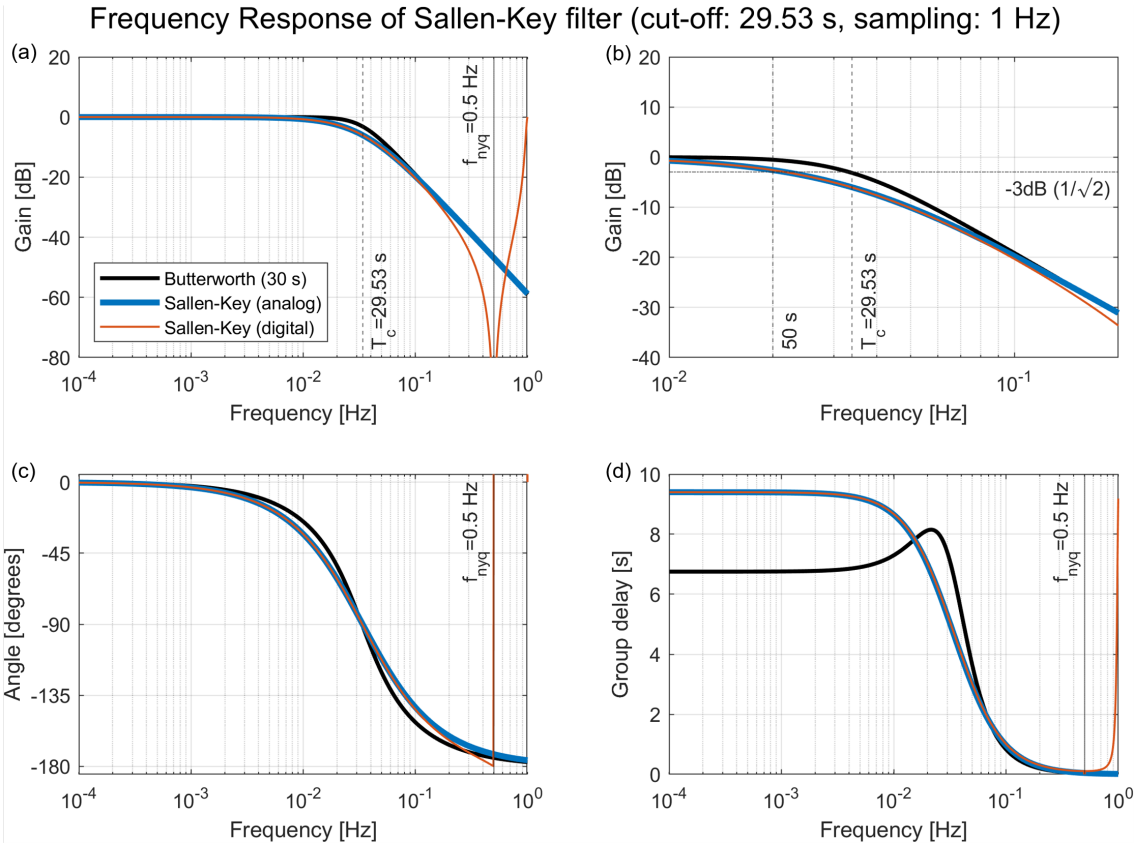

Figure 5.3: Frequency response of Sallen-Key filter (cut-off period of ∼30 s). (a) Amplitude. (b) Zoom up of (a) around the cut-off period. (c) Angle. (d) Group delay. Analog Sallen-Key filter (blue line), analogue 2-pole and 30 s-cutoff Butterworth filter (black line), digital Sallen-Key filter bilinear transform (orange line).

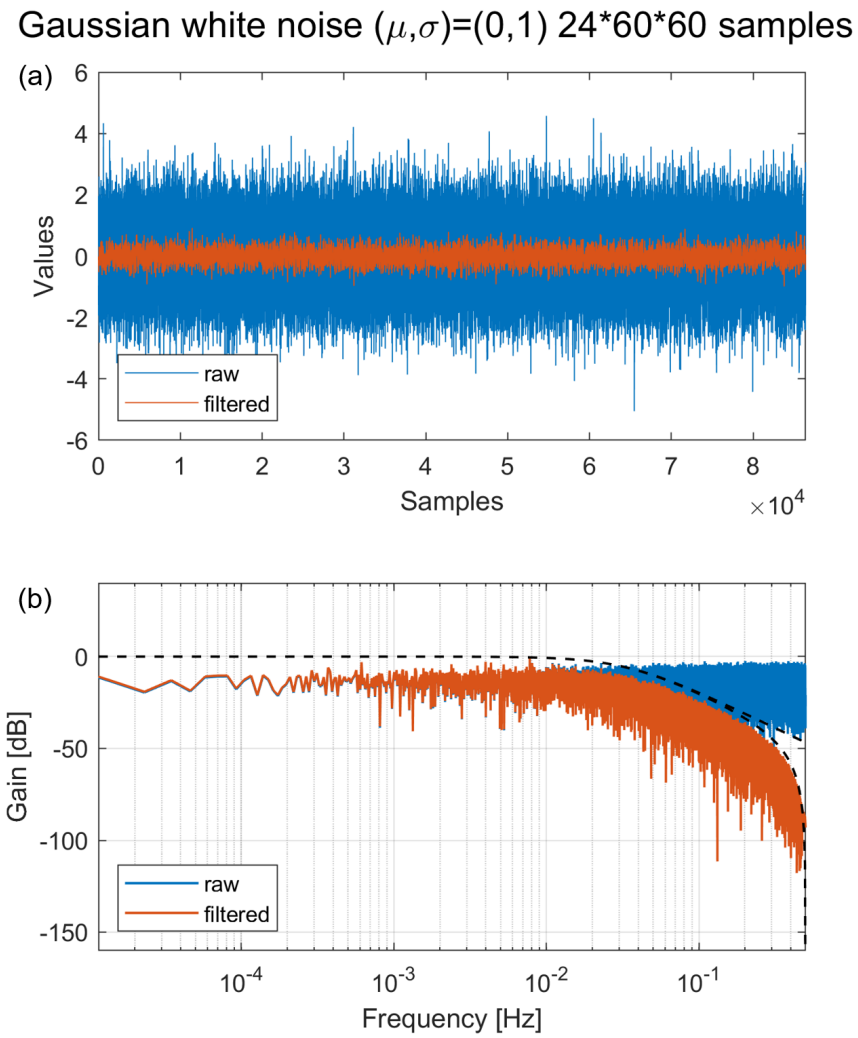

Figure 5.4: Application of the digital Sallen-Key filters to the time series of gaussian white noise. (a) Time series. (b) Amplitude spectrum.

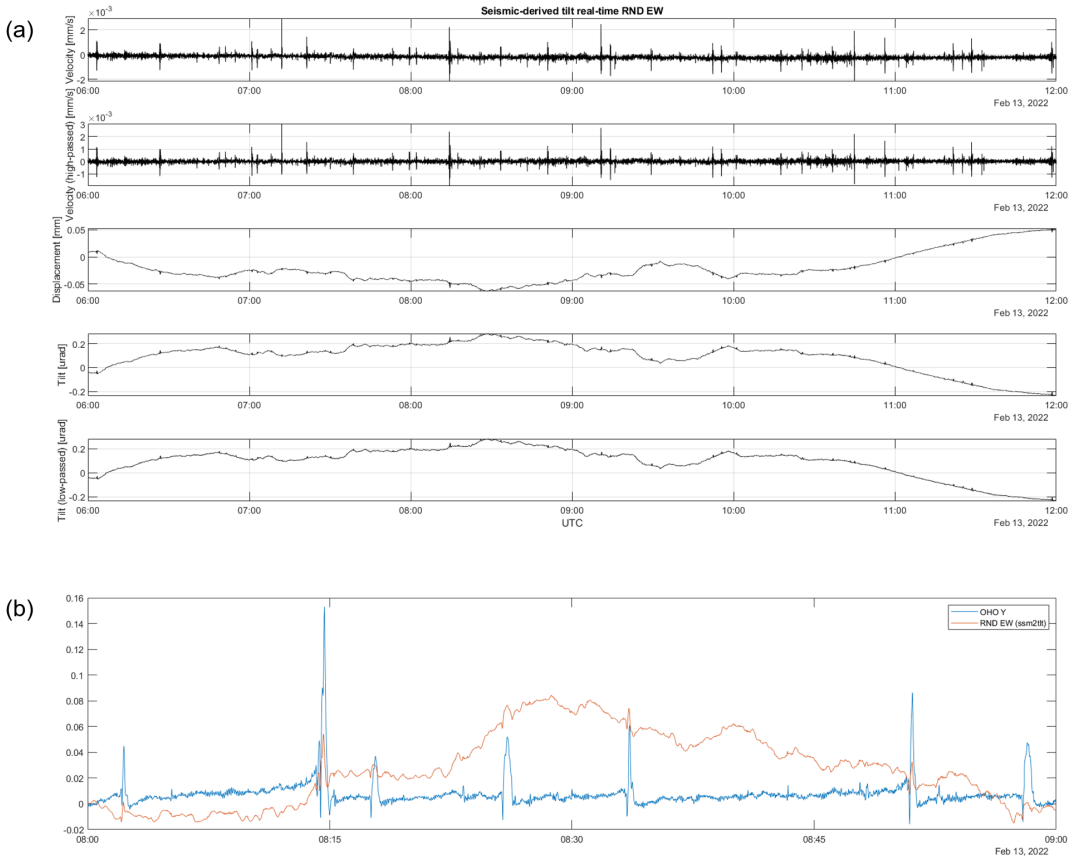

Figure 5.5: Real-time running of the tilt retrieval system from broad-band seismometer RND (EW component), which is co-located at the borehole tiltmeter OHO. (a) Plots of original velocity signal to final tilt signal. (b) Comparison of RND (seismometer) with OHO (tiltmeter).

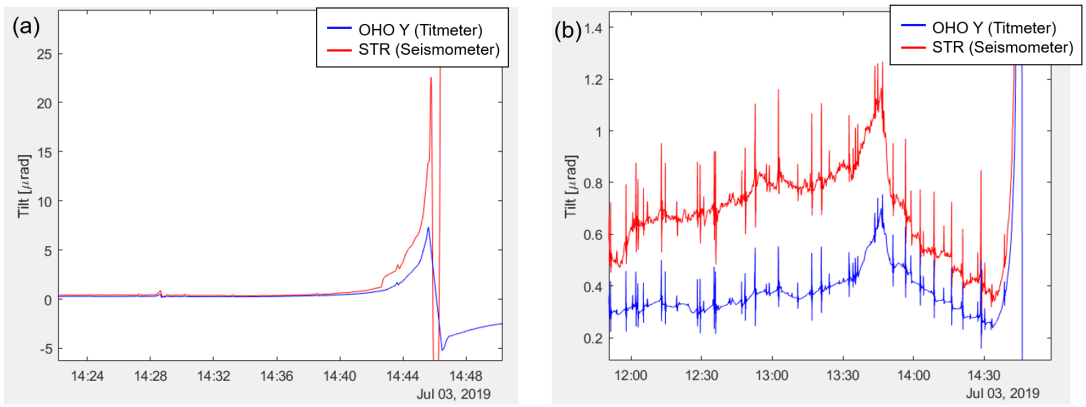

Figure 5.6: Application of the real-time tilt retrieval system to the ground deformation before the 3 July paroxysm. Broad-band seismometer STR (red) and Borehole tiltmeter OHO (blue). (a) Final inflation (−10 minutes) and (b) preceding phase (−1 hour)

Chapter 6

Conclusions

In this thesis, we have investigated the ground deformations associated with the different-type eruptions at Stromboli volcano: ordinary explosion, paroxysm and lava effusion. To update the understanding of the volcanic pressure source at the shallow magma plumbing system and the mechanical process of pre-eruptive magma transport, we analyzed ground tilt signals and estimated the volcanic pressure source.

First, we analyzed tilt signals recorded by permanent tilt and seismic stations operated by the LGS-UNIFI and temporary tilt stations deployed near the summit eruptive craters during 2014 to understand the characteristics of the ground deformation fields for each eruption type. We obtained the following main results:

1. We classified the ground tilt cycle of ordinary explosions into four stages: gradual inflation (stage A) prior to an explosion lasting ∼200 s, rapid inflation (stage B) lasting for ∼15 s followed by the explosion onset, rapid deflation (stage C) lasting for ∼30 s and recovery process (stage D). The observed tilt vectors direct towards the summit craters, excepting several stations with misorientation up to ∼30 degrees.

2. Tilt motions of ground deflation associated with the 7 August 2014 lava effusion were similar to that of the ordinary explosion. Only one station close (∼200 m) to the newly opened effusive vent at the mountain flank showed a difference in tilt direction of about 30 degrees, which is interpreted to be the effect of a local dyke that intruded from the main magma system to the flank effusive vent.

3. Tilt vectors calculated from the final inflation stating 10 min before the onset of the paroxysm were directed towards the summit craters. At the two stations commonly used for the analysis of ordinary explosions, tilt vectors were very similar, which

suggests the similarity of a volcanic pressure source generating ordinary explosion and paroxysm.

To estimate the volcanic pressure source inducing the observed ground deformations, we inverted the observed tilt vectors derived by our data analyses, applying grid-search-based inversions with spherical or ellipsoidal source shapes. Theoretical ground tilt is calculated by a finite element method (FEM) to take the effect of topography into account. The main results obtained from the inversions are summarized as follows:

1. We independently estimated the best-fit location of a spherical source with a radius of 100 m for each eruption type. The best-fit locations for ordinary explosion and paroxysm were estimated at the same horizontal location beneath the summit craters and almost the same elevation at 500–550 m a.s.l. The best-fit model for lava effusion was located horizontally ∼150 m from the central crater and at 450 m a.s.l. These results suggest that the pressure source of these eruptions is commonly located at a range of shallow (<∼400 m depth, >400 m a.s.l.) portion of magma plumbing system beneath the summit crater area, although the independent inversions returned different locations of best-fit models.

2. Joint inversions combining ordinary explosion and paroxysm returned the best-fit model of an ellipsoidal source with the same centroid as the ordinary explosion and nearly-spherical shape ($100 \times 150 \times 100$ m). However, the trade-off between the source volume and the pressure change exists.

3. The best-fit model of the joint inversion with an ellipsoidal source can also reproduce the observed ground deflation associated with the lava effusion.

We showed that the geometry of the best-fit ellipsoid and subsidence of the summit craters agree with an analogue experiment of caldera formation, as well as the effusion-induced depressurization (-1.2 MPa) corresponds with the magma volume drained during the lava effusion (1.6×10^6 m^6), which supports the robustness of the best-fit model parameters. We interpret the estimated pressure source as a shallow magma reservoir composed of high porphyritic (HP) magma mush. We compared the estimated pressure change to the volume of magma discharge or the upward velocity of magma motion in the conduit through a mechanical model of magma movement in the opened conduit-reservoir system to understand the pressurization processes of the source. Gradual inflation before

ordinary explosion is explained by the magma-static pressure change of the conduit above the reservoir in response to ordinary gas and melt supply, whereas that of paroxysm reflects the pressure gradient driving the viscous magma flow in the conduit induced by the rapid ascent of low porphyritic (LP) magma.

We succeeded in showing the similarity and difference in an aspect of volcanic pressure source among the different-type eruptions at Stromboli volcano, from the analyses of data obtained by the near-vent tilt stations. We found that, in spite of different magma properties and eruptive intensity involved, ground deformations induced by different-type eruptions (ordinary explosion, paroxysm and lava effusion) are caused by the common pressure source in the shallow depth beneath the vent. We also showed the difference between ordinary explosion and paroxysm in the mechanical processes of source pressurization. Monitoring and long-term data analysis of ground deformations associated with volcanic eruptions supported by near-vent geophysical observation networks will contribute to understanding the dynamics of volcanic eruptions and forecasting changes in volcanic activities.

References

[1] D. C. Agnew. Strainmeters and tiltmeters. *Reviews of Geophysics*, 24(3):579–624, 1986.

[2] A. Aiuppa, A. Bertagnini, N. Métrich, R. Moretti, A. Di Muro, M. Liuzzo, and G. Tamburello. A model of degassing for Stromboli volcano. *Earth and Planetary Science Letters*, 295(1-2):195–204, 2010.

[3] A. Aiuppa, M. Bitetto, D. Delle Donne, F. P. La Monica, G. Tamburello, D. Coppola, M. Della Schiava, L. Innocenti, G. Lacanna, M. Laiolo, et al. Volcanic CO2 tracks the incubation period of basaltic paroxysms. *Science Advances*, 7(38):eabh0191, 2021.

[4] F. Albino, F. Amelung, and P. Gregg. The role of pore fluid pressure on the failure of magma reservoirs: insights from Indonesian and Aleutian arc volcanoes. *Journal of Geophysical Research: Solid Earth*, 123(2):1328–1349, 2018.

[5] F. Albino, J. Biggs, and D. K. Syahbana. Dyke intrusion between neighbouring arc volcanoes responsible for 2017 pre-eruptive seismic swarm at Agung. *Nature Communications*, 10(1):1–11, 2019.

[6] F. Albino, V. Pinel, H. Massol, and M. Collombet. Conditions for detection of ground deformation induced by conduit flow and evolution. *Journal of Geophysical Research: Solid Earth*, 116(B6), 2011.

[7] A. Amoruso and L. Crescentini. Analytical models of volcanic ellipsoidal expansion sources. *Annals of Geophysics*, 56(4):S0435–S0435, 2013.

[8] A. N. Anderson, J. H. Foster, and N. Frazer. Implications of deflation-inflation event models on Kīlauea Volcano, Hawaii. *Journal of Volcanology and Geothermal Research*, 397:106832, 2020.

[9] K. Anderson, M. Lisowski, and P. Segall. Cyclic ground tilt associated with the 2004–2008 eruption of Mount St. Helens. *Journal of Geophysical Research: Solid Earth*, 115(B11), 2010.

[10] K. Anderson and P. Segall. Physics-based models of ground deformation and extrusion rate at effusively erupting volcanoes. *Journal of Geophysical Research: Solid Earth*, 116(B7), 2011.

[11] K. Anderson and P. Segall. Bayesian inversion of data from effusive volcanic eruptions using physics-based models: Application to Mount St. Helens 2004–2008. *Journal of Geophysical Research: Solid Earth*, 118(5):2017–2037, 2013.

[12] K. R. Anderson, I. A. Johanson, M. R. Patrick, M. Gu, P. Segall, M. P. Poland, E. K. Montgomery-Brown, and A. Miklius. Magma reservoir failure and the onset of caldera collapse at Kīlauea Volcano in 2018. *Science*, 366(6470):eaaz1822, 2019.

[13] K. R. Anderson and M. P. Poland. Bayesian estimation of magma supply, storage, and eruption rates using a multiphysical volcano model: Kīlauea Volcano, 2000–2012. *Earth and Planetary Science Letters*, 447:161–171, 2016.

[14] K. R. Anderson, M. P. Poland, J. H. Johnson, and A. Miklius. Episodic deflation-inflation events at Kīlauea Volcano and implications for the shallow magma system. *Hawaiian Volcanoes: From Source to Surface*, 208:229, 2015.

[15] D. Andronico, E. Del Bello, C. D ' Oriano, P. Landi, F. Pardini, P. Scarlato, J. Taddeucci, A. Cristaldi, F. Ciancitto, F. Pennacchia, et al. Uncovering the eruptive patterns of the 2019 double paroxysm eruption crisis of Stromboli volcano. *Nature Communications*, 12(1):1–14, 2021.

[16] H. Aoyama and H. Oshima. Tilt change recorded by broadband seismometer prior to small phreatic explosion of Meakan-dake volcano, Hokkaido, Japan. *Geophysical Research Letters*, 35(6), 2008.

[17] H. Aoyama and H. Oshima. Precursory tilt changes of small phreatic eruptions of Meakan-dake volcano, Hokkaido, Japan, in November 2008. *Earth, Planets and Space*, 67(1):1–13, 2015.

[18] F. Arens, A. Coco, J. Gottsmann, J. Hickey, and G. Kilgour. Multiphysics modeling of volcanic unrest at Mt. Ruapehu (New Zealand). *Geochemistry, Geophysics, Geosystems*, page e2022GC010572, 2022.

[19] E. Auger, L. D'Auria, M. Martini, B. Chouet, and P. Dawson. Real-time monitoring and massive inversion of source parameters of very long period seismic signals: An application to Stromboli Volcano, Italy. *Geophysical Research Letters*, 33(4), 2006.

[20] F. Barberi. Volcanic hazard assessment at Stromboli based on review of historical data. *Acta Vulcanologica*, 3:173–187, 1993.

[21] F. Barberi, L. Civetta, M. Rosi, and R. Scandone. Chronology of the 2007 eruption of Stromboli and the activity of the Scientific Synthesis Group. *Journal of Volcanology and Geothermal Research*, 182(3-4):123–130, 2009.

[22] A. Barth, M. Edmonds, and A. Woods. Valve-like dynamics of gas flow through a packed crystal mush and cyclic strombolian explosions. *Scientific Reports*, 9(1):1–9, 2019.

[23] M. G. Bato, V. Pinel, Y. Yan, F. Jouanne, and J. Vandemeulebrouck. Possible deep connection between volcanic systems evidenced by sequential assimilation of geodetic data. *Scientific Reports*, 8(1):1–13, 2018.

[24] J. Battaglia, K. Aki, and J.-P. Montagner. Tilt signals derived from a GEOSCOPE VBB station on the Piton de la Fournaise volcano. *Geophysical Research Letters*, 27(5):605–608, 2000.

[25] F. Beauducel and F. H. Cornet. Collection and three-dimensional modeling of GPS and tilt data at Merapi volcano, Java. *Journal of Geophysical Research: Solid Earth*, 104(B1):725–736, 1999.

[26] J. Berger. A note on thermoelastic strains and tilts. *Journal of Geophysical Research*, 80(2):274–277, 1975.

[27] A. Bevilacqua, A. Bertagnini, M. Pompilio, P. Landi, P. Del Carlo, A. Di Roberto, W. Aspinall, and A. Neri. Major explosions and paroxysms at Stromboli (Italy): A new historical catalog and temporal models of occurrence with uncertainty quantification. *Scientific Reports*, 10(1):1–18, 2020.

[28] J. Biggs, S. Ebmeier, W. Aspinall, Z. Lu, M. Pritchard, R. Sparks, and T. Mather. Global link between deformation and volcanic eruption quantified by satellite imagery. *Nature Communications*, 5(1):1–7, 2014.

[29] J. Biggs and M. E. Pritchard. Global volcano monitoring: what does it mean when volcanoes deform? *Elements*, 13(1):17–22, 2017.

[30] E. Blackburn, L. Wilson, and R. J. Sparks. Mechanisms and dynamics of strombolian activity. *Journal of the Geological Society*, 132(4):429–440, 1976.

[31] M. Bombrun, A. Harris, L. Gurioli, J. Battaglia, and V. Barra. Anatomy of a Strombolian eruption: Inferences from particle data recorded with thermal video. *Journal of Geophysical Research: Solid Earth*, 120(4):2367–2387, 2015.

[32] A. Bonaccorso. Evidence of a dyke-sheet intrusion at Stromboli Volcano Inferred through continuous tilt. *Geophysical Research Letters*, 25(22):4225–4228, 1998.

[33] A. Bonaccorso. Explosive activity at Mt. Etna summit craters and source modeling by using high-precision continuous tilt. *Journal of Volcanology and Geothermal Research*, 158(3-4):221–234, 2006.

[34] A. Bonaccorso, A. Bonforte, S. Gambino, M. Mattia, F. Guglielmino, G. Puglisi, and E. Boschi. Insight on recent Stromboli eruption inferred from terrestrial and satellite ground deformation measurements. *Journal of Volcanology and Geothermal Research*, 182(3-4):172–181, 2009.

[35] A. Bonaccorso, S. Calvari, A. Linde, S. Sacks, and E. Boschi. Dynamics of the shallow plumbing system investigated from borehole strainmeters and cameras during the 15 March, 2007 Vulcanian paroxysm at Stromboli volcano. *Earth and Planetary Science Letters*, 357:249–256, 2012.

[36] A. Bonaccorso, S. Cianetti, C. Giunchi, E. Trasatti, M. Bonafede, and E. Boschi. Analytical and 3-D numerical modelling of Mt. Etna (Italy) volcano inflation. *Geophysical Journal International*, 163(2):852–862, 2005.

[37] A. Bonaccorso and P. M. Davis. Models of ground deformation from vertical volcanic conduits with application to eruptions of Mount St. Helens and Mount Etna. *Journal of Geophysical Research: Solid Earth*, 104(B5):10531–10542, 1999.

[38] A. Bonaccorso, G. Falzone, and S. Gambino. An investigation into shallow borehole tiltmeters. *Geophysical Research Letters*, 26(11):1637–1640, 1999.

[39] A. Bonaccorso, S. Gambino, F. Guglielmino, M. Mattia, G. Puglisi, and E. Boschi. Stromboli 2007 eruption: Deflation modeling to infer shallow-intermediate plumbing system. *Geophysical Research Letters*, 35(6), 2008.

[40] M. Burton, P. Allard, F. Muré, and A. La Spina. Magmatic gas composition reveals the source depth of slug-driven Strombolian explosive activity. *Science*, 317(5835):227–230, 2007.

[41] M. Burton, S. Calvari, L. Spampinato, L. Lodato, N. Pino, E. Marchetti, and F. Murè. Volcanic and seismic activity at Stromboli preceding the 2002-03 eruption. In *THE STROMBOLI VOLCANO: An integrated study of the 2002-2003 Eruption*. American Geophysical Union, 2008.

[42] S. Calvari, L. Spampinato, A. Bonaccorso, C. Oppenheimer, E. Rivalta, and E. Boschi. Lava effusion—A slow fuse for paroxysms at Stromboli volcano? *Earth and Planetary Science Letters*, 301(1-2):317–323, 2011.

[43] S. Calvari, L. Spampinato, and L. Lodato. The 5 April 2003 vulcanian paroxysmal explosion at Stromboli volcano (Italy) from field observations and thermal data. *Journal of Volcanology and Geothermal Research*, 149(1-2):160–175, 2006.

[44] A. Capponi, S. J. Lane, and M. R. James. The implications of gas slug ascent in a stratified magma for acoustic and ground deformation source mechanisms in Strombolian eruptions. *Earth and Planetary Science Letters*, 468:101–111, 2017.

[45] A. Capponi, J. Taddeucci, P. Scarlato, and D. M. Palladino. Recycled ejecta modulating Strombolian explosions. *Bulletin of Volcanology*, 78(2):1–13, 2016.

[46] N. Casagli, A. Tibaldi, A. Merri, C. Del Ventisette, T. Apuani, L. Guerri, J. Fortuny-Guasch, and D. Tarchi. Deformation of Stromboli Volcano (Italy) during the 2007 eruption revealed by radar interferometry, numerical modelling and structural geological field data. *Journal of Volcanology and Geothermal Research*, 182(3-4):182–200, 2009.

[47] V. Cayol and F. Cornet. 3D mixed boundary elements for elastostatic deformation field analysis. *International Journal of Rock Mechanics and Mining Sciences*, 34(2):275–287, 1997.

[48] V. Cayol and F. H. Cornet. Effects of topography on the interpretation of the deformation field of prominent volcanoes—Application to Etna. *Geophysical Research Letters*, 25(11):1979–1982, 1998.

[49] S. Cesca, T. Braun, E. Tessmer, and T. Dahm. Modelling of the April 5, 2003, Stromboli (Italy) paroxysmal eruption from the inversion of broadband seismic data. *Earth and Planetary Science Letters*, 261(1-2):164–178, 2007.

[50] B. Chouet, P. Dawson, and M. Martini. Upper conduit structure and explosion dynamics at Stromboli. *Washington DC American Geophysical Union Geophysical Monograph Series*, 182:81–92, 2008.

[51] B. Chouet, P. Dawson, T. Ohminato, M. Martini, G. Saccorotti, F. Giudicepietro, G. De Luca, G. Milana, and R. Scarpa. Source mechanisms of explosions at Stromboli Volcano, Italy, determined from moment-tensor inversions of very-long-period data. *Journal of Geophysical Research: Solid Earth*, 108(B1):ESE–7, 2003.

[52] B. Chouet, N. Hamisevicz, and T. R. McGetchin. Photoballistics of volcanic jet activity at Stromboli, Italy. *Journal of Geophysical Research*, 79(32):4961–4976, 1974.

[53] A. B. Clarke, T. E. Ongaro, and A. Belousov. Vulcanian eruptions. In *The Encyclopedia of Volcanoes*, pages 505–518. Elsevier, 2015.

[54] D. Coppola, M. Ripepe, M. Laiolo, and C. Cigolini. Modelling satellite-derived magma discharge to explain caldera collapse. *Geology*, 45(6):523–526, 2017.

[55] G. Currenti, C. Del Negro, and G. Ganci. Modelling of ground deformation and gravity fields using finite element method: an application to Etna volcano. *Geophysical Journal International*, 169(2):775–786, 2007.

[56] G. Currenti, C. Del Negro, and G. Ganci. Finite element modeling of ground deformation and gravity field at Mt. Etna. *Annals of Geophysics*, 2008.

[57] L. D'Auria, F. Giudicepietro, M. Martini, and R. Peluso. Seismological insight into the kinematics of the 5 April 2003 vulcanian explosion at Stromboli volcano (southern Italy). *Geophysical Research Letters*, 33(8), 2006.

[58] P. M. Davis. Surface deformation due to inflation of an arbitrarily oriented triaxial ellipsoidal cavity in an elastic half-space, with reference to Kilauea volcano, Hawaii. *Journal of Geophysical Research: Solid Earth*, 91(B7):7429–7438, 1986.

[59] D. Delle Donne and M. Ripepe. High-frame rate thermal imagery of Strombolian explosions: Implications for explosive and infrasonic source dynamics. *Journal of Geophysical Research: Solid Earth*, 117(B9), 2012.

[60] B. Di Lieto, P. Romano, R. Scarpa, and A. T. Linde. Strain signals before and during paroxysmal activity at Stromboli volcano, Italy. *Geophysical Research Letters*, 47(21):e2020GL088521, 2020.

[61] F. Di Traglia, T. Nolesini, E. Intrieri, F. Mugnai, D. Leva, M. Rosi, and N. Casagli. Review of ten years of volcano deformations recorded by the ground-based InSAR monitoring system at Stromboli volcano: a tool to mitigate volcano flank dynamics and intense volcanic activity. *Earth-Science Reviews*, 139:317–335, 2014.

[62] M. Dragoni and C. Magnanensi. Displacement and stress produced by a pressurized, spherical magma chamber, surrounded by a viscoelastic shell. *Physics of the Earth and Planetary Interiors*, 56(3-4):316–328, 1989.

[63] Q. Dumont, V. Cayol, J.-L. Froger, and A. Peltier. 22 years of satellite imagery reveal a major destabilization structure at Piton de la Fournaise. *Nature Communications*, 13(1):1–11, 2022.

[64] D. Dzurisin and Z. Lu. Interferometric synthetic-aperture radar (InSAR). In *Volcano deformation*, pages 153–194. Springer, 2007.

[65] J. D. Eshelby. The determination of the elastic field of an ellipsoidal inclusion, and related problems. *Proceedings of the royal society of London. Series A. Mathematical and physical sciences*, 241(1226):376–396, 1957.

[66] J. Fernández, A. Pepe, M. P. Poland, and F. Sigmundsson. Volcano Geodesy: Recent developments and future challenges. *Journal of Volcanology and Geothermal Research*, 344:1–12, 2017.

[67] Y. Fialko, Y. Khazan, and M. Simons. Deformation due to a pressurized horizontal circular crack in an elastic half-space, with applications to volcano geodesy. *Geophysical Journal International*, 146(1):181–190, 2001.

[68] A. Finizola, F. Sortino, J.-F. Lénat, and M. Valenza. Fluid circulation at Stromboli volcano (Aeolian Islands, Italy) from self-potential and CO2 surveys. *Journal of Volcanology and Geothermal Research*, 116(1-2):1–18, 2002.

[69] F. R. Fontaine, G. Roult, L. Michon, G. Barruol, and A. D. Muro. The 2007 eruptions and caldera collapse of the Piton de la Fournaise volcano (La Réunion Island) from tilt analysis at a single very broadband seismic station. *Geophysical Research Letters*, 41(8):2803–2811, 2014.

[70] L. Francalanci, S. Tommasini, and S. Conticelli. The volcanic activity of Stromboli in the 1906–1998 AD period: mineralogical, geochemical and isotope data relevant to the understanding of the plumbing system. *Journal of Volcanology and Geothermal Research*, 131(1-2):179–211, 2004.

[71] J. T. Freymueller, J. B. Murray, H. Rymer, and C. A. Locke. Ground deformation, gravity, and magnetics. In *The Encyclopedia of Volcanoes*, pages 1101–1123. Elsevier, 2015.

[72] Y. Fukushima, V. Cayol, and P. Durand. Finding realistic dike models from interferometric synthetic aperture radar data: The February 2000 eruption at Piton de la Fournaise. *Journal of Geophysical Research: Solid Earth*, 110(B3), 2005.

[73] Y. Fukushima, V. Cayol, P. Durand, and D. Massonnet. Evolution of magma conduits during the 1998–2000 eruptions of Piton de la Fournaise volcano, Réunion Island. *Journal of Geophysical Research: Solid Earth*, 115(B10), 2010.

[74] D. Gaudin, J. Taddeucci, P. Scarlato, A. Harris, M. Bombrun, E. Del Bello, and T. Ricci. Characteristics of puffing activity revealed by ground-based, thermal infrared imaging: the example of Stromboli Volcano (Italy). *Bulletin of Volcanology*, 79(3):1–15, 2017.

[75] D. Gaudin, J. Taddeucci, P. Scarlato, M. Moroni, C. Freda, M. Gaeta, and D. M. Palladino. Pyroclast Tracking Velocimetry illuminates bomb ejection and explosion

dynamics at Stromboli (Italy) and Yasur (Vanuatu) volcanoes. *Journal of Geophysical Research: Solid Earth*, 119(7):5384–5397, 2014.

[76] R. Genco and M. Ripepe. Inflation-deflation cycles revealed by tilt and seismic records at Stromboli volcano. *Geophysical Research Letters*, 37(12), 2010.

[77] G. Giordano and G. De Astis. The summer 2019 basaltic Vulcanian eruptions (paroxysms) of Stromboli. *Bulletin of Volcanology*, 83(1):1–27, 2021.

[78] F. Giudicepietro, L. D'Auria, M. Martini, T. Caputo, R. Peluso, W. De Cesare, M. Orazi, and G. Scarpato. Changes in the VLP seismic source during the 2007 Stromboli eruption. *Journal of Volcanology and Geothermal Research*, 182(3-4):162–171, 2009.

[79] F. Giudicepietro, C. López, G. Macedonio, S. Alparone, F. Bianco, S. Calvari, W. De Cesare, D. Delle Donne, B. Di Lieto, A. M. Esposito, et al. Geophysical precursors of the July-August 2019 paroxysmal eruptive phase and their implications for Stromboli volcano (Italy) monitoring. *Scientific Reports*, 10(1):1–16, 2020.

[80] J. Gottsmann, M. Flynn, and J. Hickey. The transcrustal magma reservoir beneath Soufrière Hills Volcano, Montserrat: Insights from 3-D geodetic inversions. *Geophysical Research Letters*, 47(20):e2020GL089239, 2020.

[81] M. T. Gudmundsson, K. Jónsdóttir, A. Hooper, E. P. Holohan, S. A. Halldórsson, B. G. Ófeigsson, S. Cesca, K. S. Vogfjörd, F. Sigmundsson, T. Högnadóttir, et al. Gradual caldera collapse at Bárdarbunga volcano, Iceland, regulated by lateral magma outflow. *Science*, 353(6296):aaf8988, 2016.

[82] L. Gurioli, L. Colo', A. Bollasina, A. J. Harris, A. Whittington, and M. Ripepe. Dynamics of Strombolian explosions: inferences from field and laboratory studies of erupted bombs from Stromboli volcano. *Journal of Geophysical Research: Solid Earth*, 119(1):319–345, 2014.

[83] A. Harris and M. Ripepe. Synergy of multiple geophysical approaches to unravel explosive eruption conduit and source dynamics–A case study from Stromboli. *Geochemistry*, 67(1):1–35, 2007.

[84] H. Harris, M. Ripepe, S. Calvari, L. Lodato, and L. Spampinato. The 5 April 2003 explosion of Stromboli: timing of eruption dynamics using thermal data. In

THE STROMBOLI VOLCANO: An integrated study of the 2002-2003 Eruption. American Geophysical Union, 2008.

[85] J. Harrison and K. Herbst. Thermoelastic strains and tilts revisited. *Geophysical Research Letters*, 4(11):535–537, 1977.

[86] S. Hautmann, J. Gottsmann, R. S. J. Sparks, A. Costa, O. Melnik, and B. Voight. Modelling ground deformation caused by oscillating overpressure in a dyke conduit at Soufrière Hills Volcano, Montserrat. *Tectonophysics*, 471(1-2):87–95, 2009.

[87] J. Hickey and J. Gottsmann. Benchmarking and developing numerical Finite Element models of volcanic deformation. *Journal of Volcanology and Geothermal Research*, 280:126–130, 2014.

[88] J. Hickey, K. Pascal, M. Head, J. Gottsmann, N. Fournier, S. Hreinsdottir, and R. Syers. Magma pressurization sustains ongoing eruptive episode at dome-building Soufrière Hills volcano, Montserrat. *Geology*, 50(11):1261–1265, 2022.

[89] R. Honda, Y. Yukutake, Y. Morita, S. Sakai, K. Itadera, and K. Kokubo. Precursory tilt changes associated with a phreatic eruption of the Hakone volcano and the corresponding source model. *Earth, Planets and Space*, 70(1):1–14, 2018.

[90] A. Hooper, D. Bekaert, K. Spaans, and M. Arıkan. Recent advances in SAR interferometry time series analysis for measuring crustal deformation. *Tectonophysics*, 514:1–13, 2012.

[91] S. Hreinsdóttir, F. Sigmundsson, M. J. Roberts, H. Björnsson, R. Grapenthin, P. Arason, T. Árnadóttir, J. Hólmjárn, H. Geirsson, R. A. Bennett, et al. Volcanic plume height correlated with magma-pressure change at Grímsvötn Volcano, Iceland. *Nature Geoscience*, 7(3):214–218, 2014.

[92] M. Iguchi, T. Tameguri, Y. Ohta, S. Ueki, and S. Nakao. Characteristics of Volcanic Activity at Sakurajima Volcano's Showa Crater During the Period 2006 to 2011 (¡ Special Section¿ Sakurajima Special Issue). *Bulletin of the Volcanological Society of Japan*, 58(1):115–135, 2013.

[93] M. Iguchi, H. Yakiwara, T. Tameguri, M. Hendrasto, and J.-i. Hirabayashi. Mechanism of explosive eruption revealed by geophysical observations at the Sakurajima,

Suwanosejima and Semeru volcanoes. *Journal of Volcanology and Geothermal Research*, 178(1):1–9, 2008.

[94] S. Inguaggiato, F. Vita, M. Cangemi, and L. Calderone. Changes in CO2 soil degassing style as a possible precursor to volcanic activity: The 2019 case of Stromboli paroxysmal eruptions. *Applied Sciences*, 10(14):4757, 2020.

[95] K. Ishihara. Pressure sources and induced ground deformation associated with explosive eruptions at an andesitic volcano: Sakurajima volcano, Japan. *Magma Transport and Storage*, 1990.

[96] R. M. Iverson, D. Dzurisin, C. A. Gardner, T. M. Gerlach, R. G. LaHusen, M. Lisowski, J. J. Major, S. D. Malone, J. A. Messerich, S. C. Moran, et al. Dynamics of seismogenic volcanic extrusion at Mount St Helens in 2004–05. *Nature*, 444(7118):439–443, 2006.

[97] M. R. James, S. J. Lane, and S. Corder. Modelling the rapid near-surface expansion of gas slugs in low-viscosity magmas. *Geological Society, London, Special Publications*, 307(1):147–167, 2008.

[98] C. Jaupart and S. Vergniolle. Laboratory models of Hawaiian and Strombolian eruptions. *Nature*, 331(6151):58–60, 1988.

[99] C. Jaupart and S. Vergniolle. The generation and collapse of a foam layer at the roof of a basaltic magma chamber. *Journal of Fluid Mechanics*, 203:347–380, 1989.

[100] J. Johnson, R. Sanderson, J. Lyons, R. Escobar-Wolf, G. Waite, and J. Lees. Dissection of a composite volcanic earthquake at Santiaguito, Guatemala. *Geophysical Research Letters*, 36(16), 2009.

[101] K. Kamo and K. Ishihara. A preliminary experiment on automated judgement of the stages of eruptive activity using tiltmeter records at Sakurajima, Japan. In *Volcanic Hazards*, pages 585–598. Springer, 1989.

[102] R. Kawaguchi and T. Nishimura. Numerical investigation of temporal changes in volcanic deformation caused by a gas slug ascent in the conduit. *Journal of Volcanology and Geothermal Research*, 302:1–10, 2015.

[103] G. Kondo, H. Aoyama, T. Nishimura, M. Ripepe, G. Lacanna, R. Genco, R. Kawaguchi, T. Yamada, T. Miwa, and E. Fujita. Gas flux cyclic regime at an open vent magmatic column inferred from seismic and acoustic records. *Scientific Reports*, 9(1):1–8, 2019.

[104] T. Kozono, H. Ueda, T. Ozawa, T. Koyaguchi, E. Fujita, A. Tomiya, and Y. J. Suzuki. Magma discharge variations during the 2011 eruptions of Shinmoe-dake volcano, Japan, revealed by geodetic and satellite observations. *Bulletin of Volcanology*, 75(3):1–13, 2013.

[105] T. Kozono, H. Ueda, T. Shimbori, and K. Fukui. Correlation between magma chamber deflation and eruption cloud height during the 2011 Shinmoe-dake eruptions. *Earth, Planets and Space*, 66(1):1–8, 2014.

[106] M. Laiolo, D. Delle Donne, D. Coppola, M. Bitetto, C. Cigolini, M. Della Schiava, L. Innocenti, G. Lacanna, F. P. La Monica, F. Massimetti, et al. Shallow magma dynamics at open-vent volcanoes tracked by coupled thermal and SO2 observations. *Earth and Planetary Science Letters*, 594:117726, 2022.

[107] P. Landi, R. Corsaro, L. Francalanci, L. Civetta, L. Miraglia, M. Pompilio, and R. Tesoro. Magma dynamics during the 2007 Stromboli eruption (Aeolian Islands, Italy): mineralogical, geochemical and isotopic data. *Journal of Volcanology and Geothermal Research*, 182(3-4):255–268, 2009.

[108] P. Landi, L. Francalanci, M. Pompilio, M. Rosi, R. Corsaro, C. Petrone, I. Nardini, and L. Miraglia. The December 2002–July 2003 effusive event at Stromboli volcano, Italy: insights into the shallow plumbing system by petrochemical studies. *Journal of Volcanology and Geothermal Research*, 155(3-4):263–284, 2006.

[109] N. C. Lautze and B. F. Houghton. Linking variable explosion style and magma textures during 2002 at Stromboli volcano, Italy. *Bulletin of Volcanology*, 69(4):445–460, 2007.

[110] N. C. Lautze and B. F. Houghton. Single explosions at Stromboli in 2002: use of clast microtextures to map physical diversity across a fragmentation zone. *Journal of Volcanology and Geothermal Research*, 170(3-4):262–268, 2008.

[111] D. Legrand and M. Perton. What are VLP signals at Stromboli volcano? *Journal of Volcanology and Geothermal Research*, 421:107438, 2022.

[112] A. T. Linde, S. Sacks, D. Hidayat, B. Voight, A. Clarke, D. Elsworth, G. Mattioli, P. Malin, E. Shalev, S. Sparks, et al. Vulcanian explosion at Soufrière Hills Volcano, Montserrat on March 2004 as revealed by strain data. *Geophysical Research Letters*, 37(19), 2010.

[113] N. Linde, L. Baron, T. Ricci, A. Finizola, A. Revil, F. Muccini, L. Cocchi, and C. Carmisciano. 3-D density structure and geological evolution of Stromboli volcano (Aeolian Islands, Italy) inferred from land-based and sea-surface gravity data. *Journal of Volcanology and Geothermal Research*, 273:58–69, 2014.

[114] J. J. Lyons, G. P. Waite, M. Ichihara, and J. M. Lees. Tilt prior to explosions and the effect of topography on ultra-long-period seismic records at Fuego volcano, Guatemala. *Geophysical Research Letters*, 39(8), 2012.

[115] Y. Maeda, A. Kato, and Y. Yamanaka. Modeling the dynamics of a phreatic eruption based on a tilt observation: Barrier breakage leading to the 2014 eruption of Mount Ontake, Japan. *Journal of Geophysical Research: Solid Earth*, 122(2):1007–1024, 2017.

[116] F. Manta and B. Taisne. A Bayesian approach to infer volcanic system parameters, timing, and size of Strombolian events from a single tilt station. *Journal of Geophysical Research: Solid Earth*, 124(5):5081–5100, 2019.

[117] E. Marchetti, R. Genco, and M. Ripepe. Ground deformation and seismicity related to the propagation and drainage of the dyke feeding system during the 2007 effusive eruption at Stromboli volcano (Italy). *Journal of Volcanology and Geothermal Research*, 182(3-4):155–161, 2009.

[118] E. Marchetti and M. Ripepe. Stability of the seismic source during effusive and explosive activity at Stromboli Volcano. *Geophysical Research Letters*, 32(3), 2005.

[119] L. H. Marsden, J. W. Neuberg, and M. E. Thomas. Topography and tilt at volcanoes. *Frontiers in Earth Science*, 7:317, 2019.

[120] L. H. Marsden, J. W. Neuberg, M. E. Thomas, P. A. Mothes, and M. C. Ruiz. Combining magma flow and deformation modeling to explain observed changes in tilt. *Frontiers in Earth Science*, 7:219, 2019.

[121] M. Martini, F. Giudicepietro, L. D ' Auria, A. M. Esposito, T. Caputo, R. Curciotti, W. De Cesare, M. Orazi, G. Scarpato, A. Caputo, et al. Seismological monitoring of the February 2007 effusive eruption of the Stromboli volcano. *Annals of Geophysics*, 2007.

[122] L. G. Mastin, M. Lisowski, E. Roeloffs, and N. Beeler. Improved constraints on the estimated size and volatile content of the Mount St. Helens magma system from the 2004–2008 history of dome growth and deformation. *Geophysical Research Letters*, 36(20), 2009.

[123] M. Mattia, B. Di Lieto, G. Ganci, V. Bruno, P. Romano, F. Ciancitto, P. De Martino, S. Gambino, M. Aloisi, M. Sciotto, et al. The 2019 Eruptive Activity at Stromboli Volcano: A Multidisciplinary Approach to Reveal Hidden Features of the " Unexpected " 3 July Paroxysm. *Remote Sensing*, 13(20):4064, 2021.

[124] M. Mattia, M. Rossi, F. Guglielmino, M. Aloisi, and Y. Bock. The shallow plumbing system of Stromboli Island as imaged from 1 Hz instantaneous GPS positions. *Geophysical Research Letters*, 31(24), 2004.

[125] K. F. McKee, D. C. Roman, G. P. Waite, and D. Fee. Silent Very Long Period Seismic Events (VLPs) at Stromboli Volcano, Italy. *Geophysical Research Letters*, page e2022GL100735, 2022.

[126] D. McTigue. Elastic stress and deformation near a finite spherical magma body: resolution of the point source paradox. *Journal of Geophysical Research: Solid Earth*, 92(B12):12931–12940, 1987.

[127] N. Métrich, A. Bertagnini, and A. Di Muro. Conditions of magma storage, degassing and ascent at Stromboli: new insights into the volcano plumbing system with inferences on the eruptive dynamics. *Journal of Petrology*, 51(3):603–626, 2010.

[128] N. Métrich, A. Bertagnini, P. Landi, and M. Rosi. Crystallization driven by decompression and water loss at Stromboli volcano (Aeolian Islands, Italy). *Journal of Petrology*, 42(8):1471–1490, 2001.

[129] N. Métrich, A. Bertagnini, and M. Pistolesi. Paroxysms at Stromboli volcano (Italy): source, genesis and dynamics. *Frontiers in Earth Science*, 9:593339, 2021.

[130] L. Michon, T. Staudacher, V. Ferrazzini, P. Bachèlery, and J. Marti. April 2007 collapse of Piton de la Fournaise: A new example of caldera formation. *Geophysical Research Letters*, 34(21), 2007.

[131] A. Miklius and P. Cervelli. Interaction between Kilauea and Mauna Loa. *Nature*, 421(6920):229–229, 2003.

[132] K. Mogi. Relations between the eruptions of various volcanoes and the deformations of the ground surfaces around them. *Earthq Res Inst*, 36:99–134, 1958.

[133] H. Nakamichi and H. Aoyama. Eruption Process Inferred from Multi-parameter Geophysical Observations. *Bulletin of the Volcanological Society of Japan*, 61(1):119–154, 2016.

[134] C. A. Neal, S. Brantley, L. Antolik, J. Babb, M. Burgess, K. Calles, M. Cappos, J. Chang, S. Conway, L. Desmither, et al. The 2018 rift eruption and summit collapse of Kīlauea Volcano. *Science*, 363(6425):367–374, 2019.

[135] M. Neri and G. Lanzafame. Structural features of the 2007 Stromboli eruption. *Journal of Volcanology and Geothermal Research*, 182(3-4):137–144, 2009.

[136] J. Neuberg, R. Luckett, M. Ripepe, and T. Braun. Highlights from a seismic broadband array on Stromboli volcano. *Geophysical Research Letters*, 21(9):749–752, 1994.

[137] T. Nishimura. Ground deformation caused by magma ascent in an open conduit. *Journal of Volcanology and Geothermal Research*, 187(3-4):178–192, 2009.

[138] T. Nishimura, M. Ichihara, and S. Ueki. Investigation of the Onikobe geyser, NE Japan, by observing the ground tilt and flow parameters. *Earth, Planets and Space*, 58(6):e21–e24, 2006.

[139] T. Nishimura, M. Iguchi, R. Kawaguchi, M. Hendrasto, U. Rosadi, et al. Inflations prior to Vulcanian eruptions and gas bursts detected by tilt observations at Semeru Volcano, Indonesia. *Bulletin of Volcanology*, 74(4):903–911, 2012.

[140] T. Nishimura, M. Iguchi, H. Yakiwara, J. Oikawa, R. Kawaguchi, H. Aoyama, H. Nakamichi, Y. Ohta, and T. Tameguri. Mechanism of small vulcanian eruptions

at Suwanosejima volcano, Japan, as inferred from precursor inflations and tremor signals. *Bulletin of Volcanology*, 75(12):1–12, 2013.

[141] Y. Okada. Surface deformation due to shear and tensile faults in a half-space. *Bulletin of the Seismological Society of America*, 75(4):1135–1154, 1985.

[142] Y. Okada. Internal deformation due to shear and tensile faults in a half-space. *Bulletin of the Seismological Society of America*, 82(2):1018–1040, 1992.

[143] Y. Okada and E. Yamamoto. Dyke intrusion model for the 1989 seismovolcanic activity off Ito, central Japan. *Journal of Geophysical Research: Solid Earth*, 96(B6):10361–10376, 1991.

[144] J. Oppenheimer, A. Capponi, K. Cashman, S. Lane, A. Rust, and M. James. Analogue experiments on the rise of large bubbles through a solids-rich suspension: a "weak plug" model for Strombolian eruptions. *Earth and Planetary Science Letters*, 531:115931, 2020.

[145] E. Parfitt and L. Wilson. Explosive volcanic eruptions—IX. The transition between Hawaiian-style lava fountaining and Strombolian explosive activity. *Geophysical Journal International*, 121(1):226–232, 1995.

[146] E. A. Parfitt. A discussion of the mechanisms of explosive basaltic eruptions. *Journal of Volcanology and Geothermal Research*, 134(1-2):77–107, 2004.

[147] D. Patanè, G. Barberi, P. De Gori, O. Cocina, L. Zuccarello, A. Garcia-Yeguas, M. Castellano, A. D'Alessandro, and T. Sgroi. The shallow magma chamber of Stromboli Volcano (Italy). *Geophysical Research Letters*, 44(13):6589–6596, 2017.

[148] M. R. Patrick. Dynamics of Strombolian ash plumes from thermal video: Motion, morphology, and air entrainment. *Journal of Geophysical Research: Solid Earth*, 112(B6), 2007.

[149] M. R. Patrick, T. Orr, D. Swanson, and E. Lev. Shallow and deep controls on lava lake surface motion at Kīlauea Volcano. *Journal of Volcanology and Geothermal Research*, 328:247–261, 2016.

[150] C. M. Petrone, S. Mollo, R. Gertisser, Y. Buret, P. Scarlato, E. Del Bello, D. Andronico, B. Ellis, A. Pontesilli, G. De Astis, et al. Magma recharge and mush reju-

venation drive paroxysmal activity at Stromboli volcano. *Nature Communications*, 13(1):1–17, 2022.

[151] M. Pichavant, I. Di Carlo, M. Pompilio, and N. Le Gall. Timescales and mechanisms of paroxysm initiation at Stromboli volcano, Aeolian Islands, Italy. *Bulletin of Volcanology*, 84(4):1–26, 2022.

[152] V. Pinel, M. P. Poland, and A. Hooper. Volcanology: Lessons learned from synthetic aperture radar imagery. *Journal of Volcanology and Geothermal Research*, 289:81–113, 2014.

[153] N. A. Pino, R. Moretti, P. Allard, and E. Boschi. Seismic precursors of a basaltic paroxysmal explosion track deep gas accumulation and slug upraise. *Journal of Geophysical Research: Solid Earth*, 116(B2), 2011.

[154] L. Pioli, M. Pistolesi, and M. Rosi. Transient explosions at open-vent volcanoes: The case of Stromboli (Italy). *Geology*, 42(10):863–866, 2014.

[155] L. Pioli, M. Rosi, S. Calvari, L. Spampinato, A. Renzulli, and A. Di Roberto. The eruptive activity of 28 and 29 December 2002. *The Stromboli volcano: an integrated study of the 2002-2003 eruption*, pages 105–115, 2008.

[156] M. Pistolesi, D. Delle Donne, L. Pioli, M. Rosi, and M. Ripepe. The 15 March 2007 explosive crisis at Stromboli volcano, Italy: assessing physical parameters through a multidisciplinary approach. *Journal of Geophysical Research: Solid Earth*, 116(B12), 2011.

[157] S. Plank, F. Marchese, C. Filizzola, N. Pergola, M. Neri, M. Nolde, and S. Martinis. The July/August 2019 Lava Flows at the Sciara del Fuoco, Stromboli–Analysis from Multi-Sensor Infrared Satellite Imagery. *Remote Sensing*, 11(23):2879, 2019.

[158] M. Ripepe, S. Ciliberto, and M. Della Schiava. Time constraints for modeling source dynamics of volcanic explosions at Stromboli. *Journal of Geophysical Research: Solid Earth*, 106(B5):8713–8727, 2001.

[159] M. Ripepe, D. Delle Donne, G. Lacanna, E. Marchetti, and G. Ulivieri. The onset of the 2007 Stromboli effusive eruption recorded by an integrated geophysical network. *Journal of Volcanology and Geothermal Research*, 182(3-4):131–136, 2009.

[160] M. Ripepe, D. Delle Donne, D. Legrand, S. Valade, and G. Lacanna. Magma pressure discharge induces very long period seismicity. *Scientific Reports*, 11(1):1–12, 2021.

[161] M. Ripepe, D. D. Donne, R. Genco, G. Maggio, M. Pistolesi, E. Marchetti, G. Lacanna, G. Ulivieri, and P. Poggi. Volcano seismicity and ground deformation unveil the gravity-driven magma discharge dynamics of a volcanic eruption. *Nature Communications*, 6(1):1–6, 2015.

[162] M. Ripepe, D. D. Donne, A. Harris, E. Marchetti, and G. Ulivieri. Dynamics of Strombolian activity. *Washington DC American Geophysical Union Geophysical Monograph Series*, 182:39–48, 2008.

[163] M. Ripepe, G. Lacanna, M. Pistolesi, M. C. Silengo, A. Aiuppa, M. Laiolo, F. Massimetti, L. Innocenti, M. Della Schiava, M. Bitetto, et al. Ground deformation reveals the scale-invariant conduit dynamics driving explosive basaltic eruptions. *Nature Communications*, 12(1):1–8, 2021.

[164] M. Ripepe, E. Marchetti, P. Poggi, A. Harris, A. Fiaschi, and G. Ulivieri. Seismic, acoustic, and thermal network monitors the 2003 eruption of Stromboli Volcano. *Eos, Transactions American Geophysical Union*, 85(35):329–332, 2004.

[165] M. Ripepe, M. Pistolesi, D. Coppola, D. Delle Donne, R. Genco, G. Lacanna, M. Laiolo, E. Marchetti, G. Ulivieri, and S. Valade. Forecasting effusive dynamics and decompression rates by magmastatic model at open-vent volcanoes. *Scientific Reports*, 7(1):1–9, 2017.

[166] M. Ripepe, P. Poggi, T. Braun, and E. Gordeev. Infrasonic waves and volcanic tremor at Stromboli. *Geophysical Research Letters*, 23(2):181–184, 1996.

[167] M. Ripepe, M. Rossi, and G. Saccorotti. Image processing of explosive activity at Stromboli. *Journal of Volcanology and Geothermal Research*, 54(3-4):335–351, 1993.

[168] A. Rittmann. Der ausbruch des Stromboli am 11 September 1930. *Z. vulkanol*, 14:47–77, 1931.

[169] O. Roche, T. Druitt, and O. Merle. Experimental study of caldera formation. *Journal of Geophysical Research: Solid Earth*, 105(B1):395–416, 2000.

[170] P. Rodgers. The response of the horizontal pendulum seismometer to Rayleigh and Love waves, tilt, and free oscillations of the Earth. *Bulletin of the Seismological Society of America*, 58(5):1385–1406, 1968.

[171] A. Roman and P. Lundgren. Dynamics of large effusive eruptions driven by caldera collapse. *Nature*, 592(7854):392–396, 2021.

[172] E. Ronchin, A. Geyer, and J. Martí. Evaluating topographic effects on ground deformation: insights from finite element modeling. *Surveys in Geophysics*, 36(4):513–548, 2015.

[173] M. Rosi, A. Bertagnini, and P. Landi. Onset of the persistent activity at Stromboli volcano (Italy). *Bulletin of volcanology*, 62(4):294–300, 2000.

[174] M. Rosi, M. Pistolesi, A. Bertagnini, P. Landi, M. Pompilio, and A. Di Roberto. Stromboli volcano, Aeolian Islands (Italy): present eruptive activity and hazards. *Geological Society, London, Memoirs*, 37(1):473–490, 2013.

[175] R. W. Sanderson, J. Johnson, and J. Lees. Ultra-long period seismic signals and cyclic deflation coincident with eruptions at Santiaguito volcano, Guatemala. *Journal of Volcanology and Geothermal Research*, 198(1-2):35–44, 2010.

[176] P. Segall. Earthquake and volcano deformation. In *Earthquake and Volcano Deformation*. Princeton University Press, 2010.

[177] P. Segall. Volcano deformation and eruption forecasting. *Geological Society, London, Special Publications*, 380(1):85–106, 2013.

[178] P. Segall. Repressurization following eruption from a magma chamber with a viscoelastic aureole. *Journal of Geophysical Research: Solid Earth*, 121(12):8501–8522, 2016.

[179] D. R. Sherrod, W. E. Scott, and P. H. Stauffer. A volcano rekindled: the renewed eruption of Mount St. Helens, 2004-2006. Technical report, US Geological Survey, 2008.

[180] L. Spampinato, S. Calvari, H. Harris, and J. Dehn. Evolution of the lava flow field by daily thermal and visible airborne surveys. In *THE STROMBOLI VOLCANO: An integrated study of the 2002-2003 Eruption*. American Geophysical Union, 2008.

[181] R. Sparks and S. Young. The eruption of Soufrière Hills Volcano, Montserrat (1995-1999): overview of scientific results. *Geological Society, London, Memoirs*, 21(1):45–69, 2002.

[182] D. S. Stevenson and S. Blake. Modelling the dynamics and thermodynamics of volcanic degassing. *Bulletin of Volcanology*, 60(4):307–317, 1998.

[183] S. C. Stissi, R. Napoli, G. Currenti, A. Afanasyev, and G. Montegrossi. Influence of permeability on the hydrothermal system at Vulcano Island (Italy): inferences from numerical simulations. *Earth, Planets and Space*, 73(1):1–21, 2021.

[184] J. Suckale, T. Keller, K. V. Cashman, and P.-O. Persson. Flow-to-fracture transition in a volcanic mush plug may govern normal eruptions at Stromboli. *Geophysical Research Letters*, 43(23):12–071, 2016.

[185] S. Sugimura, T. Nishimura, G. Lacanna, D. Legrand, S. Valade, and M. Ripepe. Seismic Source Migration During Strombolian Eruptions Inferred by Very-Near-Field Broadband Seismic Network. *Journal of Geophysical Research: Solid Earth*, 126(12):e2021JB022623, 2021.

[186] N. Sugiura. Further analysis of the data by Akaike's information criterion and the finite corrections: Further analysis of the data by akaike's. *Communications in Statistics-theory and Methods*, 7(1):13–26, 1978.

[187] J. Taddeucci, M. Edmonds, B. Houghton, M. R. James, and S. Vergniolle. Hawaiian and Strombolian eruptions. In *The Encyclopedia of Volcanoes*, pages 485–503. Elsevier, 2015.

[188] J. Taddeucci, D. Palladino, G. Sottili, D. Bernini, D. Andronico, and A. Cristaldi. Linked frequency and intensity of persistent volcanic activity at Stromboli (Italy). *Geophysical Research Letters*, 40(13):3384–3388, 2013.

[189] R. Takahashi, Y. Maeda, and T. Watanabe. Waveform inversion of the ultra-long-period seismic event associated with ground tilt motion during an eruption of Mount Kusatsu–Shirane, Japan, on January 23, 2018. *Earth, Planets and Space*, 74(1):1–21, 2022.

[190] M. Takeo, Y. Maehara, M. Ichihara, T. Ohminato, R. Kamata, and J. Oikawa. Ground deformation cycles in a magma-effusive stage, and sub-Plinian and Vulca-

nian eruptions at Kirishima volcanoes, Japan. *Journal of Geophysical Research: Solid Earth*, 118(9):4758–4773, 2013.

[191] D. Tarchi, N. Casagli, J. Fortuny-Guasch, L. Guerri, G. Antonello, and D. Leva. Ground deformation from ground-based SAR interferometry. *The Stromboli Volcano, an integrated study of the 2002–2003 eruption. AGU Geophys Monogr*, 182:359–372, 2008.

[192] Y. Tateo and M. Iguchi. Ground deformation associated with BL-type earthquake swarms at Sakurajima volcano. *Bull. Volcanol. Soc. Japan*, 54(4):175–186, 2009.

[193] A. Terada, W. Kanda, Y. Ogawa, T. Yamada, M. Yamamoto, T. Ohkura, H. Aoyama, T. Tsutsui, and S. Onizawa. The 2018 phreatic eruption at Mt. Motoshirane of Kusatsu–Shirane volcano, Japan: eruption and intrusion of hydrothermal fluid observed by a borehole tiltmeter network. *Earth, Planets and Space*, 73(1):1–17, 2021.

[194] A. Tibaldi. Multiple sector collapses at Stromboli volcano, Italy: how they work. *Bulletin of Volcanology*, 63(2):112–125, 2001.

[195] S. Tinti, G. Pagnoni, F. Zaniboni, and E. Bortolucci. Tsunami generation in Stromboli island and impact on the south-east Tyrrhenian coasts. *Natural Hazards and Earth System Sciences*, 3(5):299–309, 2003.

[196] S. Tinti, F. Zaniboni, G. Pagnoni, and A. Manucci. Stromboli Island (Italy): scenarios of tsunamis generated by submarine landslides. *Pure and Applied Geophysics*, 165(11):2143–2167, 2008.

[197] P. Tommasi, P. Baldi, F. L. Chiocci, M. Coltelli, M. Marsella, and C. Romagnoli. Slope failures induced by the December 2002 eruption at Stromboli volcano. *Washington DC American Geophysical Union Geophysical Monograph Series*, 182:129–145, 2008.

[198] S. Valade, G. Lacanna, D. Coppola, M. Laiolo, M. Pistolesi, D. Delle Donne, R. Genco, E. Marchetti, G. Ulivieri, C. Allocca, et al. Tracking dynamics of magma migration in open-conduit systems. *Bulletin of Volcanology*, 78(11):78, 2016.

[199] J. Vandemeulebrouck, R. A. Sohn, M. L. Rudolph, S. Hurwitz, M. Manga, M. J. Johnston, S. A. Soule, D. McPhee, J. M. Glen, L. Karlstrom, et al. Eruptions at

Lone Star geyser, Yellowstone National Park, USA: 2. Constraints on subsurface dynamics. *Journal of Geophysical Research: Solid Earth*, 119(12):8688–8707, 2014.

[200] S. Vergniolle and G. Brandeis. Strombolian explosions: 1. A large bubble breaking at the surface of a lava column as a source of sound. *Journal of Geophysical Research: Solid Earth*, 101(B9):20433–20447, 1996.

[201] S. Vergniolle, G. Brandeis, and J.-C. Mareschal. Strombolian explosions: 2. Eruption dynamics determined from acoustic measurements. *Journal of Geophysical Research: Solid Earth*, 101(B9):20449–20466, 1996.

[202] M. Viccaro, A. Cannata, F. Cannavò, R. De Rosa, M. Giuffrida, E. Nicotra, M. Petrelli, and G. Sacco. Shallow conduit dynamics fuel the unexpected paroxysms of Stromboli volcano during the summer 2019. *Scientific Reports*, 11(1):1–15, 2021.

[203] B. Voight, A. Linde, I. Sacks, G. Mattioli, R. Sparks, D. Elsworth, D. Hidayat, P. Malin, E. Shalev, C. Widiwijayanti, et al. Unprecedented pressure increase in deep magma reservoir triggered by lava-dome collapse. *Geophysical Research Letters*, 33(3), 2006.

[204] G. Wadge, B. Voight, R. Sparks, P. Cole, S. Loughlin, and R. Robertson. An overview of the eruption of Soufriere Hills Volcano, Montserrat from 2000 to 2010. *Geological Society, London, Memoirs*, 39(1):1–40, 2014.

[205] J. Walsh and R. Decker. Surface deformation associated with volcanism. *Journal of Geophysical Research*, 76(14):3291–3302, 1971.

[206] E. Wielandt, T. Forbriger, et al. Near-field seismic displacement and tilt associated with the explosive activity of Stromboli. *Annals of Geophysics*, 42:407–416, 1999.

[207] C. A. Williams and G. Wadge. The effects of topography on magma chamber deformation models: Application to Mt. Etna and radar interferometry. *Geophysical Research Letters*, 25(10):1549–1552, 1998.

[208] C. A. Williams and G. Wadge. An accurate and efficient method for including the effects of topography in three-dimensional elastic models of ground deformation with applications to radar interferometry. *Journal of Geophysical Research: Solid Earth*, 105(B4):8103–8120, 2000.

[209] N. Yamakawa. On the strain produced in a semi-infinite elastic solid by an interior source of stress. *J. Seismol. Soc. Japan, Ser. 2*, 8(2):84–98, 1955.

[210] X.-M. Yang, P. M. Davis, and J. H. Dieterich. Deformation from inflation of a dipping finite prolate spheroid in an elastic half-space as a model for volcanic stressing. *Journal of Geophysical Research: Solid Earth*, 93(B5):4249–4257, 1988.